

INFORMATION TO USERS

This manuscript has been reproduced from the microfilm master. UMI films the text directly from the original or copy submitted. Thus, some thesis and dissertation copies are in typewriter face, while others may be from any type of computer printer.

The quality of this reproduction is dependent upon the quality of the copy submitted. Broken or indistinct print, colored or poor quality illustrations and photographs, print bleedthrough, substandard margins, and improper alignment can adversely affect reproduction.

In the unlikely event that the author did not send UMI a complete manuscript and there are missing pages, these will be noted. Also, if unauthorized copyright material had to be removed, a note will indicate the deletion.

Oversize materials (e.g., maps, drawings, charts) are reproduced by sectioning the original, beginning at the upper left-hand corner and continuing from left to right in equal sections with small overlaps. Each original is also photographed in one exposure and is included in reduced form at the back of the book.

Photographs included in the original manuscript have been reproduced xerographically in this copy. Higher quality 6" x 9" black and white photographic prints are available for any photographs or illustrations appearing in this copy for an additional charge. Contact UMI directly to order.

UMI

A Bell & Howell Information Company
300 North Zeeb Road, Ann Arbor MI 48106-1346 USA
313/761-4700 800/521-0600

University of Alberta

**NON-INTRUSIVE KNOCK DETECTION
IN A TURBOCHARGED, DUAL FUEL ENGINE**

BY

STEFAN ROSS ROBERTS



A thesis submitted to the Faculty of Graduate Studies and Research in partial fulfillment
of the requirements for the degree of Master of Science

Department of Mechanical Engineering

Edmonton, Alberta
Fall 1997



National Library
of Canada

Acquisitions and
Bibliographic Services

395 Wellington Street
Ottawa ON K1A 0N4
Canada

Bibliothèque nationale
du Canada

Acquisitions et
services bibliographiques

395, rue Wellington
Ottawa ON K1A 0N4
Canada

Your file *Votre référence*

Our file *Notre référence*

The author has granted a non-exclusive licence allowing the National Library of Canada to reproduce, loan, distribute or sell copies of this thesis in microform, paper or electronic formats.

The author retains ownership of the copyright in this thesis. Neither the thesis nor substantial extracts from it may be printed or otherwise reproduced without the author's permission.

L'auteur a accordé une licence non exclusive permettant à la Bibliothèque nationale du Canada de reproduire, prêter, distribuer ou vendre des copies de cette thèse sous la forme de microfiche/film, de reproduction sur papier ou sur format électronique.

L'auteur conserve la propriété du droit d'auteur qui protège cette thèse. Ni la thèse ni des extraits substantiels de celle-ci ne doivent être imprimés ou autrement reproduits sans son autorisation.

0-612-22664-6

**University of Alberta
Library Release Form**

Name of Author: Stefan Ross Roberts

Title of Thesis: Non-Intrusive Knock Detection in a Turbocharged, Dual Fuel Engine

Degree: Master of Science

Year this Degree Granted: 1997

Permission is hereby granted to the University of Alberta Library to reproduce single copies of this thesis and to lend or sell such copies for private, scholarly, or scientific research purposes only.

The author reserves all other publication and other rights in association with the copyright in the thesis, and except as hereinbefore provided, neither the thesis nor any substantial portion thereof may be printed or otherwise reproduced in any material form whatever without the author's prior written permission.



Box 28

Domain, Manitoba

R0G 0M0

Date: 10 July 1997

“From the point of conception
To the moment of Truth
At the point of surrender
To the burden of proof

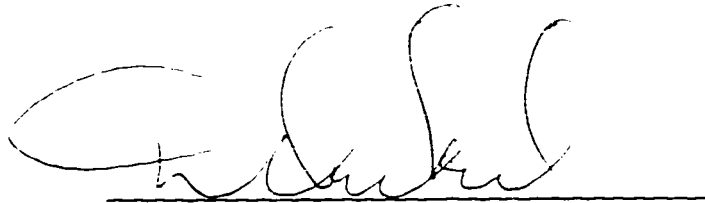
From the point of ignition
To the final drive
The point of the journey is not to arrive -
anything can happen.”

- Neil Peart, *Prime Mover*, 1987.

University of Alberta

Faculty of Graduate Studies and Research

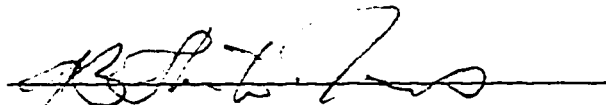
The undersigned certify that they have read, and recommend to the Faculty of Graduate Studies and Research for acceptance, a thesis entitled Non-Intrusive Knock Detection in a Turbocharged, Dual Fuel Engine by Stefan Ross Roberts in partial fulfillment of the requirements for the degree of Master of Science.



Dr. M. D. Checkel



Dr. J.D. Dale



Dr. A.B. Thornton-Trump
Department of Mech. and Indus. Engineering
The University of Manitoba

Date: 9-17-10

ABSTRACT

Recently, “dual fuel” vehicle engines have been developed which retain the high thermal efficiency and desirable torque characteristics of diesel-fuelled engines while replacing most of the required diesel with cleaner-burning natural gas. One of the biggest problems facing dual fuel engine technology is the tendency for end-gas regions to violently autoignite, or knock, at full torque. In mass-production spark-ignition engines, knock is detected non-intrusively by analyzing vibrations transmitted throughout the engine structure. Since dual fuel conversions are based on diesel powerplants, the added stiffness and strength of their compression-ignition blocks tends to make vibration analysis more problematic. In this investigation, a test engine was outfitted with a block-mounted wide-band accelerometer, and a pressure transducer was installed inside one of the combustion chambers. The output of the pressure transducer during knock testing was correlated to operator-observed knock intensity to determine the most accurate pressure-based measure of knock. Accelerometer output was then compared to the pressure transducer’s indication of knock severity to determine the best block vibration statistic. The maximum value of bandpass filtered acceleration amplitude was found to be the optimum vibrational statistic when analyzed within a data window extending 40 crankshaft degrees beyond the initiation of knock. This research concludes that there is an excellent possibility that conventional non-intrusive knock detection systems will also be useful for dual fuel engine knock control.

ACKNOWLEDGEMENTS

I would like to acknowledge the contributions of the following people, who made it possible for me to document the past three years of my life in the following pages:

Dr. M.D. Checkel - my thesis advisor, who kept me on the path to success...

Dr. J.D. Dalc, Mr. M.Y. Ackerman, Dr. L.W. Kostiuk, and Dr. D.J. Wilson - the balance of the Combustion and Environment Group, who provided valuable insights into what I have accomplished...

Mr. Allan Muir, Mr. Donald Fuhr, Mr. Tony van Straten, Mr. Albert Yuen, and Mr. Max Schubert - for their assistance in constructing and modifying the laboratory apparatus, and all their complimentary doughnuts...

Mr. Paul Newman, Mr. Jamie Newsom, and Mr. Kevin Visser of Alternative Fuel Systems Inc. - for their financial support and technical wizardry...

The Natural Sciences and Engineering Research Council (NSERC) and the Department of Mechanical Engineering - for their financial support of the dual fuel program...

Mr. Wayne Pittman - for his digital prehensilism with all things electrical...

John Take. Chris Hutton, Oleg Zastavniouk, and my associates in the Combustion Lab - for making sure I finished my thesis (but not too soon)...

and Reg Dunlop. David Gilmour, Robert Godin, Neil Peart, Bobby Rahal, Bernd Pieper, Pete Townshend, Gary Turner, Nichole Annis, Neil Young, Alan Hale and Tom Bopp, the Pembina Pucks, the Mec-spos, Ian Trump, T², and my family - for their various forms of inspiration.

TABLE OF CONTENTS

	PAGE
1.0 Chapter 1 Introduction.....	1
1.1 Preamble.....	1
1.2 Environmental and Economic Concerns of Current Diesel Engines.....	1
1.3 Alternative Fuels for Compression-Ignition Engines.....	3
1.4 Dual Fuel Technology	6
1.5 Conversion of a Mercedes OM366LA Engine	8
1.6 Knock Detection and Control.....	10
1.7 Study Objectives and Approach	14
2.0 Chapter 2 Survey of Dual Fuel Engine Knock Research	15
2.1 History of Fundamental Knock Research.....	15
2.2 Non-Intrusive Knock Detection in Production-Volume Engines.....	22
3.0 Chapter 3 Experimental Apparatus	25
3.1 The Test Engine.....	25
3.2 Test Cell Control Equipment.....	28
3.3 Knock Detection and Analysis Equipment.....	31
4.0 Chapter 4 Experimental Methodology	37
4.1 Production and Recording of Knock Signals	37
4.2 Definition of Operator-Observed Standard Knock Intensity (SKI) Scale	39
4.3 In-Cylinder Analysis Techniques	40
4.3.1 <i>Initial Pressure Trace Observations</i>	40
4.3.2 <i>Bandpass Filtering</i>	42

TABLE OF CONTENTS (CONTINUED)

	PAGE
4.3.3 <i>High-Frequency Pressure Statistics</i>	44
4.3.4 <i>Pressure Data Windows</i>	46
4.4 Non-Intrusive Analysis Techniques	49
4.4.1 <i>Accelerometer Statistics</i>	49
4.4.2 <i>Accelerometer Data Windows</i>	52
5.0 Chapter 5 Results and Analysis	54
5.1 Introduction	54
5.2 Operator-Observed Knock Intensity	55
5.3 Gross Pressure Results	57
5.4 Determination of Characteristic Knock Intensity	59
5.5 Investigation of In-Cylinder Pressure Statistics	62
5.6 Investigation of Non-Intrusive Statistics	71
5.6.1 <i>Accelerometer Data Window Start Point</i>	71
5.6.2 <i>Accelerometer Data Window Length and Best Statistic, Overfuelling Experiment</i>	74
5.6.3 <i>Accelerometer Data Window Length and Best Statistic, Pilot Experiment</i>	78
5.7 Summary of Results	85
6.0 Chapter 6 Conclusions and Considerations for Future Development	91
6.1 Summary	91
6.2 Conclusions	94
6.3 Future Work	95

TABLE OF CONTENTS (CONTINUED)

	PAGE
References	97
Appendix A Pressure Transducer Calibration	102
Appendix B Standard Knock Intensity Data.....	106
Appendix C Estimating the Fundamental Knock Frequency	108
Appendix D Pressure Investigation Data	111
Appendix E Accelerometer Window Start Position Data	114
Appendix F Accelerometer Window Length Data.....	117

LIST OF TABLES

		PAGE
Table 1.1	Storage Properties of Selected Transportation Fuels.....	4
Table 4.1	Standard Knock Index (SKI)	40
Table 5.1	Gross Pressure Statistics, Gaseous Overfuelling and Diesel Baseline	58
Table 5.2	Pressure Trace Frequency Investigation (severe knock), 1500 rpm	60
Table 5.3	Pressure Trace Frequency Investigation (severe knock), 2100 rpm	60
Table 5.4	Summary of Pressure Statistic Correlations to SKI, 1500 rpm	67
Table 5.5	Summary of Pressure Statistic Correlations to SKI, 2100 rpm	67
Table 5.6	Effect of Window Start Point on Accelerometer Correlations, 1500 rpm... 72	
Table 5.7	Effect of Window Start Point on Accelerometer Correlations, 2100 rpm... 73	
Table 5.8	Correlation of Accelerometer Statistics to FPmax, Overfuelling Experiment	78
Table 5.9	Correlation of Accelerometer Statistics to FPmax, Pilot Experiment	83
Table A.1	Kistler 601B1 Pressure Transducer Calibration Data.....	102
Table B.1	Observed SKI Levels, Gaseous Overfuelling	106
Table B.2	Observed SKI Levels, Pilot Reduction	107
Table D.1	Correlation of Maximum Filtered Pressure to SKI	111
Table D.2	Correlation of Maximum Filtered Pressure to SKI, 2100 rpm	111
Table D.3	Correlation of RMS Filtered Pressure to SKI, 1500 rpm	112
Table D.4	Correlation of RMS Filtered Pressure to SKI, 2100 rpm	112
Table D.5	Correlation of Filtered Pressure FT Amplitude to SKI, 1500 rpm	112
Table D.6	Correlation of Filtered Pressure FT Amplitude to SKI, 2100 rpm	113
Table D.7	Correlation of Pressure Statistics to SKI for 40-degree Window, Pilot Reduction, 1500 rpm.....	113
Table D.8	Correlation of Pressure Statistics to SKI for 40-degree Window, Pilot Reduction, 2100 rpm.....	113
Table E.1	Correlation of FAm _{ax} to FPmax At Various Start Positions, 1500 rpm... 114	
Table E.2	Correlation of FAm _{ax} to FPmax At Various Start Positions, 2100 rpm... 114	

LIST OF TABLES (CONTINUED)

	PAGE
Table E.3 Correlation of FArms to FPmax At Various Start Positions, 1500 rpm....	115
Table E.4 Correlation of FArms to FPmax At Various Start Positions, 2100 rpm....	115
Table E.5 Correlation of FAamp to FPmax At Various Start Positions, 1500 rpm...	115
Table E.6 Correlation of FAamp to FPmax At Various Start Positions, 2100 rpm...	116
Table F.1 Correlation of FAmx to FPmax, Gaseous Overfuelling, 1500 rpm.....	117
Table F.2 Correlation of FAmx to FPmax, Gaseous Overfuelling, 2100 rpm.....	117
Table F.3 Correlation of FArms to FPmax, Gaseous Overfuelling, 1500 rpm.....	118
Table F.4 Correlation of FArms to FPmax, Gaseous Overfuelling, 2100 rpm.....	118
Table F.5 Correlation of FAamp to FPmax, Gaseous Overfuelling, 1500 rpm.....	118
Table F.6 Correlation of FAamp to FPmax, Gaseous Overfuelling, 2100 rpm.....	119
Table F.7 Correlation of FAmx to FPmax, Pilot Reduction, 1500 rpm.....	119
Table F.8 Correlation of FAmx to FPmax, Pilot Reduction, 2100 rpm.....	119
Table F.9 Correlation of FArms to FPmax, Pilot Reduction, 1500 rpm.....	120
Table F.10 Correlation of FArms to FPmax, Pilot Reduction, 2100 rpm.....	120
Table F.11 Correlation of FAamp to FPmax, Pilot Reduction, 1500 rpm.....	120
Table F.12 Correlation of FAamp to FPmax, Pilot Reduction, 2100 rpm.....	121

LIST OF FIGURES

	PAGE
Figure 2.1 Primary Transverse Knocking Modes for a “Hockey Puck” Combustion Chamber	17
Figure 2.2 Fundamental Nodal Lines for Diesel Combustion Chamber	18
Figure 3.1 Schematic of AFS Dual Fuel System	26
Figure 3.2 AFS Crankshaft Position Mask with Corresponding Output Wave	28
Figure 3.3 Pressure Transducer Location in Combustion Chamber Six	32
Figure 3.4 Transducer Sleeve Assembly	33
Figure 3.5 Schematic of Recording and Digitizing Equipment	36
Figure 4.1 Comparison of Pressure Traces at 2100 rpm	42
Figure 4.2 Comparison of Filtered Pressure Traces at 2100 rpm	43
Figure 4.3 Comparison of Fourier-transformed Pressure Traces at 2100 rpm	46
Figure 4.4 Various Pressure Data Windows for Knock at 2100 rpm	47
Figure 4.5 Comparison of Accelerometer Signals at 2100 rpm	50
Figure 4.6 Comparison of Filtered Accelerometer Signals at 2100 rpm	51
Figure 4.7 Comparison of Fourier-transformed Accelerometer Signals at 2100 rpm ..	51
Figure 4.8 Shifting Accelerometer Window To Determine Optimum Start Point	53
Figure 5.1 Effect of Gaseous Overfuelling on Perceived Knock Intensity	56
Figure 5.2 Effect of Pilot Reduction on Perceived Knock Intensity	56
Figure 5.3 Variation of Peak Combustion Pressure with Observed Knock Intensity ..	59
Figure 5.4 Variation of RMS Pressure With Bandpass Centre Frequency	61
Figure 5.5 Correlation of Maximum Filtered Pressure to Standard Knock Intensity, Using Various Data Window Lengths, 1500 rpm	63
Figure 5.6 Correlation of Maximum Filtered Pressure to Standard Knock Intensity, Using Various Data Window Lengths, 2100 rpm	63
Figure 5.7 Correlation of RMS Filtered Pressure to Standard Knock Intensity, Using Various Data Window Lengths, 1500 rpm	65
Figure 5.8 Correlation of RMS Filtered Pressure to Standard Knock Intensity, Using Various Data Window Lengths, 2100 rpm	65

LIST OF FIGURES (CONTINUED)

	PAGE
Figure 5.9 Correlation of Filtered Pressure FT Amplitude to Standard Knock Intensity, Using Various Data Window Lengths, 1500 rpm	67
Figure 5.10 Correlation of Filtered Pressure FT Amplitude to Standard Knock Intensity, Using Various Data Window Lengths, 2100 rpm	67
Figure 5.11 Statistical Dynamic Range Comparison, Pressure Investigation, 1500 rpm.....	68
Figure 5.12 Statistical Dynamic Range Comparison, Pressure Investigation, 2100 rpm.....	69
Figure 5.13 Correlation of Optimum FPmax Statistic to SKI, 1500 rpm	70
Figure 5.14 Correlation of Optimum FPmax Statistic to SKI, 2100 rpm	70
Figure 5.15 Correlation of FAm _{ax} to FPmax Using Various Data Window Lengths, Overfuelling Experiment, 1500 rpm.....	74
Figure 5.16 Correlation of FAm _{ax} to FPmax Using Various Data Window Lengths, Overfuelling Experiment, 2100 rpm.....	75
Figure 5.17 Correlation of FAR _m s to FPmax Using Various Data Window Lengths, Overfuelling Experiment, 1500 rpm.....	75
Figure 5.18 Correlation of FAR _m s to FPmax Using Various Data Window Lengths, Overfuelling Experiment, 2100 rpm.....	76
Figure 5.19 Correlation of FAamp to FPmax Using Various Data Window Lengths, Overfuelling Experiment, 1500 rpm.....	76
Figure 5.20 Correlation of FAamp to FPmax Using Various Data Window Lengths, Overfuelling Experiment, 2100 rpm.....	77
Figure 5.21 Accelerometer Statistic Dynamic Range Comparison, Overfuelling Experiment, 1500 rpm	79
Figure 5.22 Accelerometer Statistic Dynamic Range Comparison, Overfuelling Experiment, 2100 rpm	79
Figure 5.23 Correlation of FAm _{ax} to FPmax Using Various Data Window Lengths, Pilot Experiment, 1500 rpm.....	80
Figure 5.24 Correlation of FAm _{ax} to FPmax Using Various Data Window Lengths, Pilot Experiment, 2100 rpm.....	80
Figure 5.25 Correlation of FAR _m s to FPmax Using Various Data Window Lengths, Pilot Experiment, 1500 rpm.....	81

LIST OF FIGURES (CONTINUED)

	PAGE
Figure 5.26 Correlation of FArms to FPmax Using Various Data Window Lengths, Pilot Experiment, 2100 rpm.....	81
Figure 5.27 Correlation of FAamp to FPmax Using Various Data Window Lengths, Pilot Experiment, 1500 rpm.....	82
Figure 5.28 Correlation of FAamp to FPmax Using Various Data Window Lengths, Pilot Experiment, 2100 rpm.....	82
Figure 5.29 Accelerometer Statistic Dynamic Range Comparison, Pilot Experiment, 1500 rpm	84
Figure 5.30 Acceleration Statistic Dynamic Range Comparison, Pilot Experiment, 2100 rpm	84
Figure 5.31 Comparison of Best Block Acceleration and Cylinder Pressure Statistics, 1500 rpm	87
Figure 5.32 Comparison of Best Block Acceleration and Cylinder Pressure Statistics, 2100 rpm	88
Figure 5.33 Correlation of Best Acceleration Statistic to Best Pressure Statistic, With Suggested Knock Threshold Vibration Level, 1500 rpm	89
Figure 5.34 Correlation of Best Acceleration Statistic to Observed Knock Intensity, With Suggested Knock Threshold Vibration Level, 1500 rpm	89
Figure 5.35 Correlation of Best Acceleration Statistic to Best Pressure Statistic, With Suggested Knock Threshold Vibration Level, 2100 rpm	90
Figure 5.36 Correlation of Best Acceleration Statistic to Observed Knock Intensity, With Suggested Knock Threshold Vibration Level, 2100 rpm	90
Figure A.1 Pressure Transducer Calibration Curve	103
Figure A.2 Binary Pressure Signal “Pegging”	105

LIST OF NOMENCLATURE

ACT	air charge temperature
A/D	analogue-to-digital convertor
AFS	Alternative Fuel Systems Inc.
ATDC	after top-dead-centre
BTDC	before top-dead-centre
c	velocity of sound
C	correlation coefficient
CFR	Cooperative Fuel Research
CH ₄	methane
CNG	compressed natural gas
CO ₂	carbon dioxide
D	cylinder diameter
ECM	engine control module
ECT	engine coolant temperature
f	(knock) frequency
FAamp	filtered acceleration Fourier transformed peak amplitude
FAMax	maximum filtered acceleration
FARms	root-mean-squared deviation of filtered acceleration
FPamp	filtered pressure Fourier transformed peak amplitude
FPmax	maximum filtered pressure
FPrms	root-mean-squared deviation of filtered pressure
FT, FFT	Fourier transform, Fast-Fourier transform
g*	units proportional to the earth's acceleration, g
MAP	manifold absolute pressure
NMHC	non-methane (reactive) hydrocarbons
NO _x	oxides of nitrogen
OM366LA	Mercedes turbocharged 5.958-litre diesel / dual fuel engine

LIST OF NOMENCLATURE (CONTINUED)

P_{\max}	maximum pressure
SKI	Standard Knock Intensity (scale)
TDC	top-dead-centre
THC	total hydrocarbons
TPS	throttle position sensor
w	window width (in crankshaft degrees of rotation)
ξ_m	non-dimensional mode shape factor

CHAPTER ONE

INTRODUCTION

1.1 Preamble

This investigation concerns a series of experiments conducted with a Mercedes OM366LA turbocharged diesel bus engine. The engine was converted to “dual fuel” operation by the installation of a fuel control computer and a compressed natural gas injection system. Dual fuel engines have been developed to achieve a variety of economic and environmental benefits. However, at high engine loads the gas/air mixture in the far reaches of the combustion chambers is susceptible to a potentially destructive, extremely rapid combustion phenomenon called knock. The purpose of this study is to observe and quantify the intensity of end-gas knock in a dual fuel engine using intrusive and non-intrusive knock detection techniques.

1.2 Environmental and Economic Concerns of Current Diesel Engines

The backbone of urban life and industry in the twentieth century is transportation. The ready delivery of goods from producer to consumer and the mass transportation of people in population-dense cities are vitally important to the way our global society operates.

Traditionally, transit buses and delivery vehicles have relied on diesel engines for locomotive power. Diesel engines are particularly well-suited for this task because they have high thermal efficiency, suitable torque characteristics, and utilize a relatively safe

and energy-dense fuel. Furthermore, diesel engine technology is backed by over a century of research, development, experience, and infrastructure.

However, concern for the environmental impact of fossil-fuel combustion is rapidly increasing. As a result, governments around the world are tightening their standards for acceptable vehicular emissions. For operators of truck and bus fleets, this often means that large numbers of vehicles are facing either engine upgrades or complete replacement to comply with the new standards.

Anyone who has ever walked or driven beside a diesel-powered bus in congested traffic is acutely aware of the drawbacks of diesel combustion. Engine exhaust is particularly high in soot and particulate matter, as evidenced by the black clouds that frequently emanate from truck and bus mufflers. As well, partially burned aromatic hydrocarbons (such as ketones and aldehydes) attack the eyes and soft-tissue membranes of humans. Oxides of nitrogen (NO_x) and non-methane hydrocarbons (NMHC) interact in the atmosphere to form photochemical smog and ground-level ozone, both of which are unpleasant or even toxic to people and wildlife. To a lesser extent with diesel engines, odourless and colourless carbon monoxide is a dangerous ground-level toxin.

One of the primary products of hydrocarbon combustion is carbon dioxide (CO_2). Scientists believe that CO_2 acts as a “greenhouse gas” that traps solar radiation at the earth’s surface and contributes to the “global warming” phenomenon. The burning of petroleum-based fuels by the transportation sector of industry is believed to be a significant source of CO_2 emissions [1,2].

Apart from these environmental concerns, there are economic factors that also cast a shadow on the future of diesel engines. With the explosion of industry in the developing world, global consumption rates of liquid fossil fuels continue to increase. In the foreseeable future, it seems inevitable that crude oil shortages will put pressure on the

cost of diesel fuel. It is also possible that international politics will again result in temporary (or longer) shortages of foreign crude oil feedstocks for diesel fuel production. National governments and transport companies alike can protect themselves from these problems by starting to diversify their fuel requirements today.

1.3 Alternative Fuels for Compression-Ignition Engines

Since the oil shortages of the 1970s, there has been a great deal of research in North America and Europe regarding alternatives to crude oil-refined fuels. Thus far, no fuel has been able to capture more than a small piece of the market dominated by gasoline and diesel. There are various reasons for this resistance to new technology. Firstly, a full century of gasoline and diesel technology carries a great deal of momentum, and implementation of most alternative fuels on a large scale would require an immense capital outlay for new infrastructure. Furthermore, one of the greatest advantages of liquid fossil fuels is their high energy density. Vehicular range often extends to several hundred kilometres or more with only a 70 - 100 litre fuel tank on board. For example, a full 100 litre diesel fuel tank contains enough energy to lift a typical 17.5 tonne [3] fully-loaded public transit bus, *straight up*, more than 22 kilometres. Finally, oil-derived fuels (especially diesel fuel) are relatively safe and easy to handle compared to most of the proposed alternative fuels. Diesel fuel is readily transported and stored at atmospheric pressure in its liquid state, and spills do not tend to ignite and burn rapidly, if at all.

Liquid ethanol and methanol have been proposed as realistic alternatives to fossil fuels. Table 1.1 shows that both alcohols have about half the energy density of diesel fuel, and can be transported and stored as liquids at or near atmospheric pressure. Ethanol is often derived from non-fossil fuel sources through the distillation of grains and biomass. Methanol can also be produced from non-petroleum sources, but is more economically manufactured from natural gas or coal gas liquefaction. Compared to diesel fuel, methanol is a relatively dangerous substance since it is toxic, readily adsorbed through

the skin, and bursts into colourless flames with low ignition energy. In addition, methanol has poor lubricity properties and is relatively corrosive, and thus requires extensive fuel system development for use in conventional engines. Finally, neither alcohol burns particularly well in high-torque compression-ignition engines, and at this time the relatively high cost of these fuels is prohibitive to their development [4,5].

Table 1.1 Storage Properties of Selected Transportation Fuels [3,4,6]

Fuel	Diesel Fuel (summer)	Ethanol	Methanol	Hydrogen	CNG
Vapour or Storage Pressure (kPa)	0.15	15	18	20,000	20,000
Density* at 15°C (kg/L)	0.855	0.79	0.79	0.0076	0.15
Energy Content* (LHV basis) (MJ/kg)	42.5	26.8	19.7	120.0	47.7
Volumetric Energy Content* (MJ/L)	36.3	21.2	15.6	0.9	7.2
Safety Concerns	flammable	flammable	toxic, highly flammable, colourless flame	highly explosive, very wide flammable range	flammable pressure leaks

* denotes properties at listed vapour or storage pressure

Another alternative fuel that has been investigated recently is hydrogen. Ideally, the combustion of hydrogen in air leads to extremely “clean” emissions - water vapour, oxygen, and nitrogen. But, due to its very low energy density, gaseous hydrogen must be stored under high pressure in a very large, heavy vessel to provide a range of travel comparable to that of a fossil-fuelled vehicle. The inevitable impact of conventional on-

board hydrogen storage is either greatly reduced utility when large, heavy pressure cylinders are installed or crippled vehicle range with smaller tanks. Carrying a sizable amount of hydrogen also introduces serious safety concerns, especially considering the wide flammable range of hydrogen gas and its vigorous combustion in air. Until fuel storage and transportation issues are adequately addressed, hydrogen is unlikely to become a viable alternative vehicular energy source [7].

This leaves us with the option of using a cleaner-burning hydrocarbon fuel such as compressed natural gas (CNG). Conventionally, natural gas is comprised of approximately 95 percent methane and small amounts of ethane, propane, nitrogen, and carbon dioxide. Like all alternative fuels, natural gas has certain disadvantages compared to diesel. The main drawback of CNG is its relatively low energy density. Stored as a compressed gas in a heavy cylinder, natural gas occupies much more space than an energy-equivalent (and much lighter) diesel fuel tank. Table 1.1 suggests that the volumetric energy density of compressed methane is about one-fifth that of diesel fuel. This limits the automotive use of natural gas to vehicles which have the load capacity and space to carry one or several high-pressure cylinders. As a result, CNG technology is most often utilized in large trucks and buses which can be modified to accommodate the added space and mass of gaseous fuel storage.

Natural gas is particularly useful in spark-ignition engines due to its high knock resistance. The Motor Octane Number for typical natural gas supplies is well over 120 [8]. As such, CNG is not as well suited for use as a sole compression-ignition fuel, since it is relatively difficult to autoignite. However, by injecting a small "pilot" quantity of diesel through the conventional fuel injection system, CNG can be burned quite well in a "dual fuel" high-compression engine.

1.4 Dual Fuel Technology

The concept of burning natural gas in a diesel engine, while not in wide practice today, is certainly not a new idea. Rudolf Diesel himself patented a compression-ignition engine running on the dual fuel principle almost 100 years ago [9]. Since then, there have been a number of surges in interest by researchers and developers.

Today, a limited number of dual fuel engines are being used around the world in a variety of configurations. Usually, the technology is based on an ordinary diesel engine retrofitted with natural gas injection and control equipment. One conversion method injects CNG through multiple high-speed valves in the engine's intake manifold. The gas/air mixture is then inducted into each cylinder and compressed. Near top dead centre, the mixture is ignited with a small burst of diesel fuel delivered through the conventional high-pressure diesel injector.

Since the gas/air mixture is considerably lean of stoichiometric, dual fuel engines have a number of attractive advantages. The inherently high octane number of natural gas usually allows its combustion in a high-compression diesel engine without knock. Ordinary diesel combustion is limited by the rate at which unburned diesel fuel droplets can vapourize and find fresh oxygen molecules. Dual fuel combustion occurs more quickly after the initial injection point, thereby burning with higher thermal efficiency and creating more power than the equivalent diesel-only cycle. This increase in fuel efficiency helps to reduce the impact of adding natural gas cylinders to the weight of the vehicle.

The nature of dual fuel combustion similarly leads to reductions in key exhaust emissions. Most importantly, premixed methane burns by a much cleaner, more complete process than long-chain diesel molecules. This greatly reduces the amount of soot and thermally "cracked", reactive hydrocarbons that are emitted by the engine. In addition, natural gas burns at a slightly lower temperature than diesel fuel, resulting in

lower NO_x formation via the thermal Zeldovich mechanism [10]. The combination of reducing NO_x and reactive hydrocarbons helps lower the potential for photochemical smog formation in urban centres. Since natural gas is stored as a compressed vapour, evaporative losses from the fuel system are virtually non-existent compared to volatile liquid fuels. Finally, methane (CH_4) has a lower relative carbon content than long-chain paraffins, resulting in less CO_2 formation for a given amount of engine power [11].

Apart from key emissions reductions, there are economic advantages to dual fuel technology. Compared to proven crude oil reserves, natural gas supplies are well distributed around the world. Many countries of the Pacific Rim, for instance, do not have domestic oil production but do have domestic natural gas fields. By replacing most of the foreign-derived diesel fuel that their truck and bus fleets use with locally produced natural gas, countries can spend their import dollars on something other than crude oil. As well, there is a strategic advantage to diversifying the fuel requirements of the transportation industry, even if natural gas must be imported. Historically, the worldwide price of natural gas has shown greater stability than that of crude oil, mainly because gas transportation requires a large infrastructure of pipelines. Substituting the relative stability of natural gas for the volatile nature of world oil trade is an excellent way for a country to insulate itself against foreign political crises.

In order to obtain this strategic advantage while reducing the impact of vehicle emissions, several governments have tightened their environmental regulations for conventional automotive exhaust. Fleets powered by old diesel technology are becoming obsolete and illegal to operate. Truck and bus operators must either upgrade or replace their engines to remain in compliance with the law. Installation of a brand-new, modern technology engine in an old chassis is often not economically feasible. As a result, fleets are usually faced with the choice of retrofitting their existing engines or replacing the entire vehicle. If an operator elects to replace entire trucks or buses at the typical rate of 5 to 10% a year, it could take up to twenty years to overhaul the fleet. This postpones the full benefits of

the upgrade into the future while the fleet is burdened with paying for most of the refuelling infrastructure immediately. The benefits of lower NO_x and NMHC emissions might be completely overshadowed by the normal growth rate of the fleet under this sort of replacement scheme. As a result, it is advantageous to use a bolt-on dual fuel conversion kit to bring old engine technology quickly into compliance with modern standards [11].

Conversion systems must meet several criteria to be attractive to fleet owners. Most importantly, the converted vehicle must retain its previous utility. A dual fuel engine must exhibit similar torque and power characteristics to its base diesel engine if driveability is to be maintained. To remain flexible, the converted engine must be able to quickly revert to ordinary diesel operation. This allows the fleet operator to switch back to diesel operation at times when natural gas is temporarily unavailable or not cost-effective. As well, diesel-only capability can provide range extension for occasional long trips. Resale value is maintained as long as the conversion kit is relatively non-intrusive and can be easily removed. The conversion equipment must be robust and well-designed to ensure that vehicle reliability is not affected. Finally, the initial capital outlay for the conversion must be paid back quickly by savings in fuel cost or other incentives if the retrofit is to be economically attractive.

1.5 Conversion of a Mercedes OM366LA Engine

In this project, an engine typical of medium-duty delivery trucks and transit buses in South America was chosen for dual fuel conversion. The engine was a Mercedes OM366LA turbocharged, inline-6 cylinder powerplant originally built in Brazil. The dual fuel conversion kit was designed by Alternative Fuel Systems (AFS) Inc. of Calgary, Alberta and was developed for use with the OM366LA jointly by AFS and the University of Alberta. The three main features of the conversion kit are its natural gas injectors, pump actuator, and control computer. Gas is injected sequentially into the intake

manifold near each cylinder through high-speed valves. Control of the stock diesel fuel pump is assumed by an electronic actuator. Operating conditions are monitored by a engine control module (ECM) which coordinates the natural gas and diesel fuelling systems. The AFS conversion kit is examined in greater detail in Section 3.1.

This engine is a prime candidate for dual fuel conversion for a number of reasons. Firstly, it is extensively used in several major South American cities as a transit bus engine. The governments of cities like Santiago, Buenos Aires, and Rio de Janeiro are determined to alleviate their smog and airborne pollutants problems. Also, the utility of transit buses is not adversely affected by the weight and size of retrofit compressed natural gas cylinders. Due to the high number of OM366 engines in use, conversion of this engine provides a great opportunity to make an impact on local pollution. As well, many of the OM366 engines on the road today are not “old” engines by fleet standards, but they will not meet proposed exhaust emissions standards. Retrofitting these engines with dual fuel conversion kits makes good economic and environmental sense.

The reliance on public transportation in the crowded cities of South America is one of the reasons why their governments are looking for alternative fuel choices. However, some of the specific conditions of the South American market lead to a potentially serious problem with dual fuel combustion. As mentioned previously, the high octane number of methane and the relatively lean gas/air mixture inducted into the combustion chambers of a dual fuel engine tend to prevent end-gas autoignition or “knock”. Under normal conditions, an engine control computer is set up to prevent knock by limiting diesel replacement at high torque to a safe level. This presents a tradeoff between the emissions and fuel cost benefits of high fuel replacement and the anti-knock protection of lower replacement ratios. Under controlled laboratory conditions, 75 to 80% replacement of diesel fuel (on an equivalent energy basis) has been routinely available at full torque. As such, the control maps of the ECM have been set up to provide this high level of replacement.

Unfortunately, there is no guarantee that the operating conditions of an engine will be anywhere near as well-controlled underneath a typical South American bus. One of the biggest concerns is the composition of locally-available natural gas. In North America, supplies are typically very consistent, and the volumetric methane content of natural gas hovers above ~ 94%. In Argentina and Brazil, however, the ethane and propane content can be significantly higher. This lowers the overall octane number of the natural gas supply, and can lead to the onset of knock in dual fuel engines. Additionally, the full-torque calibration of mechanical fuel pumps in the field can vary by as much as 10 percent from vehicle to vehicle. Those engines that happen to have a greater amount of diesel fuel being delivered to each cylinder than the test engine may also have a higher tendency to knock. The close confines of a transit bus's engine compartment has other negative effects. Drawing in fresh air at a significantly higher temperature than test conditions will lead to higher temperatures at the end of compression and a greater tendency for dual fuel engines to knock. OM366 engines outfitted with a turbocharger for extra power have an air-to-air heat exchanger to cool the air after the compressor. Obviously, this air-to-air exchanger will not work as effectively as in laboratory trials if the intercooler is buried in the back of a hot, dusty, poorly ventilated engine compartment. To achieve the optimum balance of fuel replacement and knock protection under these circumstances, it is vital that the control system be able to push the replacement ratio to (but not beyond) the limits of knock. This requires some form of closed-loop knock control and, hence, a reliable knock detection system.

1.6 Knock Detection and Control

Knock in the context of a dual fuel engine is defined as the rapid autoignition of a region of fuel/air mixture ahead of the propagating turbulent flame front. In spark-ignition research, the prevailing theory of knock is that unburned gas ahead of the advancing flame front is compressed to an unstable condition where the mixture undergoes rapid self-ignition at one or more locations [12]. It is believed that knock occurs in dual fuel

engines by much the same process, since both cases feature premixed fuel/air mixtures surrounding an initial ignition point. The main difference is that in a spark-ignition engine, the fuel/air mixture is often stoichiometrically correct or slightly fuel-rich, with a high tendency to knock at full torque. Dual fuel engines, on the other hand, are usually conversions of diesel engines, and their lean end-gas mixture of CNG and air is relatively knock-resistant, even at high compression ratios. For reasons of economics and many others, almost all of the knock detection research conducted in the past century has focused on spark-ignition engines.

The most obvious physical feature of the knock phenomenon is a distinct “pinging” sound. This sound is generated by a pressure or shock wave racing from the point of autoignition to the opposite side of the cylinder and back again, bouncing from one wall to another at approximately sonic velocity. While waves can and do reverberate in a number of complicated directions in a combustion chamber, it is believed that the primary mode of vibration is transverse [13]. For a typical heavy-vehicle engine with a 10 - 15 centimetre cylinder bore, this usually corresponds to a vibration frequency of about 5000 - 8000 Hertz. Since each knock event happens very quickly (within a few milliseconds) the mid-frequency tone is perceived by the human ear as a series of sharp, metallic “ticks” or “pings”.

If knock is allowed to occur unchecked in an engine, disastrous results often occur. The presence of extreme pressures inside the combustion chamber greatly increases heat transfer into the piston, head, and cylinder liners. In some cases, pistons or valves will thermally expand enough to temporarily or permanently seize the engine or valvetrain. In more extreme cases, piston crowns melt and overheated liners tear away from the block, leading to a complete physical failure of the engine. As well, localized shock waves can collide with and destroy piston rings and ring lands. Finally, the knock is a self-intensifying process. As an engine begins to knock, cylinder components get hotter and hotter, which further heats the end gas regions and increases their tendency to autoignite.

Thus, it is important that the onset of knock be detected and remedied quickly to prevent damage to the engine.

The most accurate, reliable way of detecting knock is with the use of pressure sensors that extend into the combustion cavity. Knock can be detected and even quantified by careful analysis of observed pressures. A great deal of knock research has been conducted in the past with laboratory engines outfitted with one or more in-cylinder transducers, including the work of Karim *et al* [14] and Draper [15]. Since pressure transducers directly measure the physical process of knock, they are widely considered to be the most accurate quantitative indicator of knock. However, outside of the laboratory it is not feasible to outfit every engine with a transducer in each cylinder. Pressure transducers are electronic devices which must be very small but extremely rugged, which makes them relatively expensive. It is also inconvenient (or even impossible) to drill an access hole into every combustion cavity of a typical motor. Engine blocks and heads are designed to be strong enough to withstand the high pressure forces of normal combustion, while providing access to combustion chambers for valves and injectors. Drilling an extra hole into each cylinder of an engine not designed for additional holes weakens its structural integrity. Finally, once an engine has been permanently modified, simply removing the transducers does not return the engine to its original state. This may negatively effect the vehicle's future resale value. Clearly, knock detection in practical field applications requires a less intrusive sensor.

When knock-induced pressure waves slam into the cylinder walls, their momentum causes the walls to vibrate. This energy is transmitted through the engine block to other structural components of the engine. End-gas autoignition can be detected by monitoring the sympathetic vibration of certain points on the block with an accelerometer. The onset of knock appears as an increase in acceleration amplitude at the characteristic knock frequency. In spark-ignition engines where energy release rates are much higher than normal combustion, the difference in amplitude is relatively easy to detect. The

difference is more subtle in dual fuel engines, where even normal combustion begins with a period of energetic diesel fuel autoignition. Compression-ignition engines are built much heavier and stiffer than spark-ignition ones to accommodate higher compression ratios. This may make the detection of changes in vibration amplitude even more difficult. Normal mechanical events, such as valve openings and closings, also cause the block to vibrate. To pick out knocking vibration from the background noise of a dual fuel engine, the accelerometer must be carefully analyzed during the appropriate “window” of each combustion cycle when knock is expected to occur.

Accelerometers have been successfully used as knock control devices in mass-production domestic automobiles for over a decade. Conventionally, one or more piezoelectric sensors are bolted to the engine, and their output is monitored by the engine control computer. The computer filters the incoming signal during a particular analysis window, and integrates the signal. When the result of integration is above a predetermined threshold value for that particular engine speed and load condition, the control system is alerted to the onset of knock.

In spark-ignition engines, knock is eliminated by retarding spark timing to lower the peak combustion pressure. The equivalent control scheme in a dual fuel engine would be to retard ignition by delaying the starting point of pilot injection. However, in a dual fuel engine equipped with a standard mechanical fuel pump, it is not possible to make closed-loop adjustments to pilot injection timing. As a result, the most effective way of eliminating knock is by increasing the diesel fraction of the overall energy budget. Increasing the pilot fraction makes the gas-air mixture further fuel-lean, reducing its tendency to autoignite. Using a knock detecting signal as feedback, a dual fuel ECM can hold the diesel replacement at a high but safe level.

1.7 Study Objectives and Approach

A Mercedes OM366LA diesel engine was selected for dual fuel conversion by Alternative Fuels Systems Inc. of Calgary. Development of this dual fuel conversion kit is strategically aimed at the South American market, where a large number of these engines are in use by transit bus fleets. To prevent the possibility of severe end-gas autoignition during field use of converted engines, AFS and the University of Alberta are developing a strategy to detect and quantify knock in a dual fuel OM366LA engine. The objective of this research is to study the ability of intrusive and non-intrusive sensors in the detection of dual fuel knock.

A brief survey of the findings of other knock researchers will be presented in Chapter 2. Following that, the experimental equipment and knock detection sensors will be discussed in Chapter 3. Chapter 4 will concern the methodology of quantifying and interpreting sensor outputs, and will discuss techniques for digitally processing pressure and block acceleration records. Results of various knock intensity experiments with different sensors will be presented and discussed in Chapter 5. Finally, Chapter 6 will draw conclusions from the findings of this research project, and will evaluate the suitability of block vibration sensors for knock detection in dual fuel engines.

**SURVEY OF DUAL FUEL ENGINE
KNOCK RESEARCH**

2.1 History of Fundamental Knock Research

Engineers and scientists have studied the phenomenon of knock in internal combustion engines for most of the twentieth century. Some of the earliest studies have been attributed to Midgely and Boyd [16] who published results of knock experiments in 1922. During the subsequent three-quarters of a century, a wealth of knowledge has been amassed about the physical processes that accompany end-gas autoignition. However, to this day there is still no complete fundamental explanation of the knock phenomenon for the full range of engine conditions in which it occurs.

According to Heywood [17], it is generally agreed that knock occurs when energy is released extremely rapidly by the fuel/air mixture ahead of the propagating turbulent flame front. This energy release can occur at one or more locations in the end-gas region for any particular combustion cycle, resulting in localized high-pressure areas. Driven by the resulting non-uniform pressure distribution, pressure or shock waves reverberate across the combustion chamber. When the pressure waves are sufficiently energetic, they cause the cylinder to resonate at one or more fundamental frequencies. In turn, this energy is transmitted throughout the engine block and into the air surrounding the motor. The distinctive “pinging” or “knocking” sound heard by human bystanders gives the phenomenon its name.

Two different theories were proposed to explain the actual origin of knock [17]. One school of thought contended that under certain conditions, the normal turbulent flame front accelerates to sonic or slightly supersonic velocity, consuming the reactants in the end-gas regions much more rapidly than normal. The other theory suggests that when the fuel/air mixture ahead of the flame front is excessively heated by the compression of the approaching flame front, the mixture autoignites. Recent high-speed schlieren and natural light photography of knocking combustion has provided convincing evidence for the widely-accepted autoignition theory [18, 19].

The resonance characteristics of knock in spark-ignition engines were first studied by Draper [15] in the 1930s. Draper investigated the acoustical properties of a combustion chamber using mechanical pressure transducers in a Cooperative Fuel Research (CFR) engine. In his analysis, the combustion chamber was assumed to be a right-circular cylinder with plane ends, shaped like a “hockey puck” or “pancake”. By calculating solutions to the wave equation, Draper was able to identify three modes of knock travel. First, the azimuthal (or circumferential) mode was considered, where a nodal plane between high and low pressure forms along a cylinder diameter. A radial mode was also defined such that the node took the shape of a cylinder concentric with the piston’s longitudinal axis. Finally, an axial mode was considered, with a nodal plane perpendicular to the cylinder’s axis. Figure 2.1 schematically outlines Draper’s simplest, most dominant resonance modes as they were later revisited by Hickling *et al* [13].

The first circumferential mode of Figure 2.1 is excited when knock occurs near the cylinder wall and forms a local high-pressure, high temperature zone. A pressure or shock wave races away from this point, and travels across the full diameter of the cylinder, parallel to the crown of the piston. The wave collides with the opposite wall and reflects to the original knock region.

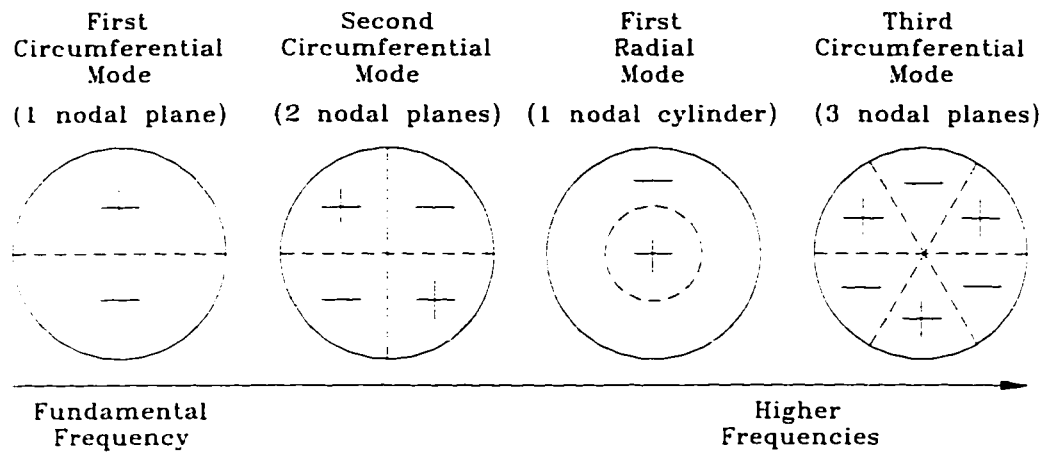


Figure 2.1 Primary Transverse Knocking Modes for a “Hockey Puck” Combustion Chamber (adapted from [13])

Theoretically, the fundamental resonance distance is simply the bore of the cylinder. The resonance frequency of any mode of knock can be determined from Equation 2.1.

$$f = \xi_m \cdot \frac{c}{D} = \xi_m \cdot \frac{\sqrt{k \cdot R \cdot T}}{D} \quad (2.1)$$

where:

- f = the knock frequency (Hz)
- ξ_m = non-dimensional mode factor
- c = speed of sound through combustion products (m/s)
- D = cylinder bore (m)
- k = ratio of specific heats of combustion gases
- R = combustion gas constant (kJ/kg-K)
- T = bulk gas temperature in cylinder (K)

From Equation 2.1 it follows that the resonance frequency increases directly with the speed of sound and inversely with bore diameter. Because of the square root function in the determination of the speed of sound, resonance frequency is a relatively weak function of bulk gas temperature and the temperature-dependent specific heat ratio [20].

It has been shown countless times that for gasoline combustion in air, the first circumferential mode knock frequency for a typical vehicle engine cylinder usually falls somewhere between 5 and 10 kHz. Knock in other circumferential and radial modes has also been observed at higher frequencies, but the simple cylinder-crossing path is generally the most apparent knocking mode. Since knock usually occurs very close to top-dead-centre where the piston is close to the “roof” of the chamber, axial modes would have a very high frequency. This mode is rarely observed, and is only measurable in very low-compression engines.

A finite element analysis of diesel engine combustion cavities has been carried out by Hickling *et al* [13]. These researchers have determined the non-dimensional mode factors ξ_m for the combustion space above a typical direct-injection diesel piston. Figure 2.2 shows the FEA results for a piston equipped with a slightly off-centre toroidal bowl. Because of the non-symmetries in bowl location, there are two different nodal planes. The fundamental knock frequencies can be calculated by substituting the appropriate ξ_m and an estimate of bulk combustion temperature into Equation 2.1.

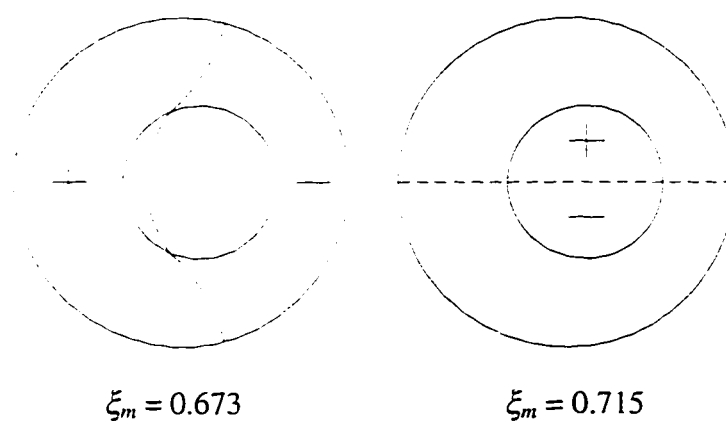


Figure 2.2 Fundamental Nodal Lines for Diesel Combustion Chamber
(adapted from [13])

Many researchers have attempted to verify Draper's modal predictions and resolve the debates over the initiation process of knock. Recently, Liiva *et al* [21] have used multiple pressure transducers and a triangulation scheme to determine the location of knock in a CFR engine. However, there are a number of other techniques that are better suited for determining the exact knock initiation point (or points). When autoignition occurs, the rapid consumption of fuel releases a great deal of energy. This violent level of combustion tends to be much brighter than a normal turbulent flame front [17]. As a result, several researchers have used high-speed photography to record knocking combustion in optical access engines. Schlieren and natural light images of knock in a Yamaha motorcycle engine have been published by König and Sheppard [18]. Through sequences of photographs, they showed that during knock one or more small pockets of fuel/air mixture autoignited and brightly burned. This research has led most people in the research community to discount the flame acceleration / detonation theory in favour of the rapid end-gas autoignition concept. More recent work by Witze and Green [22] has used ionization probes built into the engine's head gasket to locate the origin points of knock. Further correlations to schlieren imaging have been achieved by Spicher *et al* [23] through the use of multiple optical fibres. By studying the location of autoignition "hot spots" in prototype engines, designers can avoid chamber shapes with a high tendency to knock.

Aside from locating exothermic ignition centres, combustion pressure records are often used to measure the relative intensity of knock. A wide variety of pressure statistics have been proposed for gauging knock intensity, many of which have been comparatively evaluated by Puzinauskas [24]. The simplest measure of knock is the value of peak combustion pressure. When a cylinder is knocking, the maximum pressure tends to climb higher than that of normal combustion. However, the value of normal peak pressure varies widely between different operating conditions for the same engine. Therefore, interpreting absolute peak pressures as knock is fairly troublesome. A more effective way of analyzing the pressure signal involves extracting the fluctuating

pressures of knock from the gross low-frequency offset of normal combustion pressure. This is accomplished by passing the pressure record through an analogue or digital high-pass or band-pass filter. Once filtered, researchers such as Chun and Heywood [25,17] declare the maximum amplitude of oscillation to be a value proportional to knock intensity. Others prefer to take the analysis one step further, and integrate the fluctuating amplitudes over a discrete time window [26]. Similar to the integration technique, König and Sheppard used a summation of root-mean-squared (RMS) deviations from mean filtered pressure as their knock intensity factor [18].

Yet another school of thought concentrates on pressure derivative methods. Several techniques have been proposed that focus on the slopes and inflection points of the gross pressure curves instead of the pressure fluctuations. Classical experiments by Karim *et al* [14] considered the rate of pressure rise in the early stages of combustion to be a good indicator of knock intensity in dual fuel engines. Puzinauskas attributes the use of another first-order pressure derivative to Valtadoros *et al* [27], who set the threshold of knock at a rise of three bars pressure in one crankshaft degree of rotation. A more elaborate technique was proposed by Checkel and Dale [28,29,30] and implemented by Ando *et al* at Mitsubishi [31]. Three successive derivatives of a carefully-filtered pressure trace were calculated. During knock in spark-ignition engines, sharp inflection points appear in the pressure trace that distinguish it from the comparatively smooth rise and fall of normal (non-knocking) combustion. The application of three derivatives accentuates the discontinuities while attenuating the rest of the pressure signal. Through testing of a four-cylinder Ford production engine, Checkel and Dale demonstrated a strong correlation between the maximum negative value of the third derivative of pressure and observed knock intensity. Unfortunately, the third derivative method breaks down when it is applied to engines utilizing fuels that normally combust rapidly, such as the hydrogen engine research of Rosseel and Sierens [32]. Similarly, the third derivative technique will not work well for CI engines, given the sharp inflections points inherent to the normal combustion process.

The exponential progress of computer technology in recent years has revolutionized the analysis of pressure records. A small, inexpensive computer now has the computational power to digitally filter pressure signals and examine their spectral content using Fourier transform (FT) and fast-Fourier transform (FFT) techniques. In this way, the fundamental knocking frequency of a particular combustion chamber can be identified simply by examining the pressure's transform in the frequency domain. This technique quickly and accurately determines the most appropriate band-pass filter parameters for use with the pressure analysis techniques described previously.

In the past decade, in-cylinder transducers have been developed that work in concert with on-board computers in mass-production vehicles. Herden and Küsell [33] of Bosch GmbH have recently published the results of their progress with a new Combustion Pressure Sensor (CPS). The pressure output of this in-cylinder piezoresistive device can be used to detect engine knock, misfires, and roughness. Kusakabe *et al* [34] are developing a similar piezoelectric transducer in Japan. While the intent of these devices is to bring in-cylinder technology to the world of mass-production engines, they still are handicapped by several intrinsic properties. Firstly, all piezoelectric sensors are inherently prone to thermal drift. Directly exposing a crystal to the extreme heat and pressure of knocking combustion causes the sensor's output to quickly shift, making absolute pressure determinations difficult. As well, piezoelectric pressure transducers are susceptible to electrical noise interference since their output signals are proportional to extremely low-level variations in capacitance. Moreover, most engine blocks in production today were not designed to accommodate transducer access to each combustion chamber. It is often very difficult to retrofit current production engines with in-cylinder sensors without structurally weakening the block or interfering with the engine's valve train, water jacket, and fuel delivery system. Finally, each piezoelectric sensor design requires that a delicate crystal element be packaged in a necessarily small, yet extremely rugged, housing capable of prolonged exposure to the extreme environment

of combustion gases. This difficult engineering problem has so far made pressure transducers prohibitively expensive for mass-production use, especially when one considers that a separate sensor is required for each cylinder.

2.2 Non-Intrusive Knock Detection in Production-Volume Engines

Engineers have known for decades that knocking pressure fluctuations are detectable from outside the combustion chamber. When a knocking cylinder begins to resonate, energy is transmitted throughout the engine block. This causes certain parts of the block's surface to vibrate at the characteristic knock frequency with greater than normal amplitude. The most common way of detecting this vibration is to install one or more piezoelectric vibration sensors (i.e. accelerometers) at suitable locations [17]. Accelerometer output is monitored by an engine control module (ECM), which bandpass filters the sensor's signal to attenuate background noise. The filtered signal is analyzed within a measurement window synchronized to the crankshaft to further minimize noise. The acceleration signal can be electronically rectified and integrated to determine a value proportional to knock intensity [35,36]. Real-time integral output is then compared to threshold values from non-knocking combustion at the same operating conditions to determine whether knocking is occurring [3].

Numerous types of accelerometers are currently employed in production vehicles and development laboratories. The fundamental difference between various vibration sensor designs is their response characteristics. Flat response accelerometers have relatively linear output across a wide frequency band. This enables the same sensor to be used on multiple engines with different characteristic knock frequencies, as demonstrated by Dues *et al* [37]. However, the signal from wide-band accelerometers must be carefully filtered and processed to detect the noise of knocking combustion amid the relatively high level of background noise. Spike-resonant vibration sensors are tuned to one particular frequency, which greatly improves their characteristic signal-to-noise ratio. One drawback of these instruments is their limited resonant range, which may be less

than 100 Hz. This makes spike accelerometers susceptible to manufacturing and installation variances. They also are relatively insensitive to the normal cycle-to-cycle and cylinder-to-cylinder variance in knock frequency and intensity [17]. “Broadband resonant” accelerometers were designed as a compromise that combines the signal-to-noise ratio of spike sensors with the flatter frequency response of wide-band accelerometers. With a bandwidth of approximately 1 kHz, broadband resonant sensors have been used by many of the world’s automakers for more than a decade.

In the technical literature, many papers have confirmed the effectiveness of block-mounted sensors for knock detection in spark-ignition engines. For example, Chun and Kim [26] showed a direct correlation between knock intensities determined from in-cylinder pressure and external vibration records with a 4-cylinder gasoline engine. Kaji *et al* [38] have published results of their continued development of Toyota Motor Corporation’s knock control system. At the heart of their control logic is a broadband piezoceramic accelerometer, which is bolted to the middle of the engine block. When acceleration above a predetermined threshold occurs, the engine’s control computer slightly retards the spark timing. In this way, Toyota uses the sensor for closed-loop knock control.

The great majority of published work regarding non-intrusive knock sensing has focused on mass-production spark-ignition engines. This is partially due to the economics of scale, since gasoline engines are used in the majority of high-volume automobiles. Additionally, tightening emissions and fuel economy legislations have required automakers to push the limits of knock as they strive to improve thermal and combustion efficiencies. Diesel engine makers, who control the majority of the heavy vehicle market, do not experiment with knock detection methods in their heavier compression-ignition blocks since knock is not a concern in diesel combustion. Thus, there is virtually no published experimental data available to companies that convert diesel engines to dual fuel operation. The challenge facing dual fuel development is that the combustion

process is susceptible to knock like spark-ignition engines but more difficult to detect due to the heavier, stiffer compression-ignition block design. It has been left to research such as this project to investigate the suitability of non-intrusive knock detection in a dual fuel engine.

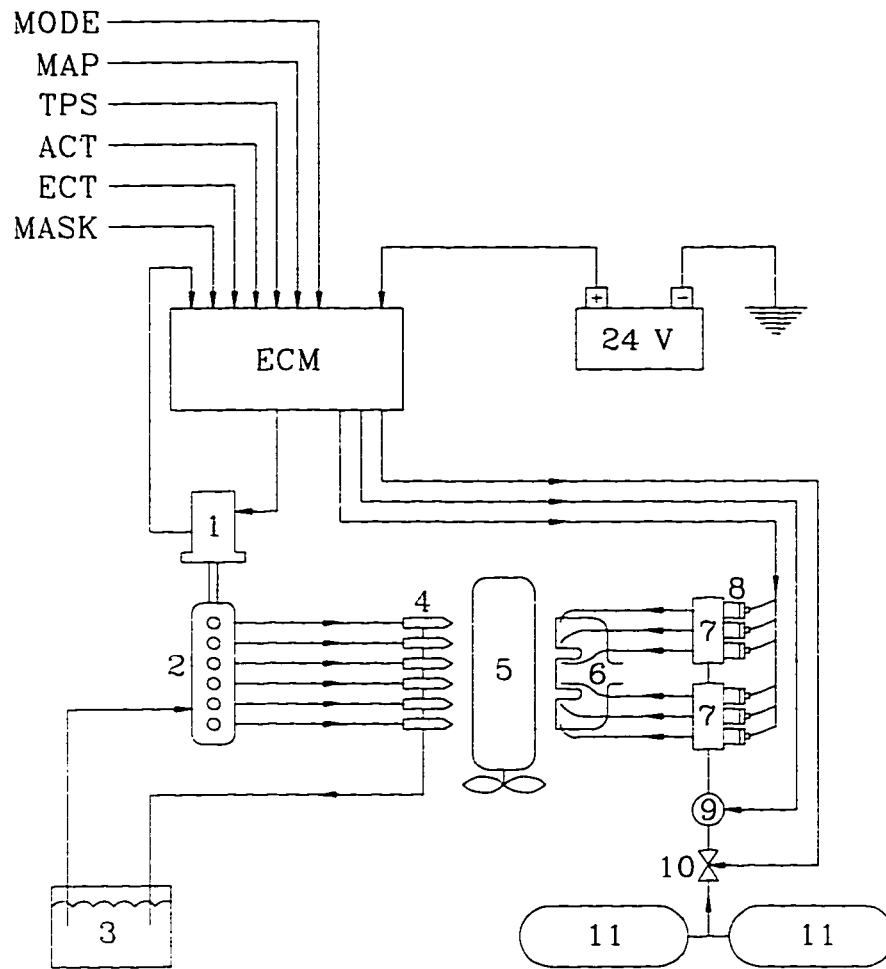
CHAPTER THREE

EXPERIMENTAL APPARATUS

3.1 The Test Engine

The central instrument of this research was a Brazilian-made Mercedes OM366LA inline-6 cylinder diesel engine. The bore and stroke are 9.75 cm and 13.30 cm respectively, giving a total engine displacement of 5958 cm³ [39]. The compression ratio is 17.4:1, typical of combustion-ignition vehicle engines. Maximum rated gross torque is 610 N-m at 1600 rpm, and maximum turbocharged power is 142 kW at 2400 rpm. Intake air is passed through an air-to-air intercooler after the turbocharger to cool the intake charge. High-pressure diesel fuel is timed and injected by a Bosch mechanical fuel pump, and fuel flow is limited by a variable-speed flyball governor. The OM366LA produces consistently high torque across most of its speed range, making it ideal for use in heavy vehicles that need to start and stop often (like transit buses).

This particular engine has been equipped with an Alternative Fuel Systems dual fuel conversion kit, as pictured in Figure 3.1. Natural gas is delivered from a pressure regulator to two machined-aluminum gas distribution blocks. Each block holds three high-speed solenoid valves [40], with one valve assigned to each cylinder for multi-port, sequential gas injection. When the high-speed valves open, gas is delivered from the distribution blocks to fittings on the intake manifold through steel-braided Teflon™



- | | |
|-------------------------|---------------------------|
| 1. ACTUATOR | 6. INTAKE MANIFOLD |
| 2. DIESEL PUMP | 7. GAS DISTRIBUTION BLOCK |
| 3. DIESEL FUEL TANK | 8. HIGH SPEED VALVES (6) |
| 4. DIESEL INJECTORS (6) | 9. SHUT-OFF SOLENOID |
| 5. OM366LA ENGINE | 10. PRESSURE REGULATOR |
| 11. CNG CYLINDER | |

Figure 3.1 Schematic of AFS Dual Fuel System

hoses. Control of the mechanical fuel pump is achieved by connecting the pump rack to an electronic actuator. An engine control module (ECM) coordinates the timing of natural gas injection and diesel rack actuation. At idle and low torque, an appropriate amount of diesel fuel is delivered to each cylinder by positioning the rack actuator accordingly. At moderate to high torque levels, the diesel flow is cut back to a minimum pilot level and the bulk of the input fuel energy is delivered by the natural gas injection system. By retaining the full capabilities of the original diesel pump, the engine can be switched back to diesel-only operation at any time with the flick of a switch.

The ECM relies on a number of sensory inputs to monitor engine performance. Commanded torque is sensed through the use of a throttle position sensor (TPS). A custom-made Hall-effect pickup “mask” on the fuel pump drive is used to determine engine speed and crankshaft position. Thermistors monitor the temperature of the engine coolant (ECT) and fresh air charge (ACT). Incoming air flow rate is induced by the speed-density technique; a Manifold Absolute Pressure (MAP) diaphragm and the ACT allow the ECM to infer manifold air density. To determine the optimum fuel quantities for every operating condition, the ECM employs several pre-programmed correlations and look-up tables.

A specially-designed shaft encoder allows the ECM to calculate engine speed and synchronize CNG injection to crankshaft position. A Hall-effect sensor detects the presence of a 12-tooth rotating mask affixed to the diesel pump drive gear. The resulting output resembles a square-wave with every second transition from low to high state corresponding to a cylinder TDC. Since the fuel pump rotates at one-half the engine rotation speed, one turn of the fuel pump gear corresponds to 720 crankshaft degrees. The first cylinder’s pulse is several degrees narrower than the others in order to distinguish between cylinders. Figure 3.2 shows the shape of the triggering mask, and the resulting output wave for a cylinder firing order of 1-5-3-6-2-4.

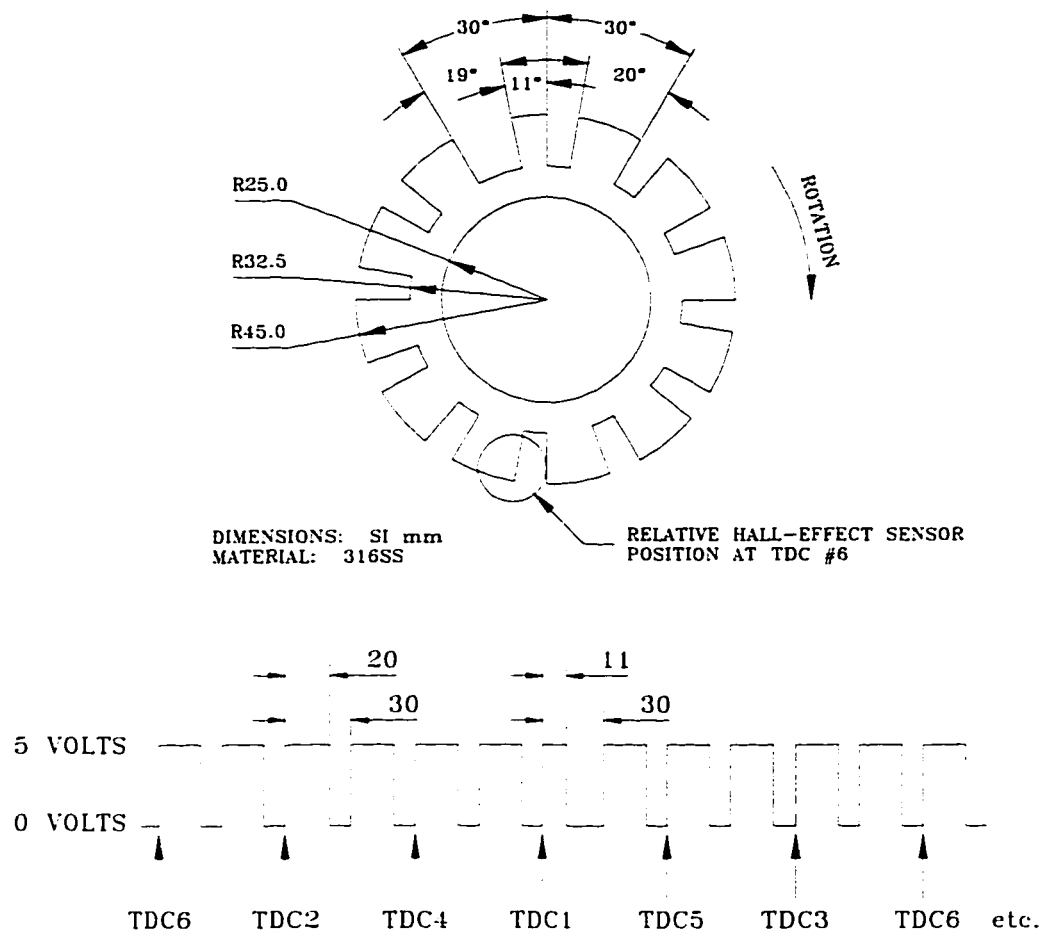


Figure 3.2 AFS Crankshaft Position Mask with Corresponding Output Wave

3.2 Test Cell Control Equipment

The dual fuel OM366LA was installed in an engine test cell to perform controlled knock experiments. To run the engine at various loads and speeds, the engine was directly coupled to a Mid-West Engineering eddy current dynamometer. Using this piece of equipment, torque can be applied to the engine by exposing a rotating iron rotor to an electrical field of varying intensity and orientation. A DyneSystems DYN-LOC IV digital dyno control unit uses electrical feedback to hold the engine at constant rotational speed. This particular dyno is rated for use up to 186 kW (250 hp) and 6000 rpm. Before

each batch of experiments, the dynamometer's load cell was calibrated using a system of known weights and a lever arm. The control unit monitors an inductive pickup in the dynamometer housing to determine engine speed.

With conventional diesel engines, desired torque is selected by moving the diesel pump rack. In this style of dual fuel engine, torque is selected electronically by a position sensor on the accelerator linkage. For experimental purposes, an dummy accelerator equipped with a TPS was connected to a DyneSystems DTC-1 digital throttle controller. This provided the engine operators with high-resolution control over commanded torque. Electrical power for the 24-volt ECM and actuator was provided by two deep-cycle 12-volt batteries connected in series, consistent with the 24-volt electrical systems typical of heavy-duty vehicles.

Engine coolant temperature was controlled by replacing the conventional engine radiator and thermostat with a shell-and-tube cold water heat exchanger. In addition, each exhaust port was equipped with a K-type (chromel-alumel alloy) thermocouple and the oil pan and intake manifold were outfitted with T-type (copper constantan alloy) thermocouples. To measure the air mass flow rate, all incoming air was drawn through two ASME long-radius nozzles in an otherwise-sealed air barrel. A Validyne™ transducer calibrated from 0.00 to 1.70 kPa measured the pressure difference across the nozzles. Using ASME standard equations, air mass flow rate was calculated and later corrected for humidity by using wet and dry bulb temperature records.

The diesel fuel for all tests was produced by Imperial Oil Inc. and conformed to the specification outlined in SAE J1349 (Jun90) [41]. Fuel was drawn from a 30 litre container on a GSE Scale Systems model 550 weigh scale with a 1 g resolution and a 5 kg range. A chilled water heat exchanger installed in the fuel return line from the pump gallery controlled fuel tank temperature. To calculate fuel flow rate, the rate of change of weigh scale reading was electronically recorded. A similar technique was used to

determine the flow rate of natural gas from a pressure vessel on a second identical weigh scale. Natural gas was drawn from the University of Alberta's service, with an average composition of 94% methane, 2% ethane, 3% nitrogen, and 1% carbon dioxide by volume [10]. The gas was compressed into eight 60-litre steel storage cylinders by a FuelMaker Model 3 Vehicle Refueling Appliance, then delivered to the weigh scale through stainless steel tubing.

During the initial dual fuel development, several exhaust gas analyzers were used to help fine-tune the ECM's fuel control maps. A vacuum pump pulled exhaust gases through a series of particulate filters and water vapour traps. The sample gas was then distributed to a number of emissions analyzers in the engine control room. Two Beckman model 864 infrared analyzers measured carbon monoxide and carbon dioxide levels. A Beckman model 955 chemiluminescent analyzer measured the concentration of oxides of nitrogen (NO_x). A Taylor Servomex model OA-137 analyzer detected the concentration of oxygen in the exhaust. Hydrocarbon emissions were measured in two different ways; a Beckman GC 72-5 determined total hydrocarbon (THC) content by a flame ionization technique, and an MTI P200 gas chromatograph with a thermal conductivity detector measured methane (CH_4) directly. The difference between THC and CH_4 readings (both on a carbon-1 basis) was defined as the non-methane hydrocarbon (NMHC) content. Each analyzer was calibrated daily using a series of bottled calibration gases.

Outputs of all the above equipment were simultaneously displayed and stored using a 32-channel data acquisition system. Two 16-channel Keithley Metrabyte EXP-16 expansion boards were multiplexed to a DAS-16 analogue-to-digital (A/D) convertor. Once per second, an IBM-compatible personal computer digitally acquired and stored each channel's level. Additionally, the ECM communicated with a second PC through a serial port connection. This enabled the operators to monitor all of the engine's sensors from one control station and store this data for future reference.

3.3 Knock Detection and Analysis Equipment

All of the equipment listed in the previous two sections serves one important purpose - it allows the researcher to induce knock in a typical dual fuel engine with reasonable consistency and controllability. In this way, the phenomenon of end-gas autoignition can be systematically explored. This study focuses on two different instruments for knock detection.

The primary method for detecting knock in the laboratory is through the use of an in-cylinder pressure transducer. Directly measuring combustion pressure gives a great deal of information about the nature of both normal and abnormal combustion processes. For this project, a spare OM366LA engine head was specially modified to allow access to the combustion chamber of cylinder number six. A 9.53 mm (3/8") diameter hole was drilled through the outer edge of the head and into the hardened ceiling of the combustion chamber. To avoid interference with valve ports and head bolts, x-ray images of the head were carefully studied. The optimum transducer hole location depicted in Figure 3.3 avoids weakening the head bolt bosses and stays well clear of the valve seats. A stainless steel sleeve (see Figure 3.4) spanned the gap across the water jacket and connected the combustion-facing and outward-facing holes. A Kistler 601B1 piezoelectric transducer was held inside the sleeve by the compressive force of a packing tube. The sleeve was designed to recess the transducer's pressure-sensing face 5 mm from the combustion chamber wall. The 601B1 is one of the smallest transducers available that can adequately handle the demands of combustion pressure measurement. Choosing a transducer with a tiny 5.55 mm diameter minimizes the size of the hole that must be drilled through the head, which reduces the amount of structural weakening. Routing the sleeve through the head's water jacket helps convect heat away from the sensor, protecting it from the extreme temperatures of combustion gases. The sleeve is sealed at the combustion end by 3/8"-NF24 threads treated with high-temperature (#272) Loctite™. A standard rubber O-ring at the opposite end of the tube prevented engine coolant leakage. Recessing the face of the transducer 5 mm from the combustion cavity prevents physical contact with

moving engine parts. The small gap also places the face close enough to the combustion chamber to prevent acoustical effects from the transmission space between the instrument and the chamber.

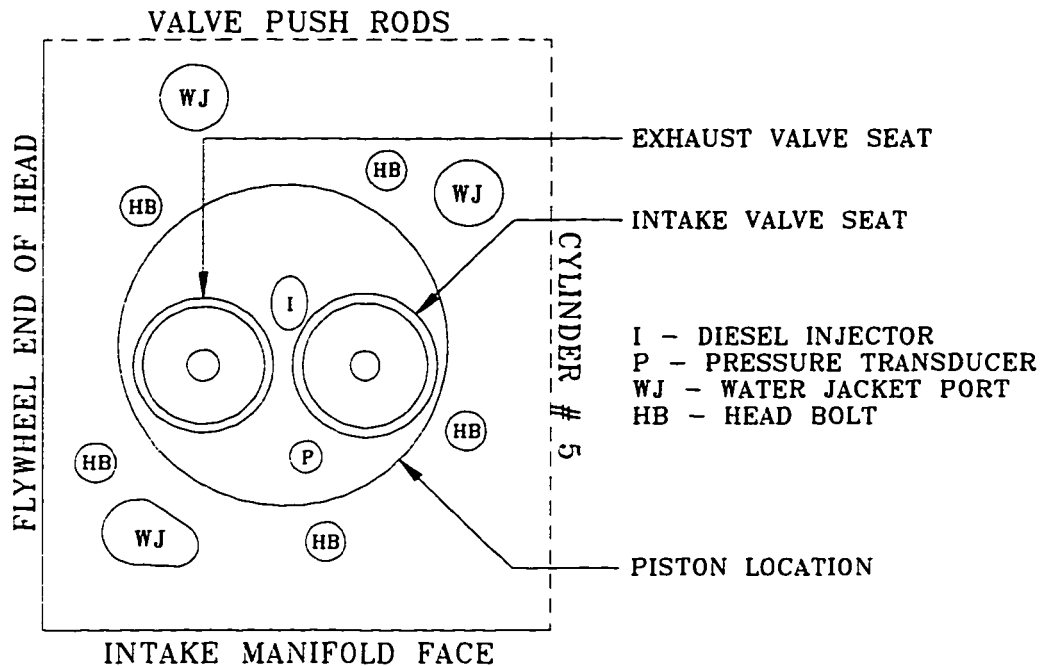
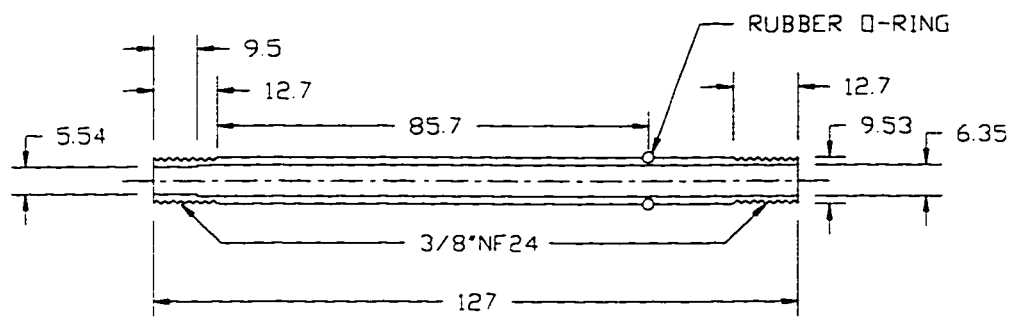


Figure 3.3 Pressure Transducer Location in Combustion Chamber Six

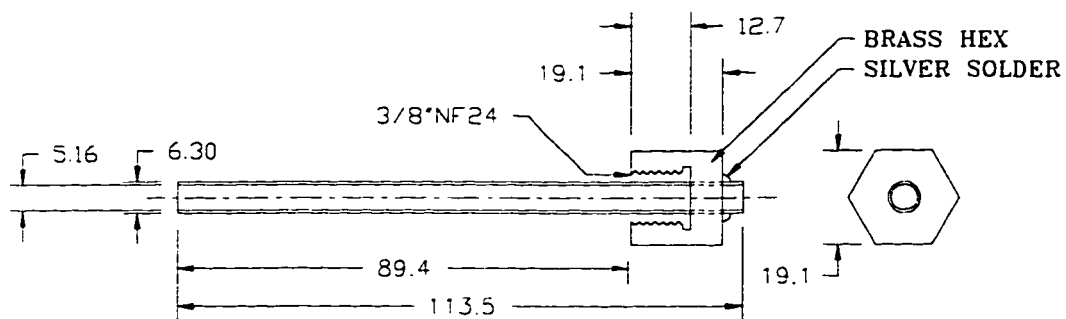
The Kistler 601B1 measures pressure by exploiting the piezoelectric effect discovered by the Curie brothers in the nineteenth century [42]. When certain crystals are loaded mechanically, their surfaces become electrically charged. By converting this charge to a voltage with a charge amplifier, voltages directly proportional to pressure can be read. Quartz crystals are particularly useful for this application, since they have high mechanical strength, good thermal stability, excellent linearity, and their output is not prone to hysteresis. In the 601B1, a diaphragm welded to the end of the transducer deflects when pressure is applied, compressing quartz crystal elements inside. The resulting piezoelectric charge is transmitted via a shielded micro-BNC cable to a

Sundstrand model 507 dual-mode differential amplifier. The amplifier, transducer, and cable combination was calibrated with a Budenberg dead-weight pressure tester from 0 to 13,790 kPa (2000 psi). The calibration procedure is outlined in Appendix A.

MATERIAL: 316SS (except where noted)
 DIMENSION: SI mm (except where noted)



TRANSDUCER SLEEVE



PACKING TUBE

Figure 3.4 Transducer Sleeve Assembly

The piezoelectric transducer's output tends to drift rather quickly when exposed to the extreme heat of combustion gases. As a result, the pressure signal must be correlated (or "pegged") to a reference point in the engine cycle to determine true absolute pressure. In this study, the transducer signal was pegged to manifold absolute pressure at 180 crankshaft degrees before TDC (compression) for each combustion event. This is in accordance with the recommendations of Randolph [43] and Brunt and Pond [44].

At the same time, knock was sensed non-intrusively with a Brüel & Kjær type 4370 wide-band instrument-grade accelerometer. The 4370's undamped natural frequency is rated at 26 kHz, safely above the expected knock frequency, and its measured sensitivity deviated less than +1.5 dB up to 8000 Hz. This instrument also works on the piezoelectric principle. Bolted to the middle of the cylinder head, the accelerometer senses different levels of block vibration. Deflection of the flush-mounted sensor face mechanically loads the quartz crystal inside. A Brüel & Kjær model 2511 vibration amplifier was connected to the accelerometer by a micro-BNC cable and used in "acceleration" mode. Unfortunately, the laboratory was not equipped with the equipment necessary to properly calibrate this sensor at the high-frequency, high- g conditions of interest. As a result, all of the block vibration results presented in this thesis will be relative values proportional to g 's (hereafter designated as g^*) instead of true g -forces. Each test was performed with the same amplifier settings and accelerometer location for consistent results. The sensor was bolted to the lower edge of the cylinder head, between cylinders 3 and 4. This location was selected based on previous experience at the University of Alberta [45] and recommendations in the literature [37]. The accelerometer was easily accessible, protected from harsh environmental conditions, and was bolted securely to a mechanically stiff engine component in a location central to all cylinders.

Cylinder pressure, block acceleration, and engine crankshaft position were simultaneously recorded on magnetic tape, as portrayed in Figure 3.5. A Racal Store-4DS 4-channel reel-to-reel FM tape recorder converted incoming voltages to frequencies,

then wrote the data to 6 mm (¼") tape. The linear tape speed was set to 0.762 m/s (30 inches per second) for recording, which provided each channel with an available bandwidth of 0-20 kHz. Crankshaft position and cylinder pressure were written to two separate channels through unipolar input cards, while the oscillating accelerometer signal was recorded in bipolar mode on a third channel. Upon playback, the Store-4DS reverted each recorded FM signal to analogue voltage, and all outputs were automatically adjusted to fit a unipolar 0-5 volt range. The advantage of recording voltages as frequencies is that tapes can be played back at a different velocity from the recording speed without a shift in voltage level. The data was digitized by playing the three recorded channels into the A/D convertor card of an IBM-compatible personal computer. Each analogue signal was captured with 16-bit digital resolution at a sampling frequency of 10 kHz per channel. However, by reducing the playback speed to only 0.1905 m/s (7.5 ips) or one-quarter of the recording speed, the effective sampling frequency quadrupled to 40 kHz per channel. This high sampling frequency prevents the possibility of aliasing effects corrupting the data and provides excellent data resolution for future studies. Digitized data points are first stored in binary format on computer hard disk, then burned to recordable compact discs for subsequent analysis.

Finally, a variety of computer programs have been written by the author and his colleagues to analyze the collected data. Routines programmed in QuickBASIC for DOS read data from hard disk or CD, then study the accelerometer and transducer signals with respect to engine position. Techniques such as digital bandpass filtering, data windowing, and signal analysis will be discussed thoroughly in the next chapter.

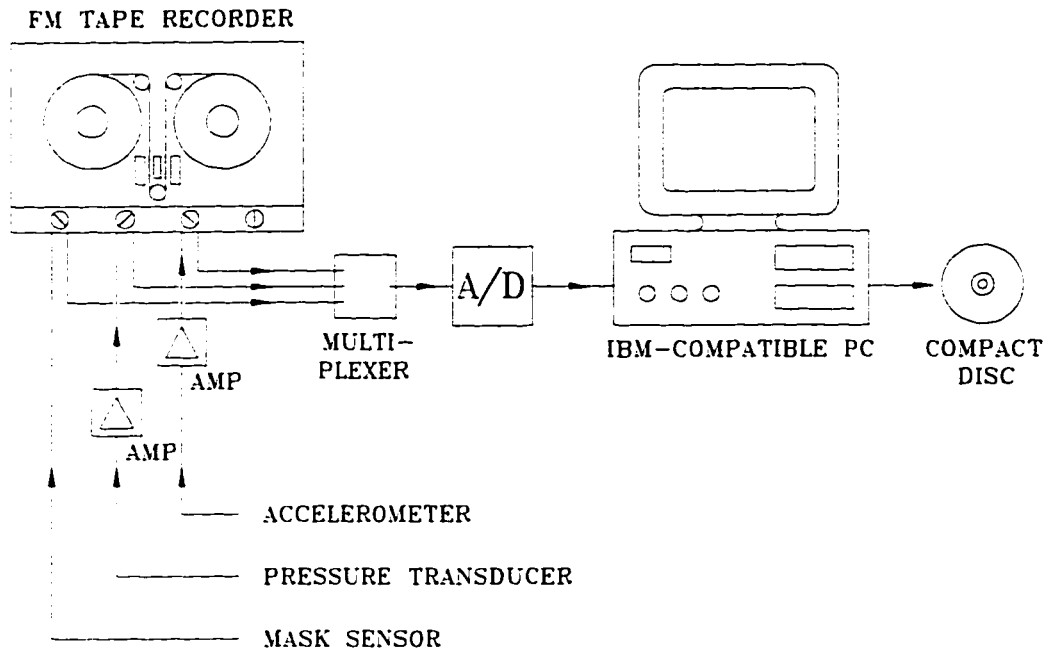


Figure 3.5 Schematic of Recording and Digitizing Equipment

**EXPERIMENTAL
METHODOLOGY**

4.1 Production and Recording of Knock Signals

To investigate and understand knock, the phenomenon must first be produced and recorded in a consistent and reliable manner. There are three major interrelated variables that can be manipulated to promote the onset of knock in a dual fuel engine. Knock occurs when the concentration of fuel in the end-gas regions of combustion becomes excessively high. Secondly, end gases will begin to knock as the result of excessive heating from flame front compression and/or high air intake temperature. Finally, the reactivity of the fuel/air mixture affects the tendency to knock. In this research project, a dual fuel engine was connected to a dynamometer and monitoring equipment to give the operators full control over engine torque and speed. Then, the engine was forced to knock with various intensity by manipulating one of the aforementioned variables - fuel/air equivalence ratio. The outputs of intrusive and non-intrusive knock sensors were subsequently recorded with the equipment outlined in Section 3.3.

This project was initiated by Alternative Fuel Systems Inc. (the manufacturer of the dual fuel conversion kit) in response to concerns about gas quality. It is not uncommon for utilities to temporarily replace some of the methane content of natural gas with propane-air mixtures. This can be accommodated by external combustion devices, since the propane and air quantities are controlled to maintain a constant heating value of the fuel gas. However, since propane ignites at a lower temperature than methane, this also

increases the tendency for end gases in dual fuel engines to autoignite [8]. This effect could be duplicated in the laboratory by the combustion of several different “grades” of natural gas. Unfortunately, this requires mixing, storing, and analyzing many different gas samples with a chromatograph to conduct a simple series of knock tests. Instead, two simpler approaches were adopted.

The effect of propane-enriched end-gas was duplicated by delivering an artificially high amount of natural gas, which richened the overall gas/air ratio. This was achieved in the laboratory by increasing the CNG supply pressure to the sixth cylinder’s gas injector. Each injector is a high-speed valve, and the amount of fuel delivered in each injection event depends on how long the valve is open and the pressure difference across the valve. Opening the valve for the same amount of time with a higher gas supply pressure resulted in more fuel energy being injected per event. Richening the air/fuel ratio of the end-gas increased its sensitivity to temperature, which raised the tendency to knock. The normally-regulated gas supply pressure of 1000 kPa was gradually raised to 1600 kPa to induce knock varying in intensity from very light to extreme.

Over the last decade, AFS has observed with several engine conversion projects that dual fuel knock sensitivity also depends on the fuel replacement ratio at high torque. With the AFS system, desired torque is determined from a throttle position sensor input. The control computer accesses an engine fuel map to determine the amount of diesel fuel energy required to produce this level of torque for the current speed. Finally, the computer consults a pilot map to determine the fraction of fuel energy to be injected as diesel, then makes up the rest of the energy budget with natural gas. If the pilot quantity is reduced, the computer compensates by increasing gas delivery to achieve the same amount of torque. Therefore, as the fuel replacement fraction increases, the end-gas becomes richer. Eventually, the engine reaches the point where either the pilot is too small to ignite the gas-air mixture (resulting in a misfire), or the end gas becomes rich enough to autoignite. With the OM366LA test engine, knock was successfully induced

by gradually reducing the pilot quantity from 34% (40 milligrams per injection) to 17% (20 mg/inj.) of the total input energy budget. This was achieved by modifying parameters in the ECM's pilot quantity map while using standard (1000 kPa) CNG supply pressure for all gas valves. Like the gaseous overfuelling of cylinder six discussed previously, pilot reduction caused knock of intensities ranging from very light to severe.

The results reported in the following chapter of this document focus on the digital recordings of two experiments. In the first experiment, knock was induced by the gas-overfuelling technique at two engine speeds - 1500 rpm and 2100 rpm. These speeds were chosen because they reflect the OM366LA's maximum-torque point and a common high-speed operating point, respectively. While increasing the CNG supply pressure from 1000 kPa to 1600 kPa in 100 kPa increments, seven different 20-second recordings were made at each speed. In the second experiment, the pilot quantity was gradually reduced until severe knock was observed, again at 1500 rpm and 2100 rpm. The volume of pilot injection was reduced from 40 mg/injection to 20 mg/injection in 5-milligram steps, providing five knock recordings at each speed.

4.2 Definition of Operator-Observed Standard Knock Intensity (SKI) Scale

Humans are equipped with an excellent “on-board” knock detection system [17]. The ear has a remarkable ability to filter out low-frequency engine noise and focus on higher-frequency “pinging”. An experienced human can even interpret subtle changes in “ping” loudness as variations in knock intensity. Additionally, researchers in a controlled lab environment often observe a change in the nature of floor and wall vibration when a nearby heavy-duty engine begins to knock. As a result, one of the best standards for knock intensity is derived simply from qualitative observations.

During the course of knock experiments conducted with the OM366LA, operator-observed knock intensity levels varied from “no audible knock” through “light” to

“extreme”, with several intensities in between. Unlike temperature or mass, knock intensity cannot be directly measured using electronic instruments. This vaguely-defined concept must be implicitly inferred by observing the output of a transducer or accelerometer and comparing the signal to some accepted standard [17]. Therefore, to properly determine the best sensory detection technique, one must first define a quasi-quantitative scale of operator-observed knock intensity. In this project, a Standard Knock Intensity (SKI) scale was chosen by the author to help assign a numerical value to the perceived audible level of knock intensity. The scale was defined as in Table 4.1. At each test point, the author evaluated the relative loudness of audible “pinging” and the amount of floor vibration, and then selected an appropriate SKI value from the table.

Table 4.1 Standard Knock Index (SKI)

Perceived Level of Knock	SKI
normal combustion (no audible knock)	1
light knock (faint pinging)	2
moderate knock (clear pinging)	3
heavy knock (intense pinging)	4
extreme knock (intense pinging, excessive vibration)	5

4.3 In-Cylinder Analysis Techniques

4.3.1 Initial Pressure Trace Observations

In controlled environments, it is clear that humans have a well developed ability to detect knock. An urban bus driver, however, has to contend with a much greater amount of ambient noise. Road noise, traffic noise, and even passenger noise make it difficult for a driver to hear knock from the other end of the bus. Engine mounts are designed to

dampen the transmission of vibration, so it is virtually impossible to feel the subtle change in engine roughness through the floorboards and seats. To make sure that knock does not go unchecked, some sort of automatic system is necessary. As described in Chapter 2, the “pinging” sounds that are observed during knock result from shock waves racing across one or more combustion chambers. The most accurate method of monitoring this phenomenon electronically is through the use of in-cylinder pressure transducers.

In a dual fuel engine, the normal combustion process involves a diesel pilot injection shortly before top-dead-centre (TDC) for each cylinder. Each squirt of diesel fuel rapidly vapourizes and ignites in the hot compressed gas-air mixture. The diesel flame ignites the gas-air mixture, and the combustion of natural gas generates most of the cycle’s energy release. Figure 4.1 compares the pressure traces of two dual fuel combustion events at 2100 rpm. The pilot quantity was injected at 13 degrees before TDC in each case. The non-knocking trace is reminiscent of a spark-ignition engine. During normal combustion, the diesel injection autoignited at approximately four degrees ATDC, followed by a steady, controlled burn. When the gas/air mixture became too rich, the end-gas ahead of the flame front spontaneously ignited and burned violently. The shock wave resulting from this explosion raced across the cylinder bore, accompanied by high-frequency pressure fluctuations. In Figure 4.1, these fluctuations appear as “ringing” on the curve’s downward slope after maximum pressure (about 16° ATDC). While peak pressure alone is a reasonably good indicator of the occurrence of knock, isolating and investigating the ringing pressures gives much more information about the frequency and intensity of knock. Since it is the peak pressure that drives the end-gas into its unstable condition, this report assumes that knock begins at P_{\max} and continues for an undetermined number of crankshaft degrees afterward.

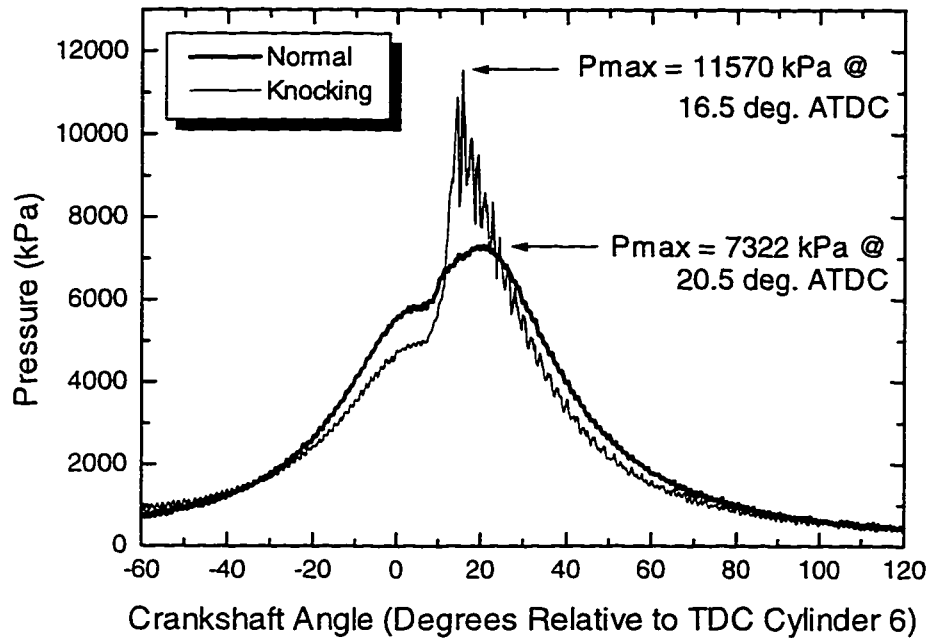


Figure 4.1 Comparison of Pressure Traces at 2100 rpm

4.3.2 Bandpass Filtering

The ringing component of a knocking pressure trace can be extracted by filtering the data. The gross shape of the curve (the transition from manifold pressure to peak pressure and back) is removed by attenuating the low-frequency content of the signal. It has been shown many times in the literature that knock frequencies for vehicular internal combustion engines range from 5 to 10 kHz [17]. To prevent the fundamental knock frequency's higher harmonics from "folding back", the data should also be filtered of high-frequency content. "Bandpass" filters are useful for simultaneously attenuating both high and low frequency information in pressure signals.

In this project, data analysis was performed digitally with computer programs. One of the routines incorporated into these programs bandpass filtered the knock recordings. A QuickBASIC subroutine representing an analogue Butterworth-type filter [46] attenuated

the pressure and accelerometer signals above and below a selected pass band. When this routine is applied to the traces of Figure 4.1 using a typical 7 ± 1 kHz pass band, the curves of Figure 4.2 result.

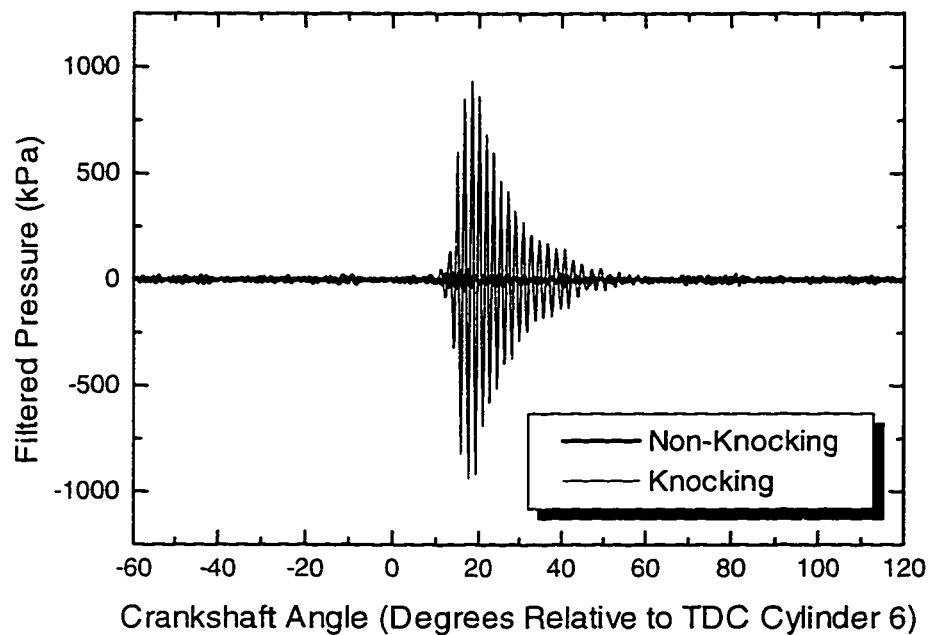


Figure 4.2 Comparison of Filtered Pressure Traces at 2100 rpm

All that remains after filtering (in this case) are the ringing pressures of the downward slope. The method for choosing the representative 7 kHz bandpass centre used in Figure 4.2 will be discussed in Section 4.3.4.

Butterworth filters exhibit the characteristic of being maximally flat, i.e. they minimize the distortion of the original signal inside the pass band at the expense of less effective attenuation outside the band [47]. They are ideal for knock pressure filtering since they are very good at removing low-frequency combustion noises and high-frequency harmonics without disturbing the signal in the knock frequency range. The particular

subroutine used in this research project was designed for a maximum distortion of 3 dB at the band pass limits with a minimum of 18 dB attenuation 5% of the sampling frequency outside of the band

4.3.3 High-Frequency Pressure Statistics

Once the knock component of pressure has been isolated from the rest of the signal, several different statistics can be calculated. The most obvious characteristic of the traces in Figure 4.2 is that filtered knocking and non-knocking signals have greatly different peak fluctuating pressure values. Combustion experts such as Heywood [17] and Benson *et al* [48] have noted that the maximum amplitude of pressure oscillation is a good indicator of knock severity.

Since the ringing phenomenon continues for several dozen degrees after P_{\max} , it is also possible to determine the root-mean-square (RMS) value of the amplitude population. The formula for calculating the RMS of a population of data [49] appears in Equation 4.1. This equation is appropriate for analyzing sets of more than 20 data points.

$$\sigma = \sqrt{\frac{\sum_{i=1}^N (x_i - \mu)^2}{N}} \quad (4.1)$$

where σ = population standard deviation (RMS)
 x_i = amplitude at each digitized data point, i
 μ = population mean
 N = total number of data points in the population

Calculating the RMS deviation of an oscillating pressure signal provides a measure of the pressure variability about the mean value. In practice, the RMS increases as a cylinder rings with greater fluctuating pressures, which makes it another good indicator of knock intensity.

Finally, spectral analysis of the filtered pressure is indispensable for investigating the fundamental frequency of oscillation. In this study, a routine was written in QuickBASIC which performed simple Fourier transforms (FT) on selected data sets. A Discrete Fourier transform (DFT) similar to those suggested by Shiavi [50] and Fyfe [51] converts a pressure array in the time domain into an amplitude array in the frequency domain. Equation 4.2 shows the applicable complex transform for discrete time and frequency records, while Equation 4.3 simplifies the DFT equation, extracting the real components of the transform.

$$X_{DFT}(f_m) = \frac{1}{N} \sum_{n=0}^{N-1} x(t_n) \exp\left(\frac{-j2\pi mn}{N}\right) \quad (4.2)$$

$$X_{DFT,real}(f_m) = \frac{1}{N} \sum_{n=0}^{N-1} x(t_n) \cos\left(\frac{2\pi}{N} mn\right) \quad (4.3)$$

where $x(t)$ = pressure signal in time domain
 $X(f)$ = transformed pressure amplitude in frequency domain
 N = number of data points in pressure array
 m, n = indices of notation (in frequency and time domains, respectively)

When the spectral density of a pressure sample is concentrated at one particular frequency, this appears as a spike in the transform plot. When the filtered pressure traces of Figure 4.2 were analyzed with this FT routine, the result is as shown in Figure 4.3. The fact that the knocking cycle contains a burst of energy that is not present in the non-knocking transform suggests that the knock frequency is approximately 7300 Hz.

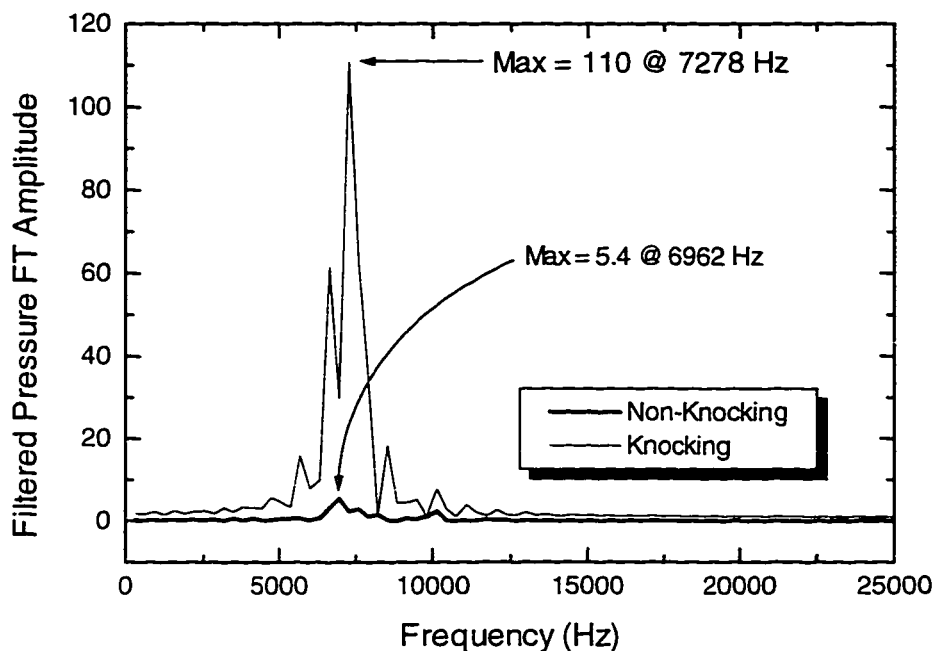


Figure 4.3 Comparison of Fourier-transformed Pressure Traces at 2100 rpm

4.3.4 Pressure Data Windows

As mentioned in Section 4.3.1, end-gas autoignition is triggered near the time of maximum chamber pressure, and pressure fluctuations reverberate for a number of degrees after the initial explosion. The first step in calculating the statistics mentioned previously is to specify a discrete time “window” of data. With filtered pressure records, the beginning of this window can be set to the time corresponding to maximum pressure. Choosing a specific length of time after this start point is more difficult, since the point at which the ringing stops tends to be less well-defined. In this study, the pressure data window always begins at P_{\max} , and the length of the window varies from 10 to 60 crankshaft degrees, as in Figure 4.4.

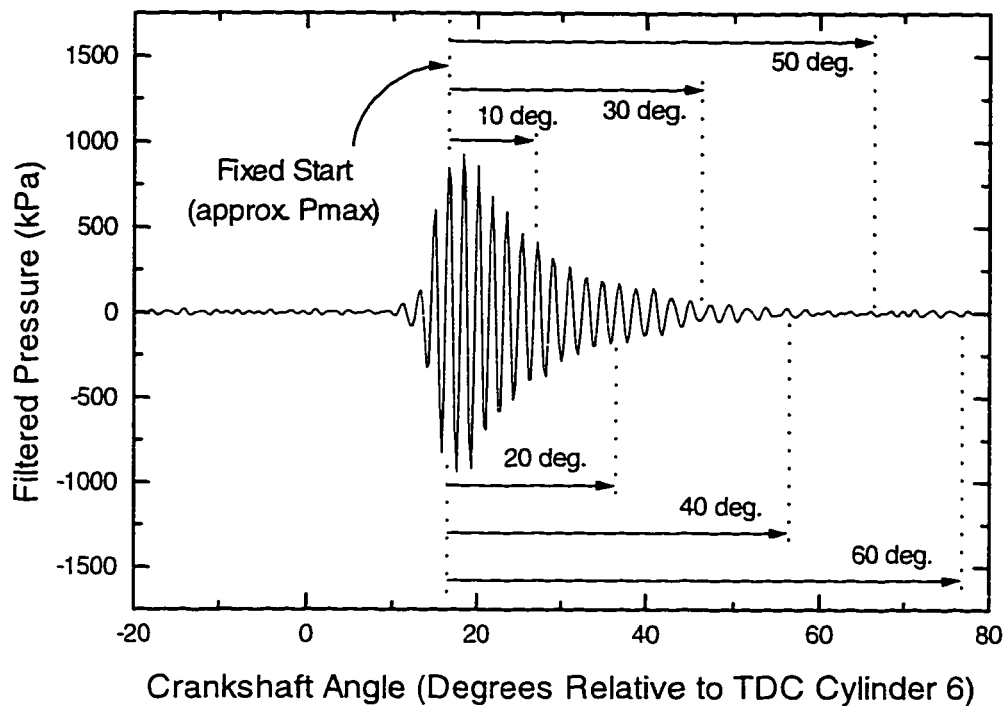


Figure 4.4 Various Pressure Data Windows for Knock at 2100 rpm

To investigate the effect of pressure data window length on knock detection sensitivity, pressure signals with varying knock levels were analyzed. Seven different knock intensities were generated by overfueling cylinder six with natural gas, and five different intensities were achieved with pilot reduction. In Chapter 5, pressure statistics have been calculated using various length windows for each severity level, and then correlated to the SKI index for those conditions. This study determined which statistic is the most reliable, and suggested the most appropriate window length.

To illustrate the method of testing knock statistics, consider the evaluation of filtered pressure RMS as a knock indicator. For a set of experiments at 1500 rpm, the gas supply pressure was increased from 1000 kPa (normal) to 1600 kPa (severe knock) in 100 kPa increments. Using a window from P_{max} to 40 crankshaft degrees after P_{max} , the filtered

root-mean-square pressure for each combustion event can be calculated. Next, determining the mean value of pressure RMS for 100 consecutive cycles at each condition accommodates normal cycle-to-cycle statistical variations in knock intensity. Once the mean RMS values have been calculated for seven different knock severities, this array (X) can be correlated to the corresponding array of seven observed SKI values (Y) using a statistical analysis [49] similar to Equation 4.4.

$$\text{correlation} = C = \frac{S_{xy}}{\sqrt{S_{xx} \cdot S_{yy}}} \quad (4.4)$$

where S_{xx} , S_{yy} , and S_{xy} are sums of squares of the RMS and SKI arrays, as defined by:

$$S_{xx} = \sum (x - \bar{x})^2 = \sum x^2 - \frac{(\sum x)^2}{n} \quad (4.5a)$$

$$S_{yy} = \sum (y - \bar{y})^2 = \sum y^2 - \frac{(\sum y)^2}{n} \quad (4.5b)$$

$$S_{xy} = \sum (x - \bar{x})(y - \bar{y}) = \sum xy - \frac{(\sum x)(\sum y)}{n} \quad (4.5c)$$

If the correlation coefficient, C, between (X) and (Y) is high (i.e. near unity), this provides statistical evidence that RMS pressure is a good predictor of knock intensity (as indicated by SKI). In this project, correlations were calculated with a Microsoft Excel computerized spreadsheet employing this statistical principle.

The correlation technique has also been used to determine the fundamental knock frequency and, consequently, the most appropriate digital filter limits. Bandpass filters are commonly defined by specifying a centre frequency and a symmetrical bandwidth around that point. For instance, a series of knock control chips currently produced by Bosch Electronics feature on-board bandpass filtering, with a user-selectable centre frequency surrounded by a ± 1 kHz fixed pass band [36]. Since AFS is evaluating this

type of chip for use with their production knock kit, the filter used in this research project was chosen to conform to this filter format. Analysis of knocking pressure traces with different filter settings was the first step in determining the OM366LA's knock frequency. Peak, RMS, and Fourier transform results have been calculated for each filter and compared. The centre frequency that led to maximum transducer sensitivity was adopted as the optimum setting and used for all subsequent trials.

4.4 Non-Intrusive Analysis Techniques

4.4.1 Accelerometer Statistics

While pressure transducers detect knock very well, they are not economically feasible as a production-volume sensor. Installation of a transducer in every cylinder of every converted dual fuel engine is simply too cumbersome and expensive, and the required modifications can significantly weaken the engine. For spark-ignition engines, designers have successfully used block vibration to measure knock for several years. The goal of this research was to determine if a block-mounted accelerometer is able to adequately detect knock-induced vibrations in the stiffer, heavier block of a compression-ignition engine.

When pressure waves from end-gas autoignition collide with combustion cavity walls, they transfer momentum to other parts of the engine. Since some of this energy causes the block to vibrate, knock can be indirectly detected by measuring the acceleration of certain engine surfaces. Knocking combustion appears in the accelerometer signal as oscillations of a higher magnitude than the equivalent normal combustion level of vibration, as in Figure 4.5.

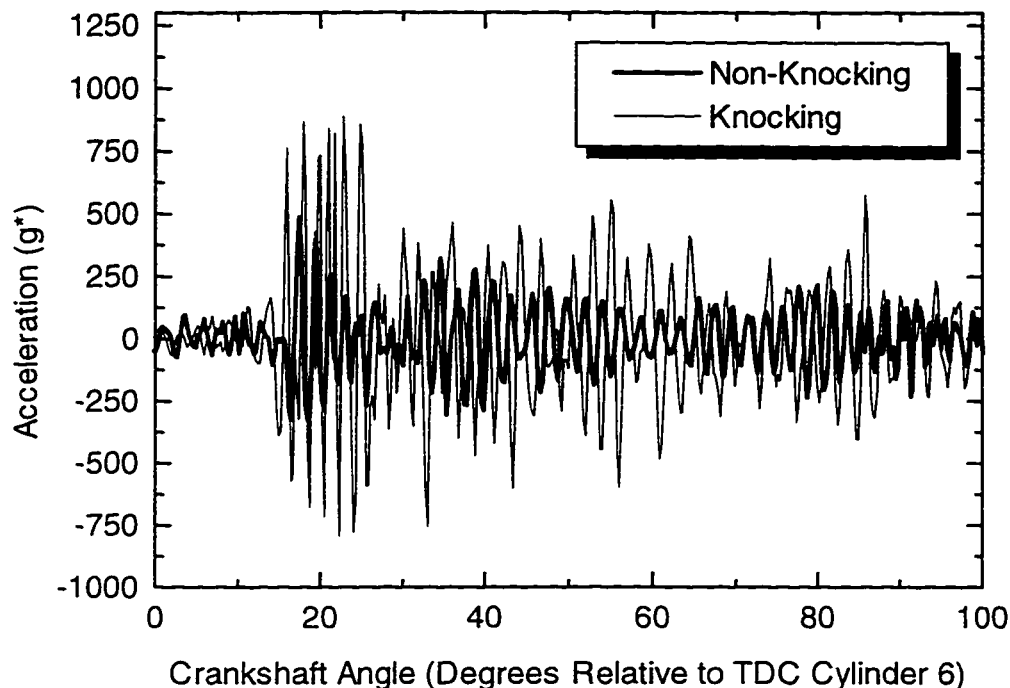


Figure 4.5 Comparison of Accelerometer Signals at 2100 rpm

The same bandpass filtering and windowing techniques discussed in Section 4.3.2 can also be applied to the accelerometer signal to increase the signal-to-noise ratio. This helps to attenuate block vibration signals caused by ordinary engine events. Figure 4.6 illustrates the amplitude difference between filtered accelerometer signals of different knock severity. Additionally, the Fourier transform routines of Section 4.3.3 have been used to extract information from the filtered acceleration signal regarding the most prominent frequencies of vibration, as in Figure 4.7. In this way, statistics such as filtered maximum amplitude, filtered RMS deviation, maximum FT amplitude, and most prominent FT frequency were determined for the vibration sensor. These statistics were correlated to the SKI values and the accepted pressure-derived standard to establish the most reliable accelerometer-based knock detection technique.

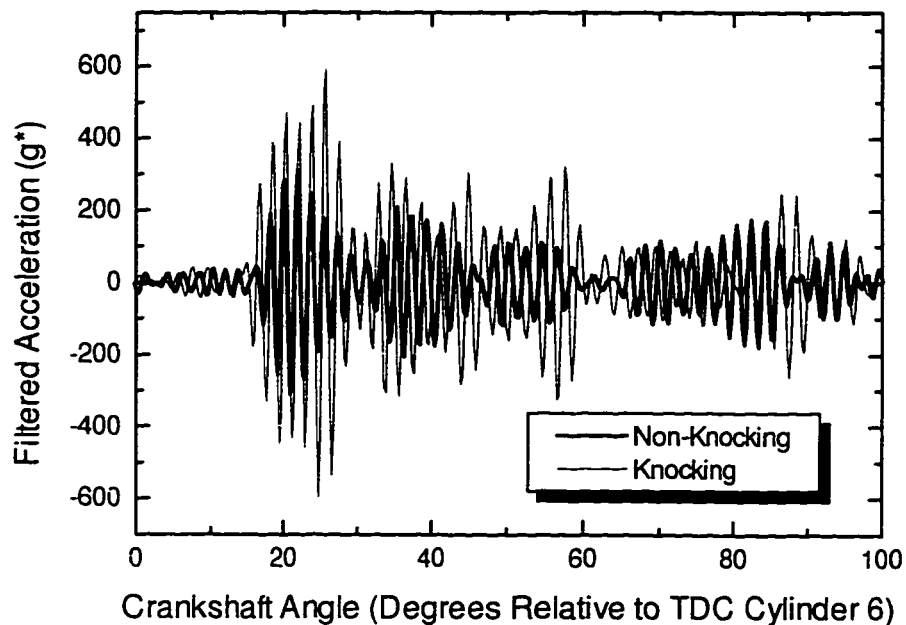


Figure 4.6 Comparison of Filtered Accelerometer Signals at 2100 rpm

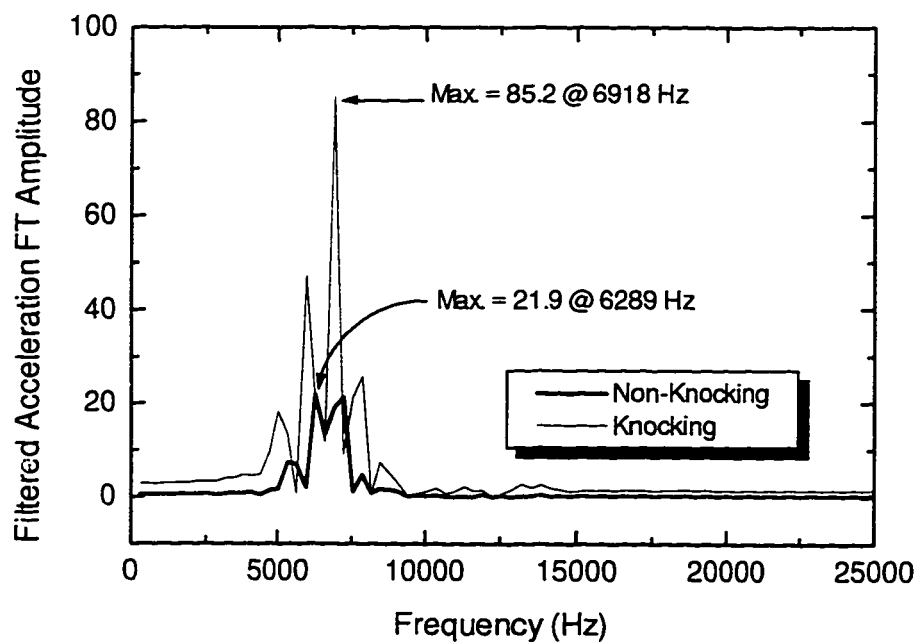


Figure 4.7 Comparison of Fourier-transformed Accelerometer Signals at 2100 rpm

4.4.2 Accelerometer Data Windows

Because of the high level of background noise in the accelerometer signal, it is important to choose an appropriate data window for statistical analysis. In Section 4.3.4, a rationalization was provided for synchronizing the beginning of the pressure window to the point of maximum pressure. Since the pressure fluctuations of the knock phenomenon affect the pressure transducer directly, the signal is expected to respond instantaneously. The accelerometer, on the other hand, must wait for the pressure wave energy to be passed to the cylinder walls, then propagated through the block to the vibration sensor. The engine and sensor have mass, so there is a certain amount of inertia to overcome before the piezoelectric crystal will start to freely vibrate. Therefore, it was considered wise to investigate the optimum start point of the accelerometer data window rather than assign one automatically.

This was accomplished by shifting a constant-length window through a variety of start points, calculating several acceleration statistics in each window. The start point at which the statistics correlate best with the SKI and the pressure standard was considered the optimum. Figure 4.8 shows a typical 40-crankshaft-degree window where the start point has been shifted from TDC to 25 degrees ATDC to illustrate this concept. After the best start time was determined, the window length was varied as in the pressure transducer analysis (see Figure 4.4). This was used to confirm that the 40 degree window suggested by the filtered pressure traces was also appropriate for the accelerometer.

The methodology outlined in this chapter was used to determine how well pressure transducers and accelerometers correlate with operator-observed knock intensity. The following chapter shows how this information has made it possible to recommend a suitable knock detection scheme for dual fuel engines.

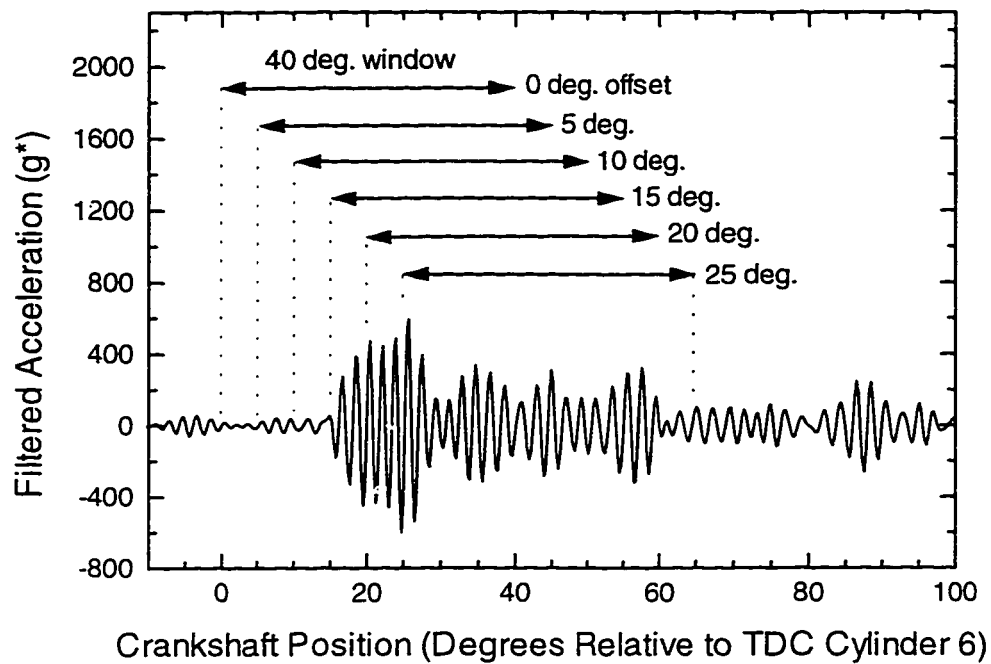


Figure 4.8 Shifting Accelerometer Window To Determine Optimum Start Point

CHAPTER FIVE

RESULTS AND ANALYSIS

5.1 Introduction

Two different experiments were conducted to determine how well intrusive and non-intrusive sensors could detect the intensity of engine knock. In the first experiment, the fuel/air ratio was richened by overfuelling one cylinder with natural gas. The CNG delivery pressure to the sixth cylinder's gas valve was increased from 1000 kPa to 1600 kPa in 100 kPa increments. Each pressure increase caused a proportional rise in gas flow rate and, consequently, an increase in end-gas sensitivity to knock. This "gaseous overfuelling" experiment resulted in a range of operator-perceived knock intensities from normal operation (no knock) to severe knock. The overfuelling investigation was conducted at 1500 rpm and repeated at 2100 rpm to determine the effects (if any) of engine speed on the tendency to knock.

In the second experiment, the end-gas regions of each cylinder were richened by reducing the volume of the diesel fuel "pilot" spray while increasing the contribution of CNG to the engine's overall fuel energy budget. The pilot quantity was reduced from a conservative (safe from knock) level of 40 mg/injection to 25 mg/injection in four 5-mg decrements. With each "pilot reduction", the engine control computer increased the quantity of natural gas being delivered to each cylinder to maintain constant torque. Once again, perceived knock intensity ranged from non-existent to severe in trials at 1500 rpm and 2100 rpm. Pressure and accelerometer records for cylinder number six were

compared to the operator-observed Standard Knock Intensity to determine the best in-cylinder and block-mounted knock measurement techniques. However, since the ECU could not control the fuel delivery to cylinders independently, cylinder six was no longer clearly distinguishable to human ears as the knocking cylinder. This may have reduced the effectiveness of the SKI scale as an indicator of knock intensity for that specific cylinder. For this reason and because of the pilot reduction experiment's lower resolution (five knock intensity steps compared to seven for the overfuelling experiment), the preliminary knock investigation focused mainly on the overfuelling results.

5.2 Operator-Observed Knock Intensity

The Standard Knock Intensity (SKI) index introduced in Chapter 4 was recorded for each test condition. The gaseous overfuelling experiment was conducted at 1500 rpm and again at 2100 rpm to reflect two of the engine's common full-torque operating points. The SKI results observed in the laboratory for this experiment are summarized in Figure 5.1, based on results tabulated in Appendix B, Table B.1.

As expected, the intensity of knock increased from $SKI = 1$ (no perceptible knock) at 1000 kPa gas pressure to $SKI = 4$ or 5 (heavy to extreme knocking) at 1600 kPa, with a nearly linear transition in between. It is apparent that the equivalence ratio of the premixed end-gas charge has a significant effect on the tendency to knock.

In the pilot reduction experiment, increasing the fuel richness of the end-gas regions again increased the tendency to knock. This experiment was also conducted at both 1500 rpm and 2100 rpm, and the corresponding SKI levels are listed in Table B.2, Appendix B. Graphically, SKI varies with pilot quantity as shown in Figure 5.2.

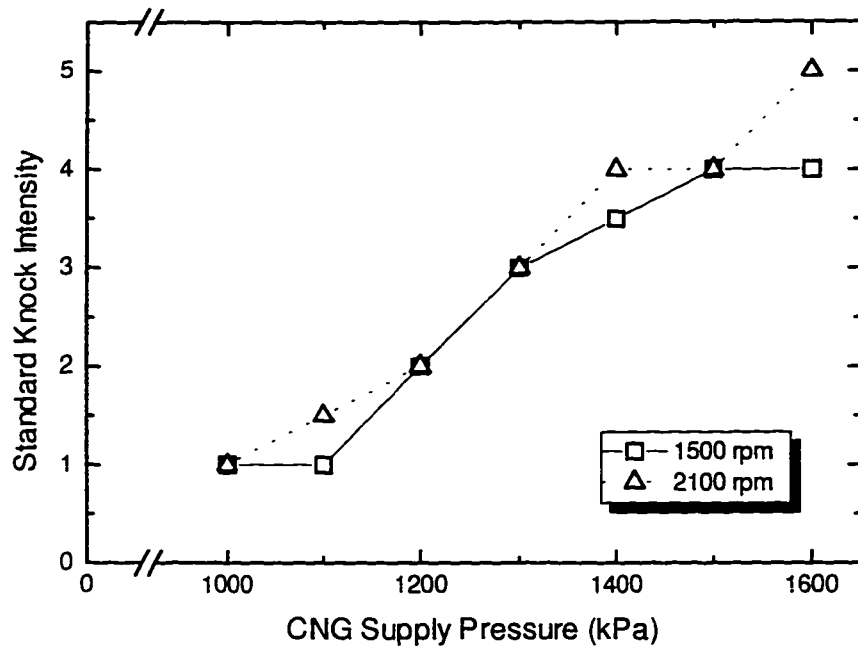


Figure 5.1 Effect of Gaseous Overfuelling on Perceived Knock Intensity

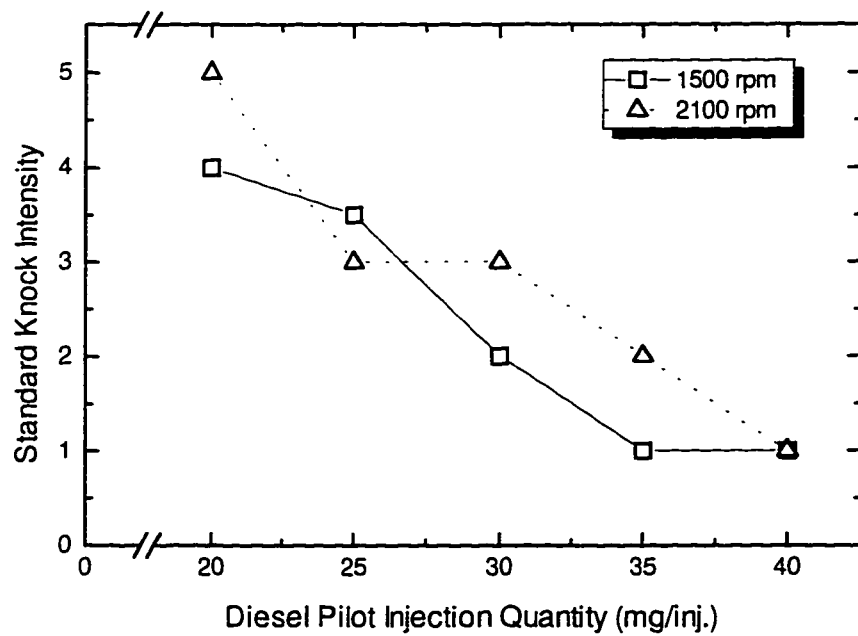


Figure 5.2 Effect of Pilot Reduction on Perceived Knock Intensity

The intensity of observed knock increased from $SKI = 1$ to $SKI = 4$ or 5 by decreasing the diesel pilot fraction. This is further proof that there is a practical limit to how fuel-rich the premixed gas/air mixture can become before knock develops into a significant problem. Alternative Fuel Systems has observed, through experience with a number of turbocharged dual fuel engines, that diesel replacement is usually limited by knock at full torque. Based on the above data, AFS's observation is applicable to the Mercedes OM366LA as well.

5.3 Gross Pressure Results

Two important statistics can be extracted from the gross (unfiltered) pressure signal. Knowing the peak pressure and the time at which it occurs helps to understand the processes of knocking and non-knocking dual fuel combustion. Table 5.1 contains peak pressure information for the gaseous overfuelling experiment and a diesel-only test at the same torque.

Table 5.1 indicates that in ordinary diesel-only operation, maximum pressure occurred at approximately 16 degrees after top-dead-centre for both engine speeds. At 1500 rpm, non-knocking dual fuel combustion occurred at a slightly higher peak pressure but at about the same time after TDC. At this point, the engine was well suited to dual fuel operation, since the increased pressure led to greater power and lower specific emissions. At 2100 rpm, however, the peak pressure was lower and later than the diesel baseline, suggesting that dual fuel combustion was not as thermally efficient at the higher speed.

The data contained in Table 5.1 also shows that as the engine knocked harder, the peak combustion pressure was higher and occurred earlier (sooner after TDC). As the gas supply pressure increased, the gas/air mixture inducted into the number six cylinder became richer. Since the same pilot quantity was retained for each pressure setting, the

cylinder was being increasingly overfuelled. As expected, both peak pressure and knock intensity rose as the end gas becomes richer.

Table 5.1 Gross Pressure Statistics, Gaseous Overfuelling and Diesel Baseline

Engine Speed (rpm)	Gas Supply Pressure (kPa)	SKI	P_{max} (kPa)	Location of P_{max} (deg.ATDC)
1500	none - diesel only	-	8387 ± 124	15.8 ± 1.1
1500	1000	1	8971 ± 238	16.7 ± 3.0
1500	1100	1	9437 ± 218	15.6 ± 0.6
1500	1200	2	10252 ± 161	13.7 ± 0.5
1500	1300	3	10894 ± 193	12.7 ± 0.5
1500	1400	3.5	10908 ± 162	12.7 ± 0.6
1500	1500	4	11244 ± 179	12.4 ± 0.7
1500	1600	4	11118 ± 193	12.7 ± 0.6
2100	none - diesel only	-	8112 ± 146	16.1 ± 1.6
2100	1000	1	7576 ± 158	19.7 ± 1.1
2100	1100	1.5	8868 ± 203	20.8 ± 0.5
2100	1200	2	9518 ± 230	19.3 ± 0.5
2100	1300	3	10238 ± 168	18.0 ± 0.4
2100	1400	4	10368 ± 199	16.8 ± 0.8
2100	1500	4	10012 ± 277	15.9 ± 0.7
2100	1600	5	10848 ± 550	14.0 ± 0.9

Finally, the value of peak combustion pressure can be used as a knock indicating statistic. Figure 5.3 shows the correlation between peak pressure and SKI, based on the data from Table 5.1. At 1500 rpm, the correlation coefficient, C (from Equation 4.4) between pressure and SKI is 0.9676, which is an excellent level of agreement. The correlation drops to 0.9048 at the higher speed. Pressure and SKI are still well-correlated, but the relationship is less linear at 2100 rpm.

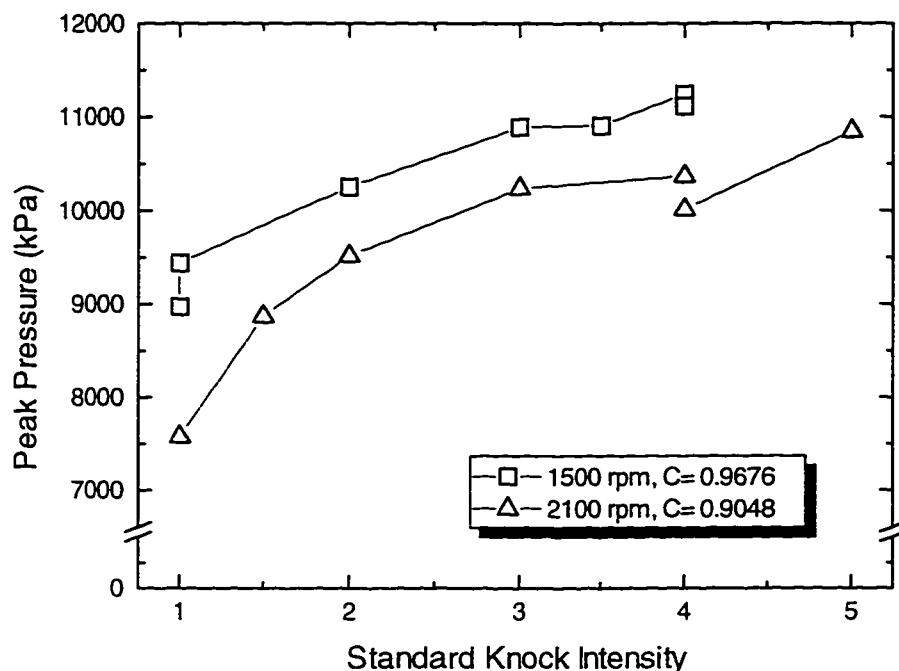


Figure 5.3 Variation of Peak Combustion Pressure with Observed Knock Intensity

5.4 Determination of Characteristic Knock Frequency

As noted in Section 4.2, knock manifests itself in the pressure trace as a high-frequency “ringing” after the maximum pressure point. An initial estimate of this frequency can be calculated by combining Equation 2.1 and the non-dimensional mode coefficients determined by Hickling *et al* from Section 2.1. For the OM366LA, this analysis (included in Appendix C) predicts the fundamental knocking frequency to be on the order of 6900 to 7300 Hz. However, knock frequency can be determined more accurately by the inspection of ringing pressure records.

A computerized bandpass filter was employed to separate the oscillating knock signal from the gross pressure trace. To specify the ideal centre frequency for the pass band, one heavily-knocking signal at each speed was analyzed using various filter parameters. The signals chosen for analysis were the 1600 kPa cases from the gaseous overfuelling

experiment. Each pressure trace was filtered with a ± 1 kHz bandwidth around centre frequencies ranging from 5 to 8 kHz. RMS and Fourier transform statistics were calculated for a 40-degree long filtered data window synchronized to maximum pressure. Since each signal was known to be knocking heavily, it was assumed that the maximum filtered RMS value coincided with the most appropriate centre frequency. The maximum amplitude and corresponding frequency from the Fourier transform analysis were also determined as other gauges of filter suitability. The values listed in Tables 5.2 and 5.3 are statistical means and first standard deviations calculated from 100 consecutive engine cycles at each filter setting. Figure 5.4 shows the variation of filtered pressure RMS with bandpass centre frequency at each speed.

Table 5.2 Pressure Trace Frequency Investigation (severe knock), 1500 rpm

Bandpass Centre Frequency (Hz)	RMS Pressure (kPa)	FT amplitude (kPa)	FT Frequency (Hz)
5000	22.0 \pm 5.1	5.39 \pm 1.85	5916 \pm 1382
5500	24.8 \pm 8.3	6.76 \pm 3.10	6980 \pm 785
6000	33.1 \pm 14.2	10.5 \pm 5.5	7173 \pm 400
6500	46.2 \pm 22.1	16.4 \pm 9.0	7313 \pm 209
7000	56.4 \pm 27.8	18.8 \pm 9.6	7358 \pm 223
7500	60.0 \pm 29.4	19.4 \pm 10.7	7372 \pm 216
8000	54.8 \pm 27.3	17.6 \pm 9.1	7475 \pm 219

Table 5.3 Pressure Trace Frequency Investigation (severe knock), 2100 rpm

Bandpass Centre Frequency (Hz)	RMS Pressure (kPa)	FT amplitude (kPa)	FT Frequency (Hz)
5000	76.6 \pm 15.0	21.0 \pm 6.0	6550 \pm 1043
5500	91.8 \pm 25.2	28.5 \pm 10.1	6886 \pm 657
6000	126 \pm 40	44.0 \pm 15.3	7038 \pm 317
6500	170 \pm 58	64.3 \pm 24.1	7126 \pm 183
7000	193 \pm 68	68.1 \pm 25.9	7196 \pm 189
7500	202 \pm 70	71.3 \pm 25.4	7284 \pm 216
8000	182 \pm 64	58.5 \pm 22.1	7423 \pm 214

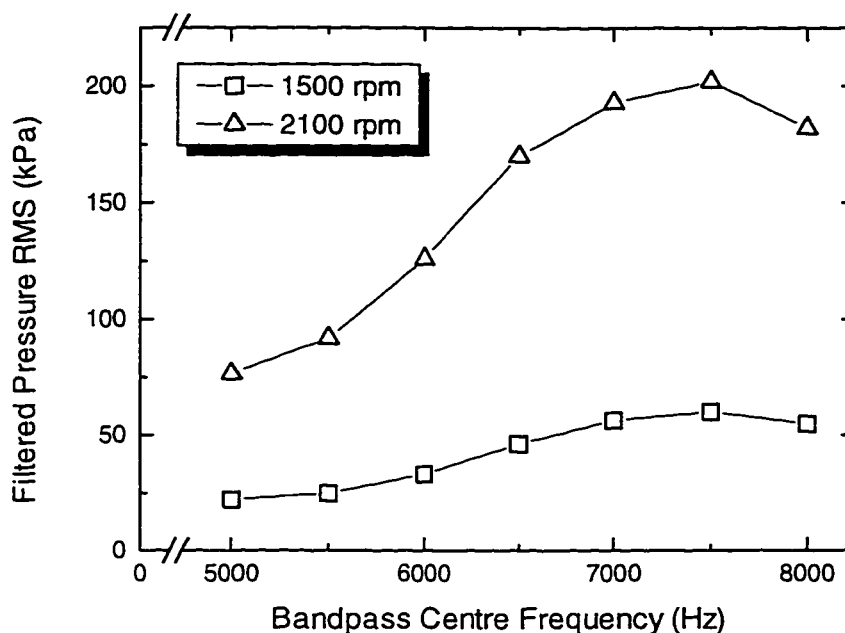


Figure 5.4 Variation of RMS Pressure With Bandpass Centre Frequency

The RMS pressure values for both speed cases suggest that the optimum centre frequency is between 7000 and 7500 Hz. While 7500 Hz is likely the best centre frequency for detecting severe knock, a 7000 Hz centre was chosen for two reasons. Recent work by Scholl *et al* [20] suggests that knock frequency is somewhat dependent on combustion temperature (and therefore directly proportional to knock severity). Thus, less severe levels of knock than those considered in Tables 5.2 and 5.3 would tend to occur at lower frequency (i.e. nearer to 7 kHz). Also, it is preferable that the results of this project be compatible with the eventual use of a commercial knock detection chip. The Bosch CC195 system under consideration performs on-board bandpass filtering, but it only allows the selection of integer values for centre frequency (i.e. 7 kHz and not 7.3 or 7.5 kHz). For these reasons, the fundamental knock frequency for the OM366LA engine has been approximated at 7000 Hz.

5.5 Investigation of In-Cylinder Pressure Statistics

Once a gross pressure trace has been bandpass filtered, all that remains is the cross-cylinder “ringing” pressures from knock. To capture the ringing data, a window was selected that started at the point of maximum combustion pressure. The length of this window (denoted in the figures as ‘w’) ranged from 10 to 60 crankshaft degrees. Three statistics were calculated from the data: maximum filtered pressure (FPmax), RMS filtered pressure (FPrms), and maximum Fourier transform amplitude (FPamp). These values were collected for each knock severity level and engine speed combination of the gaseous overfuelling experiment. A reasonably large population of 100 consecutive engine cycles were analyzed to determine mean values for each statistic. Next, each set of averaged statistics was correlated to the corresponding set of SKI indexes. The optimum statistic was chosen as the one that most reliably correlated with the SKI while maintaining a wide, usable dynamic range. Likewise, the optimum window length was the length that corresponded to the best pressure statistic.

The next two figures depict how well FPmax correlated with SKI at 1500 rpm and 2100 rpm. The figures in this section are all based on data included in tables in Appendix D. Figure 5.5 is derived from Table D.1, while Table D.2 provides the data for Figure 5.6. For short windows, the FPmax values at various natural gas supply pressures correlated poorly with the SKI index. Figure 5.5 shows that for a 10-degree data window, there was virtually no correlation between FPmax and SKI. For a 20-degree window, the correlation was 0.7702. This number seems quite high, but Figure 5.5 reveals that the range between low and high knock intensity is only a few kPa. The correlation is numerically correct, but the statistic is so insensitive with this window that it is practically unusable. Once the window is 30 or more crankshaft degrees long, however, the correlation ($C = 0.9899$) and FPmax range are both excellent, covering a relatively wide pressure range.

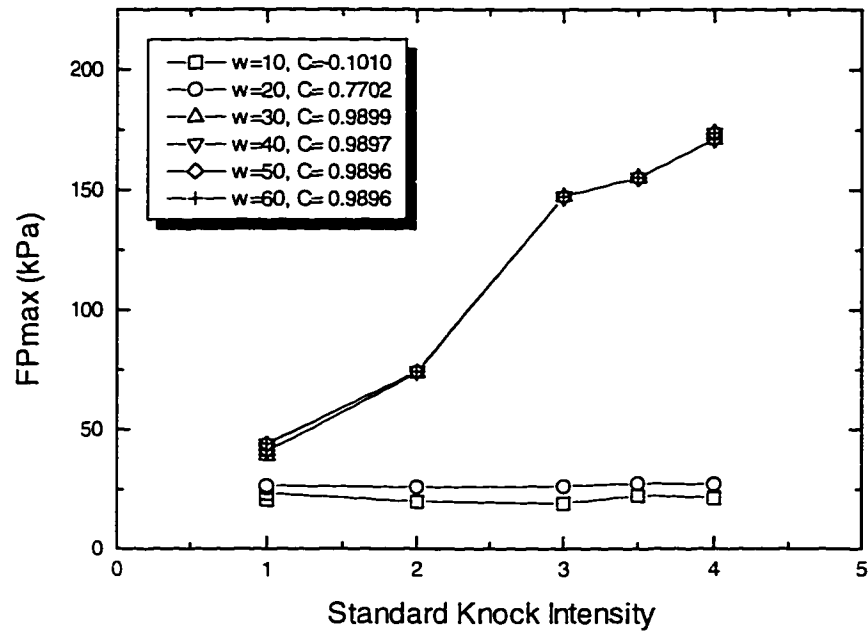


Figure 5.5 Correlation of Maximum Filtered Pressure to Standard Knock Intensity, Using Various Data Window Lengths, 1500 rpm

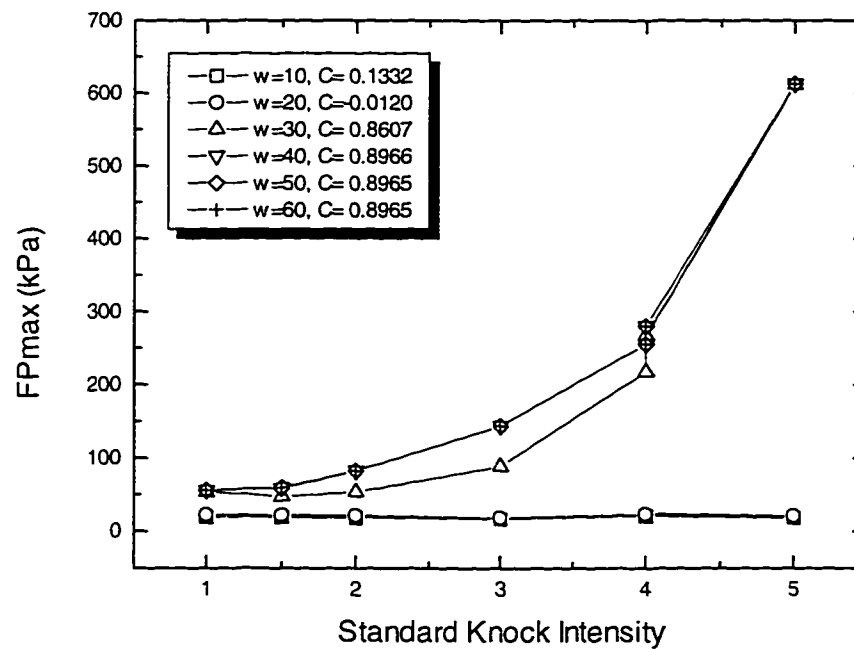


Figure 5.6 Correlation of Maximum Filtered Pressure to Standard Knock Intensity, Using Various Data Window Lengths, 2100 rpm

In Figure 5.6, it is also evident that at least a 30-degree window is required. The 10° and 20° windows suffer the same insensitivity at 2100 rpm as they did at 1500 rpm. In fact, at this higher speed it is not until the window is 40° long or more that the correlation reaches its relatively high maximum value of $C = 0.8966$.

Tables D.3 and D.4 in Appendix D document the correlation between filtered pressure root-mean-square deviation (FPrms) and Standard Knock Intensity. Figure 5.7 shows the calculated data from Table D.3 for the 1500 rpm test. The correlation between FPrms is poor for 10° and 20° windows, and excellent for 30° to 60° windows, achieving a maximum correlation of 0.9907 at 40 degrees. Figure 5.8 is very reminiscent of Figure 5.6 in that the 30-degree window gives a relatively good correlation, while windows 40 degrees and longer provide excellent agreement. The maximum correlation between FPrms and SKI is 0.9063, and occurs with a 40-degree window.

The third pressure statistic to be considered is the peak amplitude of a Fourier transformation of the windowed data. A simple FT routine examines the spectral content of the filtered pressure signal. The frequency with the greatest spectral energy content results in the highest amplitude peak in the FT results array. Figure 5.9 depicts the correlation between FT amplitude (FPamp) and SKI at 1500 rpm, as found in Table D.5. Once again, the maximum correlation occurs with a window length greater than or equal to 30 degrees. The correlation reaches a maximum of $C = 0.9894$ with a 30-degree data window, but the value is virtually as high ($C = 0.9890$ or more) from 30 to 50 degrees. In Figure 5.10, the correlation follows the trend of the previous two statistics at 2100 rpm. At this speed, it once again appears that the best agreement occurs with a window 40° long or longer, with a maximum correlation of over 0.90.

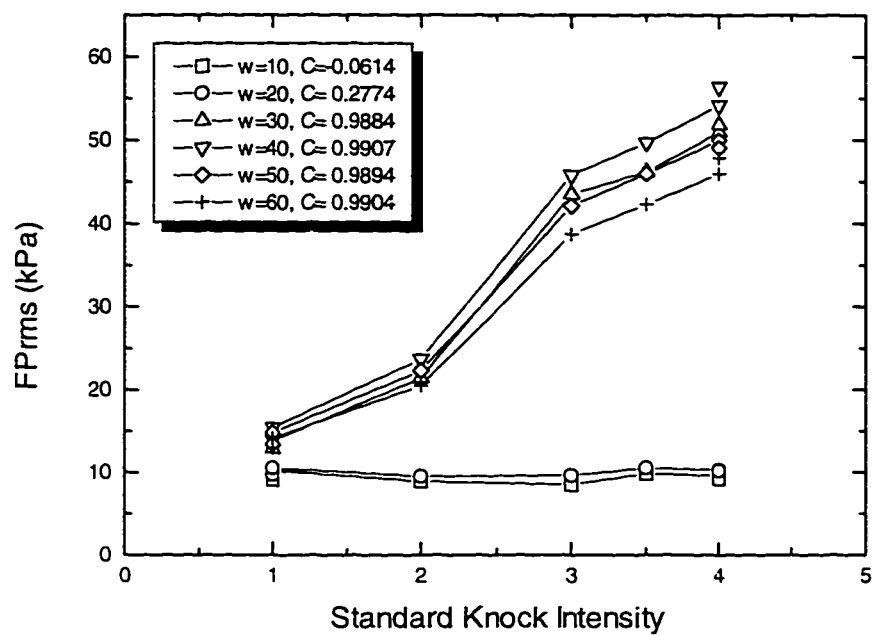


Figure 5.7 Correlation of RMS Filtered Pressure to Standard Knock Intensity, Using Various Data Window Lengths, 1500 rpm

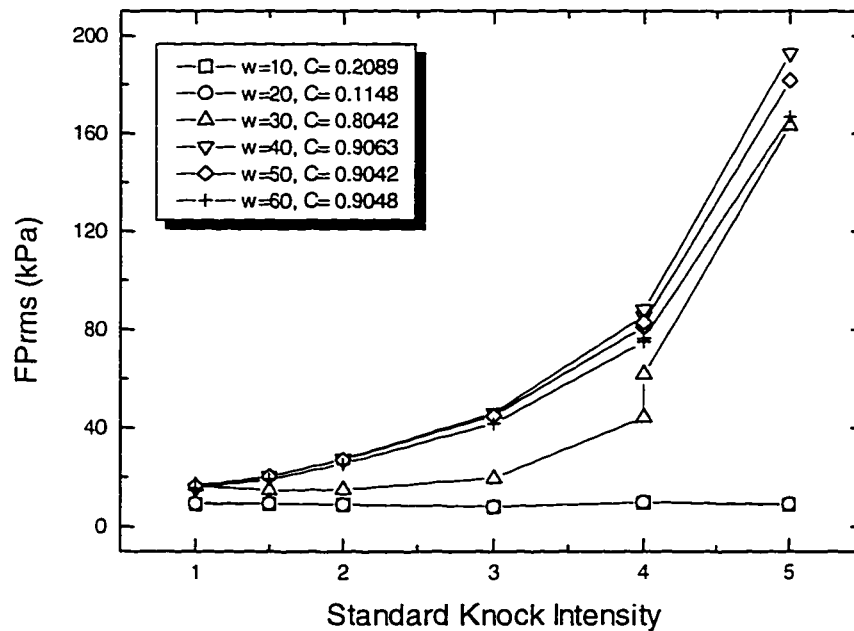


Figure 5.8 Correlation of RMS Filtered Pressure to Standard Knock Intensity, Using Various Data Window Lengths, 2100 rpm

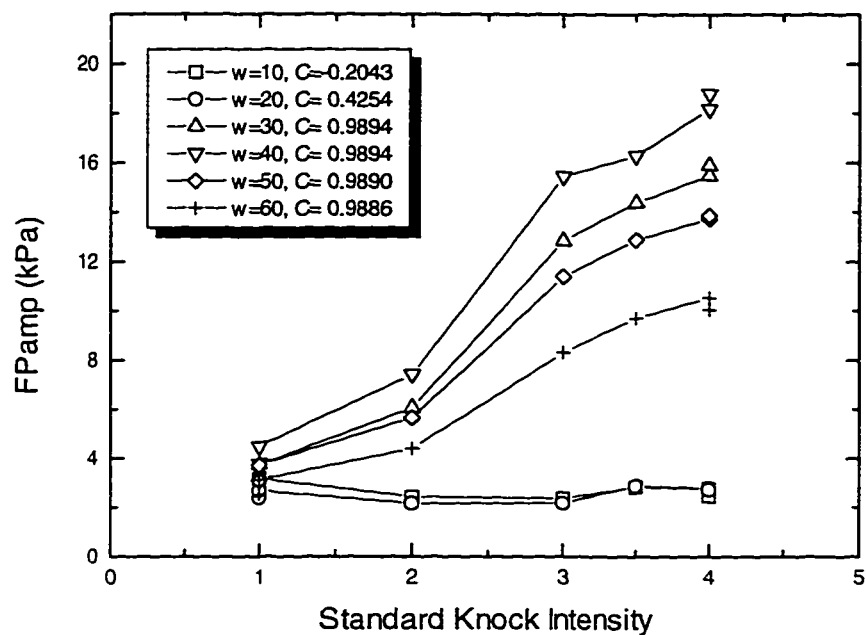


Figure 5.9 Correlation of Filtered Pressure FT Amplitude to Standard Knock Intensity, Using Various Data Window Lengths, 1500 rpm

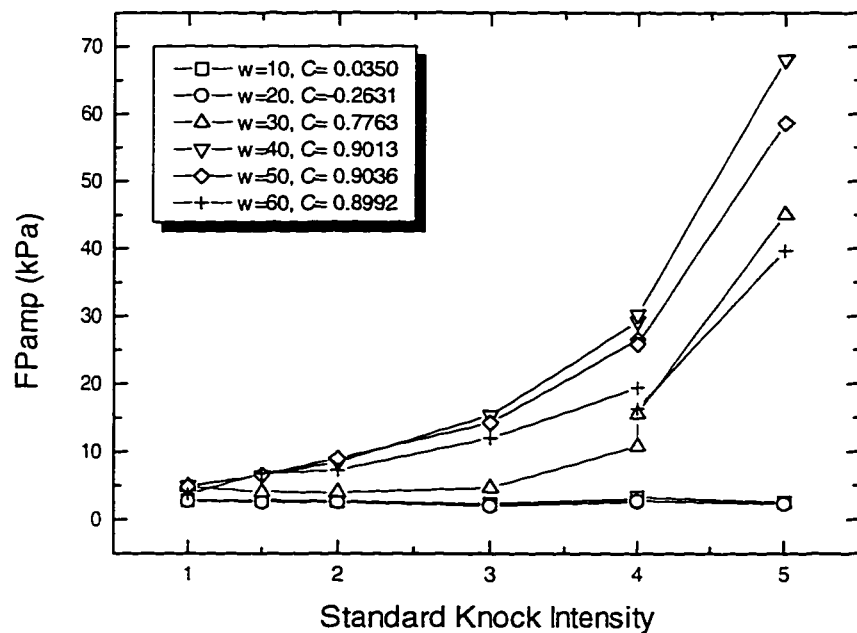


Figure 5.10 Correlation of Filtered Pressure FT Amplitude to Standard Knock Intensity, Using Various Data Window Lengths, 2100 rpm

As Figures 5.5 through 5.10 reveal, 10- and 20-degree windows after maximum pressure are simply too short. These windows consistently result in either a poor correlation between the pressure statistic and knock intensity, or a relatively insensitive statistic. At 1500 rpm, a 30-degree window often provides a correlation as good as longer windows. However, to ensure that the strongest correlations and sensitivities are achieved at all speeds, it is necessary to use a window 40 degrees or more in length.

The correlations of the previous figures and Tables D.1 through D.6 are summarized in Table 5.4 for the 1500 rpm cases and Table 5.5 at 2100 rpm. The highest correlation for each statistic is highlighted in bold type.

Table 5.4 Summary of Pressure Statistic Correlations to SKI, 1500 rpm

Pressure Statistic	Window Length (degrees of crankshaft rotation)					
	10°	20°	30°	40°	50°	60°
Maximum Pressure, P_{max}	0.9662	0.9662	0.9662	0.9662	0.9662	0.9662
Filtered Maximum Pressure, FPmax	-0.1010	0.7702	0.9899	0.9897	0.9896	0.9896
Filtered RMS Pressure, FPrms	-0.0614	0.2774	0.9884	0.9907	0.9894	0.9904
Filtered FT Amplitude, FPamp	-0.2043	0.4254	0.9894	0.9894	0.9890	0.9886

Table 5.5 Summary of Pressure Statistic Correlations to SKI, 2100 rpm

Pressure Statistic	Window Length (degrees of crankshaft rotation)					
	10°	20°	30°	40°	50°	60°
Maximum Pressure, P_{max}	0.9048	0.9048	0.9048	0.9048	0.9048	0.9048
Filtered Maximum Pressure, FPmax	0.1332	-0.0120	0.8607	0.8966	0.8965	0.8965
Filtered RMS Pressure, FPrms	0.2089	0.1148	0.8042	0.9063	0.9042	0.9048
Filtered FT Amplitude, FPamp	0.0350	-0.2631	0.7763	0.9013	0.9036	0.8992

Since maximum pressure is invariant with window length, its correlation is a constant value for each speed. All of the other statistics agree well with observed knock intensity as long as a suitably long window is analyzed. The highest correlation at both speeds has been achieved with the filtered pressure RMS in a 40-degree long data window. If the numerical correlation was the only factor in choosing the optimum statistic, FP_{rms} would be selected. However, to function well as a practical knock indicator, a statistic must balance strong numerical correlation to SKI with a wide dynamic range. Figures 5.11 and 5.12 compare the ranges of the best FP_{max}, FP_{rms}, and FP_{amp} cases of Table 5.4 and Table 5.5. These figures show that each statistic correlates similarly (and well) to SKI, but FP_{max} has the greatest dynamic range. For this reason, maximum filtered pressure has been chosen as the optimum pressure statistic.

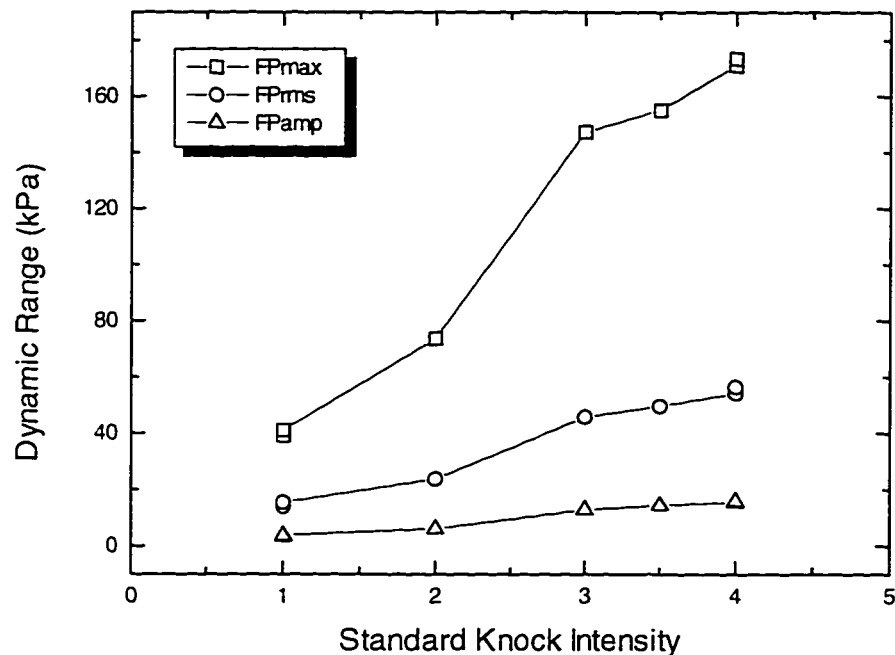


Figure 5.11 Statistical Dynamic Range Comparison, Pressure Investigation, 1500 rpm

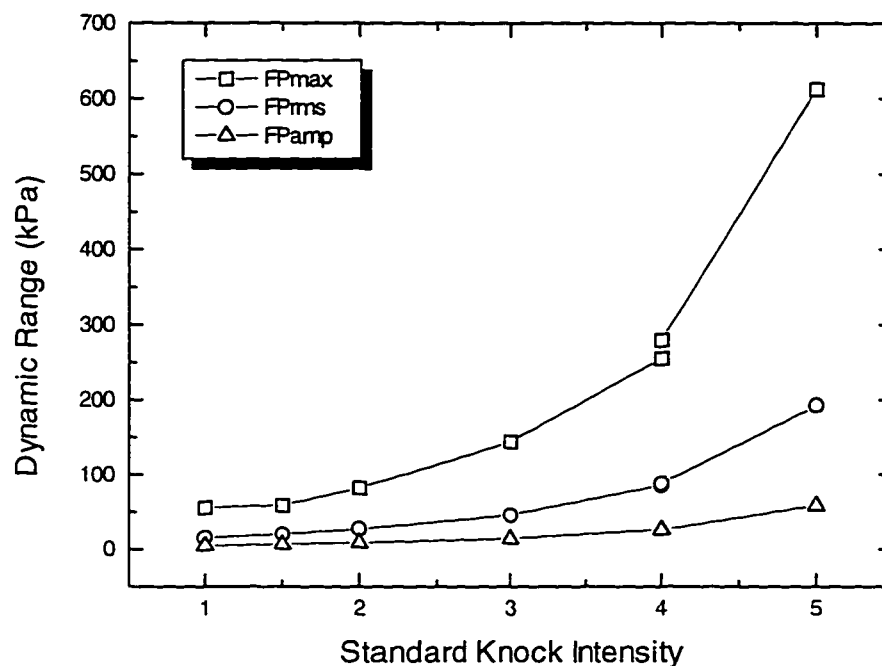


Figure 5.12 Statistical Dynamic Range Comparison, Pressure Investigation, 2100 rpm

Having chosen a statistic (FPmax) and window length (40° after P_{max}) based on the gaseous overfuelling experiment, these selections were checked using the pilot reduction data. In Tables D.7 and D.8 of Appendix F, the correlations between the four major statistics and SKI are listed for a 40 degree window after maximum pressure. Each technique worked fairly well as an indicator of knock, but FPmax correlated well at both speeds while maintaining the widest dynamic range. The correlations for both experiments are apparent in Figure 5.13 and Figure 5.14.

At each speed, maximum filtered pressure consistently rose with observed knock severity. There is a clear difference in FPmax magnitude between weak and heavy levels of knock. Thus, FPmax proves to be not only an absolute indicator of knock, but also a suitable indicator of the relative intensity of knock. This provides a purely quantitative knock detection method which correlates well with the accuracy of a skilled human observer.

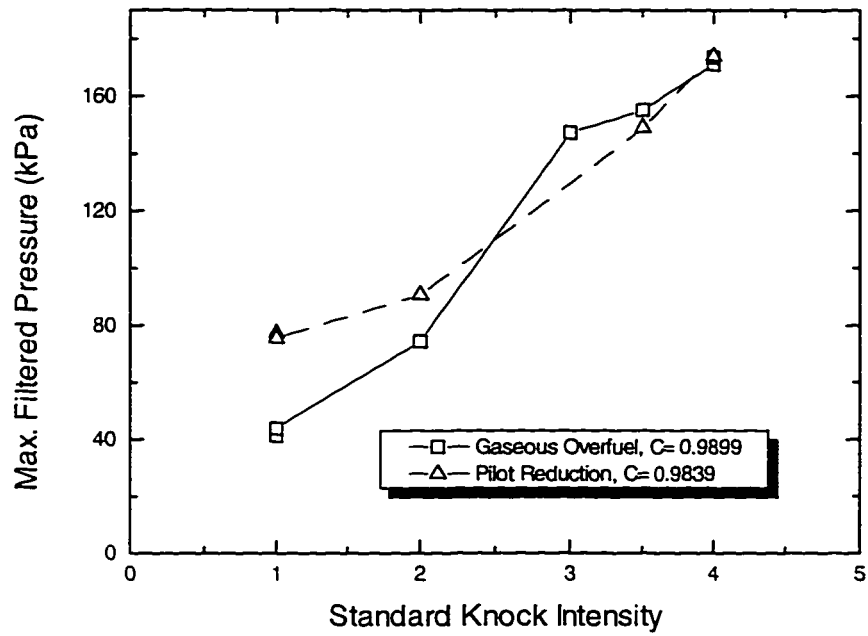


Figure 5.13 Correlation of Optimum FPmax Statistic to SKI, 1500 rpm

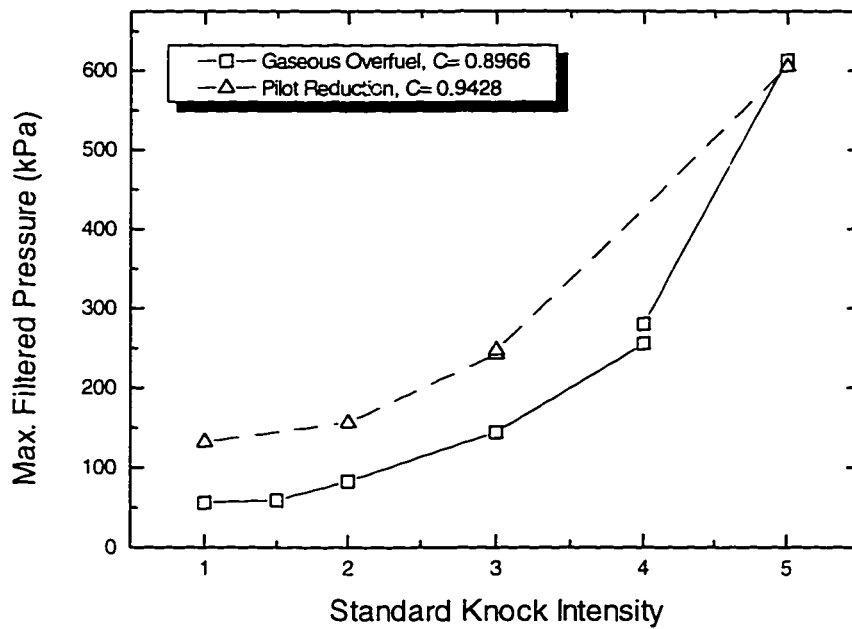


Figure 5.14 Correlation of Optimum FPmax Statistic to SKI, 2100 rpm

5.6 Investigation of Non-Intrusive Statistics

5.6.1 Accelerometer Data Window Start Point

After identifying a reliable knock sensor based on cylinder pressure measurements, the next challenge was to find a non-intrusive sensory method that worked equally well. In mass-production spark-ignition engines, vibration sensors mounted on the engine block have been shown to adequately detect the vibrational energy caused by knock. The problem was to establish such a system with a much heavier, stiffer compression-ignition engine block.

In the pressure trace analysis of Section 5.5, the window of signal selected for analysis always started at the point of maximum pressure. It was shown that the optimum window length after P_{\max} was 40 crankshaft degrees. Apparently, this window best captured the “ringing” oscillations on the pressure trace; a window shorter than 40 degrees missed part of the ringing signal, while a window much longer than 40 degrees was diluted by extraneous non-knocking data. As an initial estimate, it seems reasonable that the block should vibrate for approximately the same duration as the in-cylinder reverberations.

However, it was not positively known how long it would take for end-gas explosions to manifest themselves as increased accelerometer vibration. The time taken for pressure wave energy striking the cylinder walls to reflect through the engine’s block is very short. At the speed of sound through iron (5130 m/s, [52]), it requires only 78 microseconds for energy to reach an accelerometer 40 centimetres away. However, it might take somewhat longer for the vibration to induce a strong response from the sensor’s piezoelectric elements. To ensure that the accelerometer data window was truly optimized, the optimum window start point was determined statistically.

Table 5.1 showed that P_{\max} occurred at approximately 12 degrees ATDC at 1500 rpm and near 16 degrees ATDC at 2100 rpm with the engine knocking moderately heavily. These two start points, augmented with several others earlier and later in the cycle, were used to test for optimum accelerometer window start point. While the exact angle of P_{\max} was known for every cycle during the pressure analysis, such information was not available from the accelerometer signal. Therefore, every window of vibration sensor output was synchronized to a selected crankshaft angle.

A 40°-wide window of data was analyzed for the start points listed in Tables 5.6 and 5.7. Three accelerometer statistics were calculated after the vibration data was bandpass filtered from 6 kHz to 8 kHz (the same filter used in the pressure analysis). One hundred consecutive cycles from the gaseous overfuelling experiment were examined for maximum filtered acceleration (F_{Amax}), filtered RMS acceleration (F_{Arms}), and Fourier transform amplitude (F_{Aamp}). The mean values of each statistic were correlated to the corresponding maximum filtered pressure (FP_{max}) values. With each statistic, the maximum correlation has been highlighted in bold type. Table 5.6 and Table 5.7 are based on data extracted from Tables E.1 to E.6 in Appendix E.

Table 5.6 Effect of Window Start Point on Accelerometer Correlations, 1500 rpm

Start Degree (ATDC)	Correlation to FP _{max}		
	F _{Amax}	F _{Arms}	F _{Aamp}
0	0.8081	0.7755	0.0475
4	0.8081	0.7961	0.2229
8	0.8081	0.7993	0.3853
12 (P_{\max})	0.8136	0.8154	0.3230
16	0.8105	0.8100	0.5130
20	0.7923	0.7889	0.4658

Table 5.6 shows that the F_{Amax} and F_{Arms} values were much more reliable than the Fourier transform amplitude. F_{Amax} and F_{Arms} both correlated to FP_{max} with better than 0.80 proficiency, compared to the 0.0 - 0.5 performance of FP_{amp}. This was likely

due to other randomly-phased block vibrations interfering with the transmission of knock energy. Given the limited number of vibration cycles in each sample window, the phase-shifting from background vibrations produced an apparent spread in vibration frequency. The FT routine looked for a clear “spike” of energy in a very narrow spectrum, and if the data entering the routine was distributed among several frequencies instead of being concentrated at one fundamental frequency, the peak transform amplitude would have dropped. Table 5.6 shows that at 1500 rpm, the knocking signal that reaches the vibration sensor was not focused at one particular frequency, thus there is a poor correlation between FAamp and maximum filtered pressure.

At 2100 rpm, Table 5.7 suggests that Fourier transform amplitude works even better than the other two statistics. However, its poor performance in the lower-speed trials rule it out as a reliable knock detector. RMS and maximum filtered acceleration, on the other hand, continue to correlate quite well with FPmax. At both speeds, the best agreement between these two statistics and FPmax occurs when the window is synchronized to start at the angle approximating P_{\max} , i.e. 12 degrees ATDC at 1500 rpm and 16 degrees ATDC at 2100 rpm.

Table 5.7 Effect of Window Start Point on Accelerometer Correlations, 2100 rpm

Start Degree (ATDC)	Correlation to FPmax		
	FMax	FArms	FAamp
4	0.8368	0.8558	0.7582
8	0.8368	0.8597	0.8571
12	0.8368	0.8601	0.8684
16 (P_{\max})	0.8368	0.8620	0.8691
20	0.8311	0.8595	0.8121
24	0.7849	0.8532	0.8519

Note that in Tables 5.6 and 5.7, the maximum correlations are significantly lower than the 0.90 to 0.99 listed in Tables 5.4 and 5.5 for the pressure analysis. This suggests that the correlation between block vibration and knock intensity is not as strong as it is for the

in-cylinder transducer. For extra insurance, both the gaseous overfuelling and pilot reduction experiments were analyzed for the balance of the accelerometer investigation.

5.6.2 Accelerometer Data Window Length and Best Statistic, Overfuelling Experiment

With a suitable window start point chosen for each engine speed, the effect of window length was also examined. Six different data window lengths were investigated, ranging from 10 to 60 crankshaft degrees. Three acceleration statistics were calculated for each window, then correlated to maximum filtered pressure. Figures 5.15 through 5.20 show the correlation of each statistic to FPmax at 1500 and 2100 rpm for the gaseous overfuelling experiment, based on data in Appendix F, Tables F.1 through F.6. The filtered accelerometer values portrayed in this section have been assigned the units of g^* to reflect the fact that, as Section 3.3 described, the instrument's output is known to be directly proportional to acceleration but could not be calibrated absolutely.

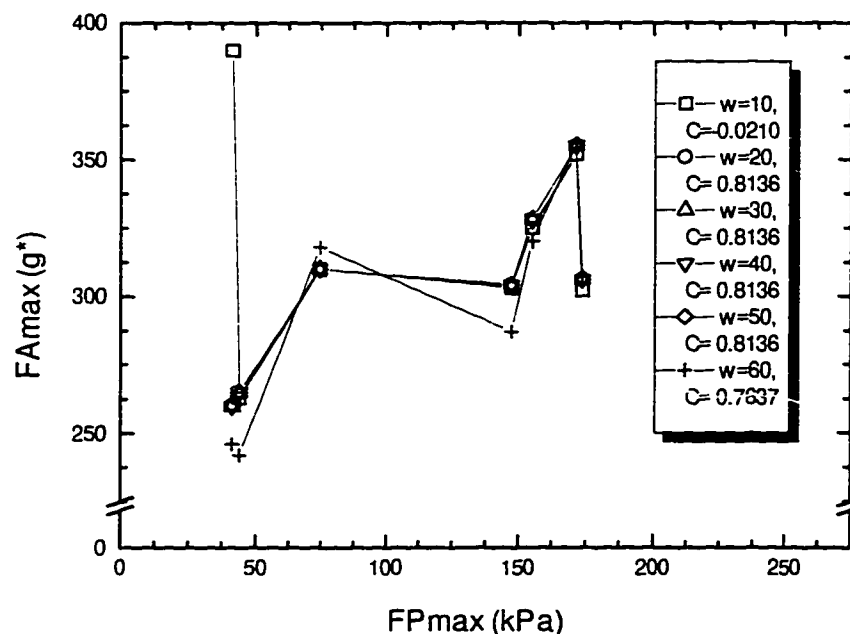


Figure 5.15 Correlation of Fmax to FPmax Using Various Data Window Lengths, Overfuelling Experiment, 1500 rpm

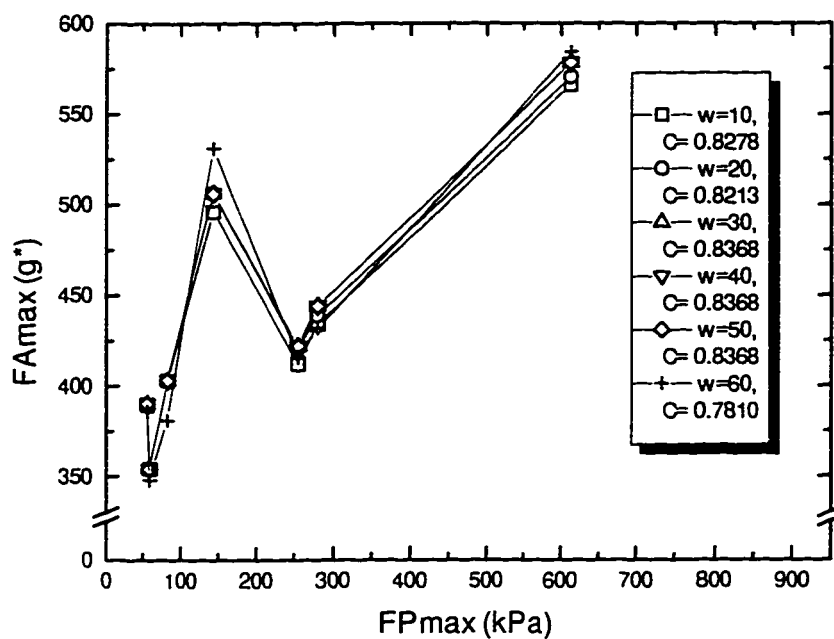


Figure 5.16 Correlation of FAmx to FPmax Using Various Data Window Lengths, OverfueLLing Experiment, 2100 rpm

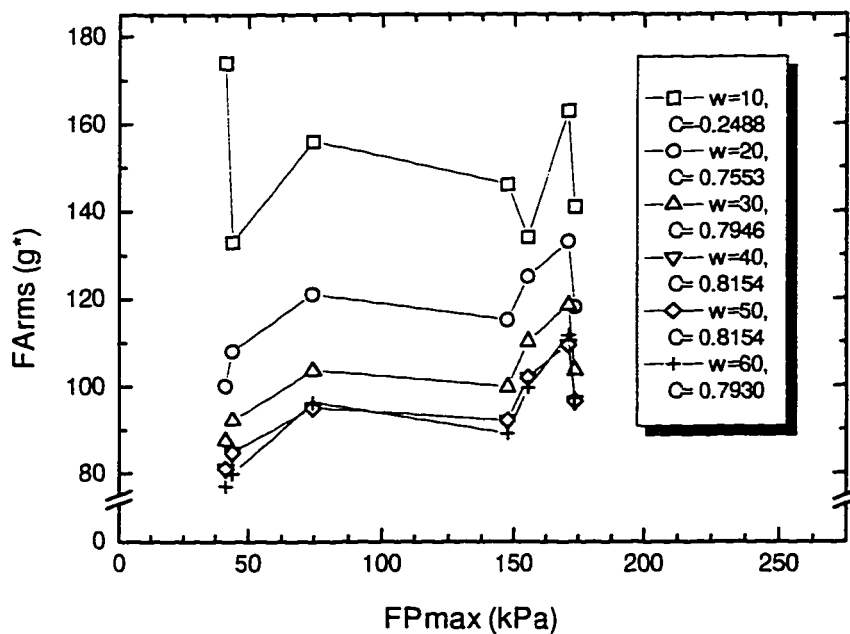


Figure 5.17 Correlation of FArms to FPmax Using Various Data Window Lengths, OverfueLLing Experiment, 1500 rpm

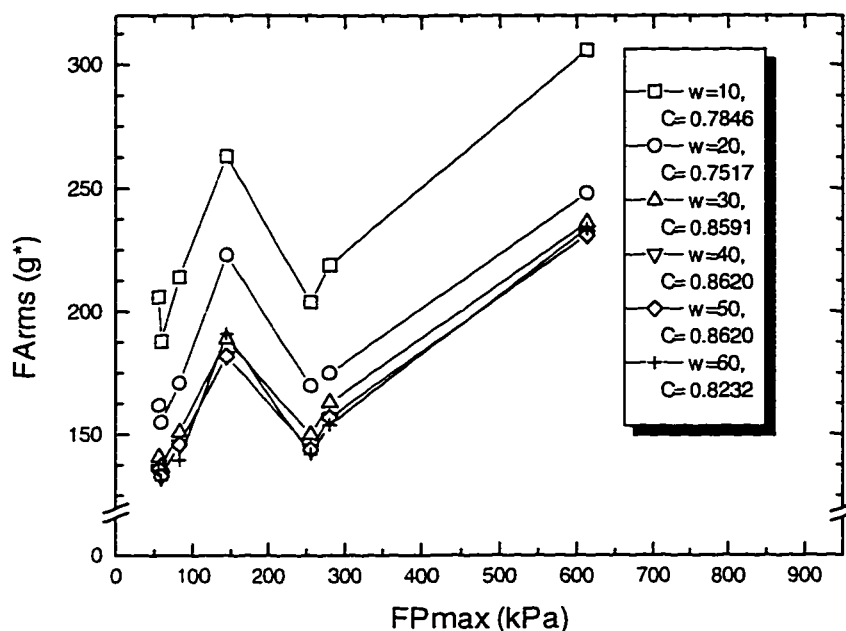


Figure 5.18 Correlation of FARms to FPmax Using Various Data Window Lengths, OverfueLLing Experiment, 2100 rpm

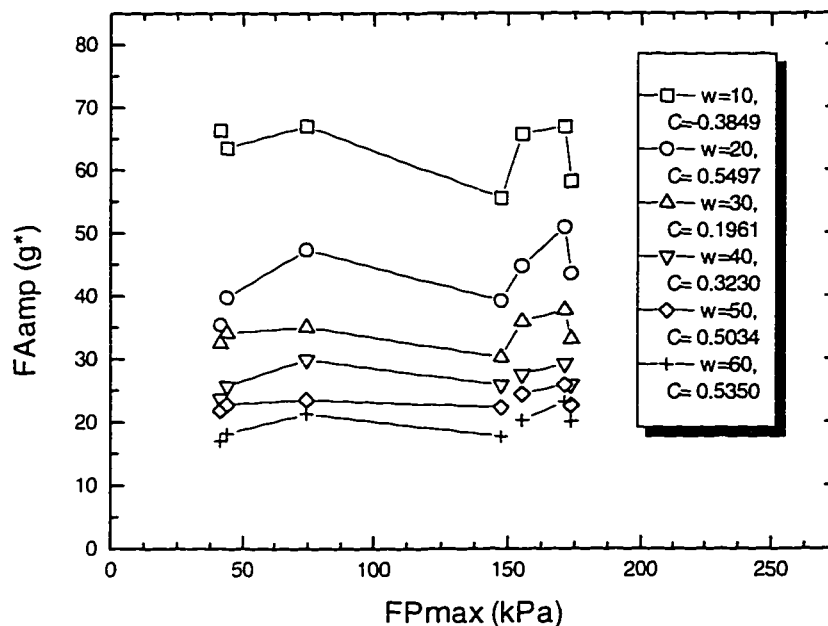


Figure 5.19 Correlation of FAamp to FPmax Using Various Data Window Lengths, OverfueLLing Experiment, 1500 rpm

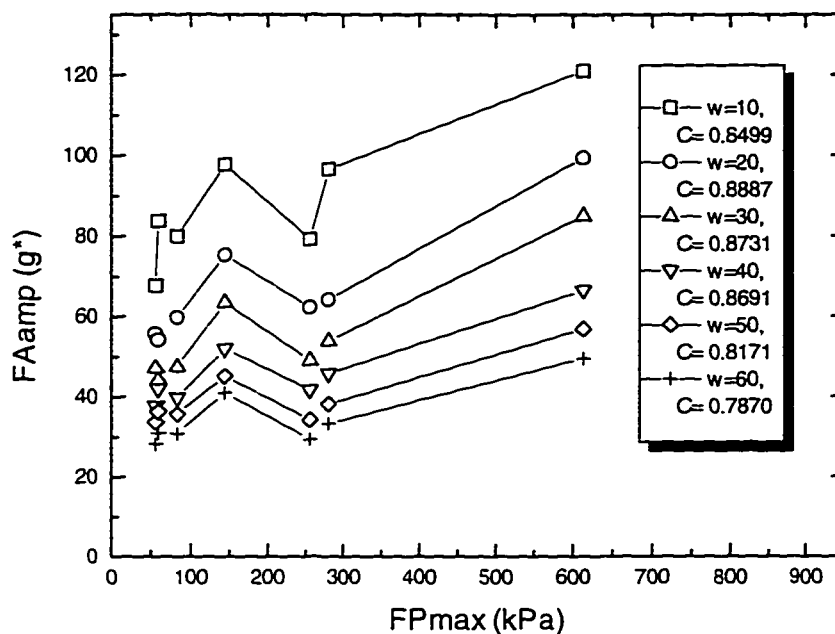


Figure 5.20 Correlation of FAamp to FPmax Using Various Data Window Lengths, Overfuelling Experiment, 2100 rpm

Table 5.8 summarizes the previous figures numerically. The maximum correlation value for each statistic at each speed is highlighted in bold type. The maximum and RMS values of the filtered accelerometer signal (FMax and FArms, respectively) correlate consistently well with FPmax. The correlation values for these statistics at 1500 and 2100 rpm are greater than 0.80 for 40- or 50-degree data windows. Figures 5.15 to 5.18 confirm that there is reasonable statistical resolution to differentiate between light and heavy knock with longer windows. The Fourier transform amplitude correlates well at 2100 rpm, but its maximum correlation coefficient at 1500 rpm is a relatively poor 0.5497. As well, Figures 5.19 and 5.20 reveal that the difference in FAamp value between knock intensities is relatively small regardless of window length.

Table 5.8 Correlation of Accelerometer Statistics to FPmax, OverfueLLing Experiment

Engine Speed (rpm)	Window Length (deg.)	Correlation to FPmax		
		FAm _{ax}	FAR _{ms}	FA _{amp}
1500	10	-0.0210	-0.2488	-0.3849
1500	20	0.8136	0.7553	0.5497
1500	30	0.8136	0.7946	0.1961
1500	40	0.8136	0.8154	0.3230
1500	50	0.8136	0.8154	0.5034
1500	60	0.7637	0.7930	0.5350
2100	10	0.8278	0.7846	0.8499
2100	20	0.8213	0.7517	0.8887
2100	30	0.8368	0.8591	0.8731
2100	40	0.8368	0.8620	0.8691
2100	50	0.8368	0.8620	0.8171
2100	60	0.7810	0.8232	0.7870

The best correlations listed in Table 5.8 are plotted in Figures 5.21 and 5.22. Once again, while both FAm_{ax} and FAR_{ms} correlate quite strongly with FPmax, maximum filtered acceleration (FAm_{ax}) has the greatest dynamic range of the three statistics under consideration. As a result, FAm_{ax} (as measured within a 30°-50° data window after P_{max}) is the preliminary choice for optimum vibration statistic.

5.6.3 Accelerometer Data Window Length and Best Statistic, Pilot Experiment

The results for the pilot reduction experiment are quite similar to the gaseous overfueLLing tests. Figures 5.23 through 5.28 show the relationships between the three accelerometer statistics and the FPmax standard at both speeds. Table 5.9 summarizes the findings of this experiment, which are tabulated fully in Tables F.7 to F.12 of Appendix F.

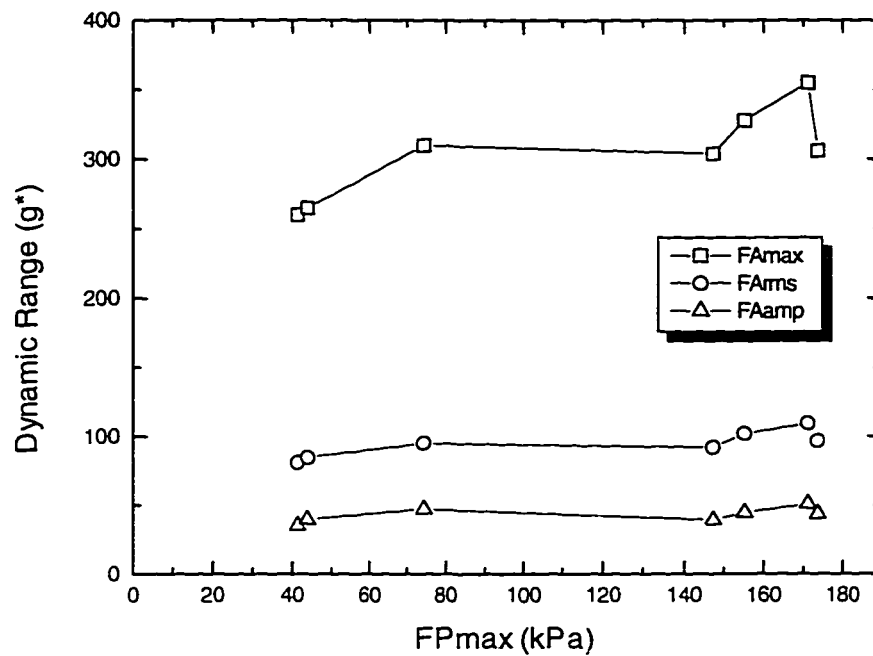


Figure 5.21 Accelerometer Statistic Dynamic Range Comparison, OverfueLLing Experiment, 1500 rpm

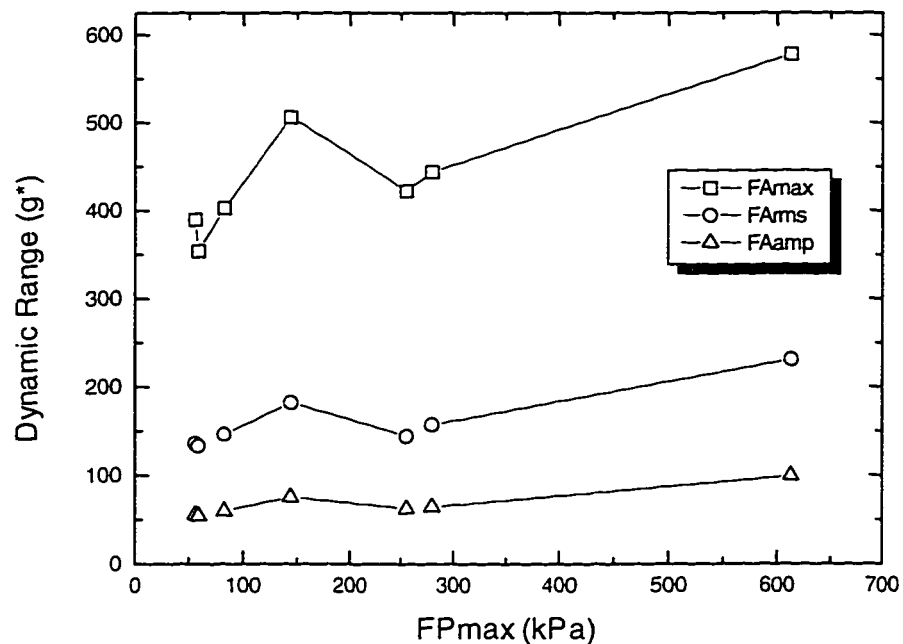


Figure 5.22 Accelerometer Statistic Dynamic Range Comparison, OverfueLLing Experiment, 2100 rpm

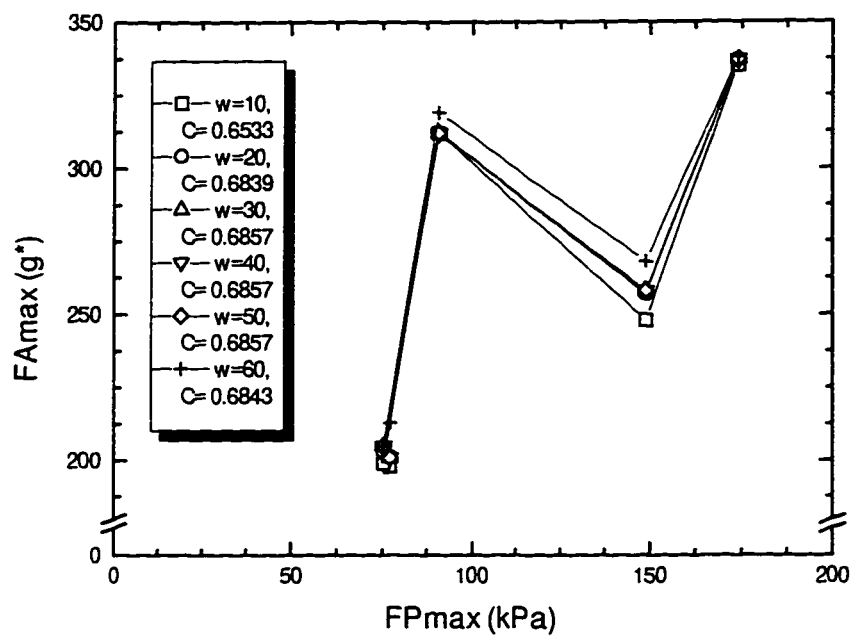


Figure 5.23 Correlation of Fmax to FPmax Using Various Data Window Lengths, Pilot Experiment, 1500 rpm

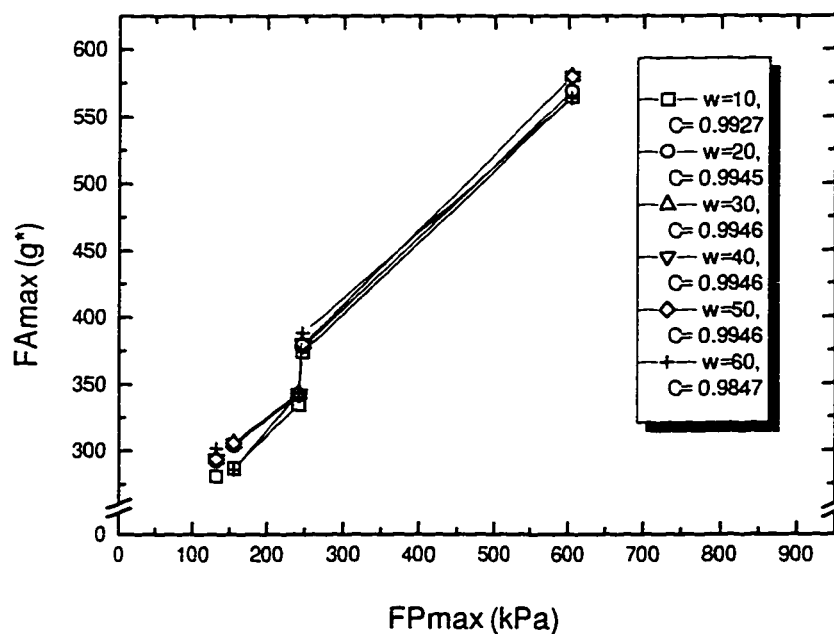


Figure 5.24 Correlation of Fmax to FPmax Using Various Data Window Lengths, Pilot Experiment, 2100 rpm

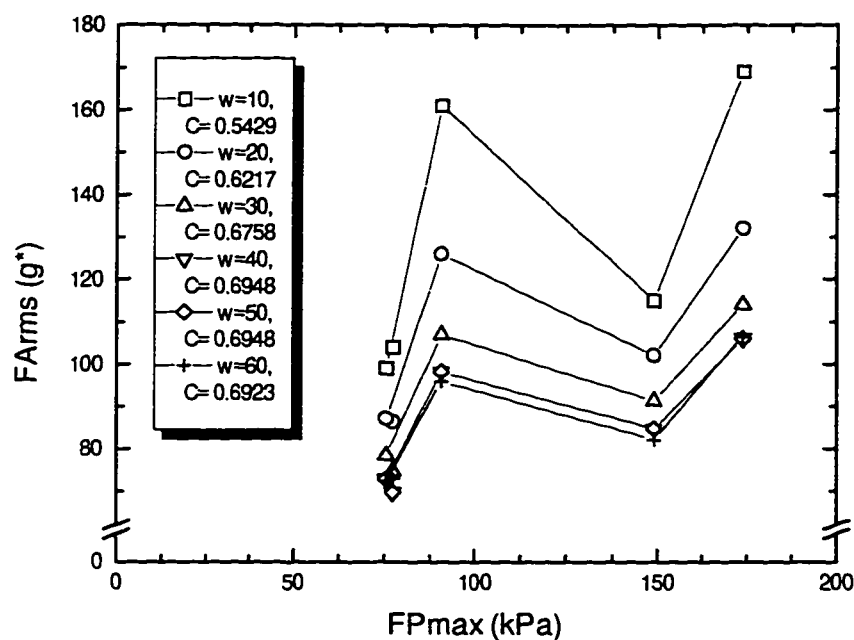


Figure 5.25 Correlation of FARms to FPmax Using Various Data Window Lengths, Pilot Experiment, 1500 rpm

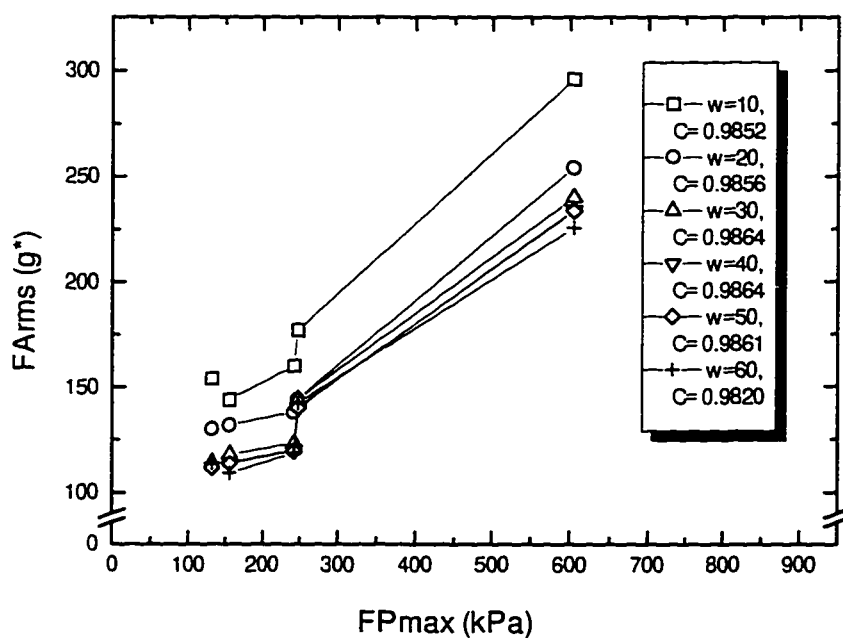


Figure 5.26 Correlation of FARms to FPmax Using Various Data Window Lengths, Pilot Experiment, 2100 rpm

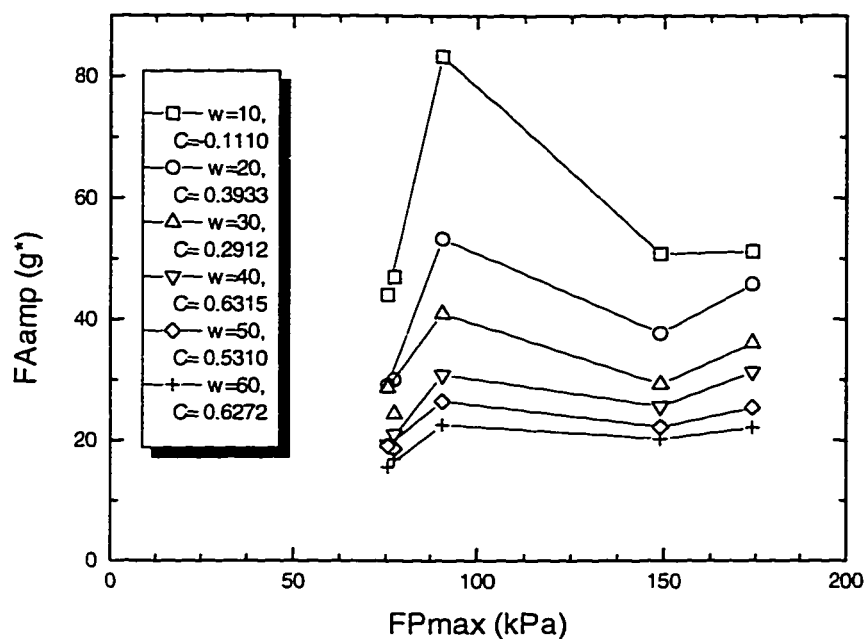


Figure 5.27 Correlation of FAamp to FPmax Using Various Data Window Lengths, Pilot Experiment, 1500 rpm

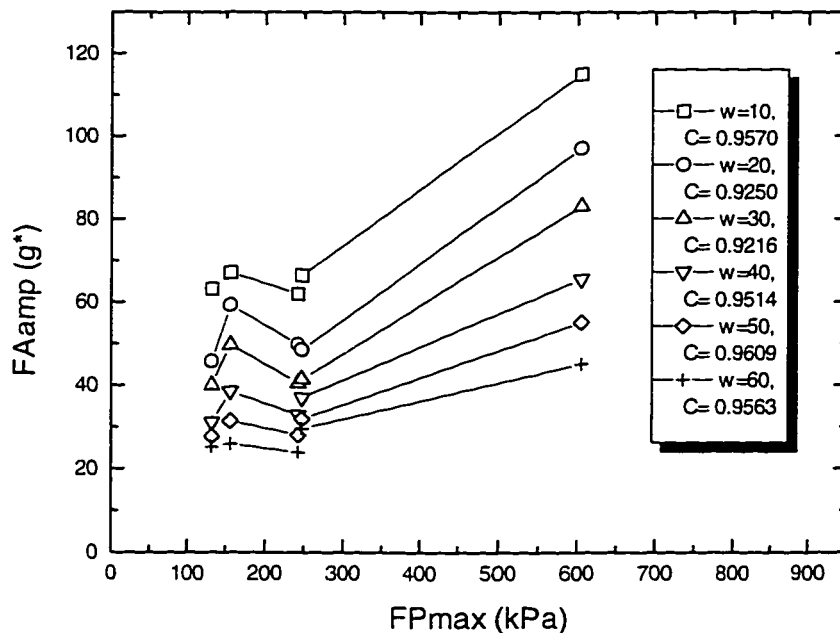


Figure 5.28 Correlation of FAamp to FPmax Using Various Data Window Lengths, Pilot Experiment, 2100 rpm

Table 5.9 Correlation of Accelerometer Statistics to FPmax, Pilot Experiment

Engine Speed (rpm)	Window Length (deg.)	Correlation to FPmax		
		FMax	FArms	FAamp
1500	10	0.6533	0.5429	-0.1110
1500	20	0.6839	0.6217	0.3933
1500	30	0.6857	0.6758	0.2912
1500	40	0.6857	0.6948	0.6315
1500	50	0.6857	0.6948	0.5310
1500	60	0.6843	0.6986	0.6272
2100	10	0.9927	0.9852	0.9570
2100	20	0.9945	0.9856	0.9250
2100	30	0.9946	0.9864	0.9216
2100	40	0.9946	0.9864	0.9514
2100	50	0.9946	0.9861	0.9609
2100	60	0.9847	0.9820	0.9563

As in the overfuelling experiment, FMax and FArms were more consistent than FAamp. In this experiment, the maximum correlation to FPmax at 1500 rpm was slightly less than 0.70. At 2100 rpm, FMax and FArms both correlated significantly better with the maximum filtered pressure, with FMax agreeing slightly better than FArms. Figure 5.27 in particular reveals the inadequacy of the Fourier transform statistic at 1500 rpm. Even the highest correlation, $C=0.6315$, is accompanied by only a small change in dynamic amplitude between light and heavy knock. Such a small range means it would be very difficult to pick a threshold value for this statistic which did not lead to excessive false-positive errors. This is clearly shown in Figures 5.29 and 5.30, which compare the dynamic ranges of each statistic for the pilot reduction experiment.

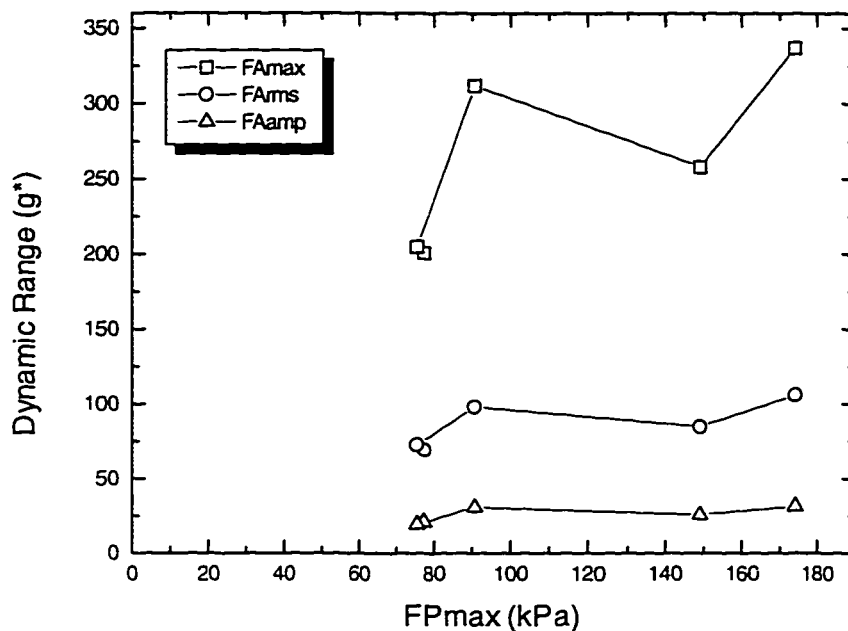


Figure 5.29 Accelerometer Statistic Dynamic Range Comparison, Pilot Experiment, 1500 rpm

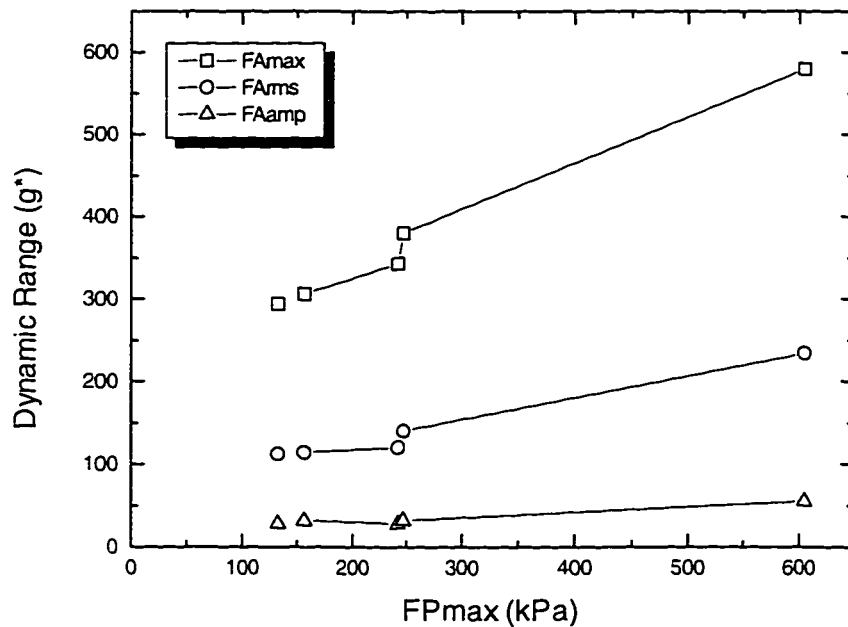


Figure 5.30 Acceleration Statistic Dynamic Range Comparison, Pilot Experiment, 2100 rpm

Considering the information in Table 5.8 and Table 5.9, both the F_{Amax} and F_{Arms} statistics appear to be comparably adept at accurately detecting knock intensity. Both statistics correlated consistently well with the maximum filtered pressure benchmark, and had reasonably good resolution between levels of knock intensity. From a practical use standpoint, quantifying the maximum signal within a window is simpler than calculating an RMS value, since it involves less mathematical operations. Additionally, Figure 5.29 and Figure 5.30 show that the maximum acceleration statistic had a better dynamic range than F_{Arms} . The pilot reduction tests again showed that F_{Amax} gave the best balance of high correlation to FP_{max} and usable dynamic range. Hence, F_{Amax} was chosen as the best non-intrusive knock detection statistic.

The data window leading to the highest sensor correlation was typically 40 crankshaft degrees long, synchronized to the average angle of maximum knocking cylinder pressure. This validated the earlier assumption that the accelerometer would vibrate for approximately the same length of time as the pressure signal was “ringing”. It is interesting to note that window length is more flexible with F_{Amax} than with the other vibration statistics, since windows of lengths from 30° to 50° after P_{max} were repeatedly shown to capture the same points of maximum acceleration.

5.7 Summary of Results

In the first part of this chapter, the maximum value of filtered in-cylinder pressure (FP_{max}) was shown to be an excellent indicator of knock. FP_{max} correlated consistently well with the operator-observed knock intensity scale, SKI , and displayed a high dynamic output range. Using FP_{max} as a quantitative standard, records of block acceleration were analyzed in various ways to attempt to detect knock in cylinder six non-intrusively. It was determined that the accelerometer data window leading to the best results was 40 crankshaft degrees long, starting at the average angle of maximum pressure (12° ATDC for the 1500 rpm tests, 16° ATDC for the 2100 rpm tests). After considering three

different statistics, the maximum value of bandpass-filtered acceleration (F_{Amax}) was chosen as the optimum non-intrusive knock detection technique. Figures 5.31 and 5.32 show the correlation between 100-cycle averages of F_{Pmax} and F_{Amax} for two experiments. In the first experiment, knock was induced in cylinder six by overfuelling it with natural gas, richening the end-gas composition. In the second series of tests, the quantity of the diesel pilot injection was reduced while the CNG content of the intake charge was increased. In both cases, increasing the fuel richness of the end-gas regions of combustion led to stronger knock pressure waves. Figures 5.31 and 5.32 show that F_{Amax} correlated reasonably well with maximum filtered in-cylinder pressure for both experiments at either engine speed.

Having proven that a block-mounted sensor is capable of reliably detecting knock, the focus shifts to using the F_{Amax} statistic for real-time knock control. Figures 5.33 and 5.34 show that as the intensity of knock increases, block vibration increases proportionally. In these particular figures, an acceleration of approximately 280 g* makes a reasonable threshold level between normal and knocking combustion. When a knock control computer has sensed that the previous several consecutive cycles (in this case, 100) have had an average acceleration higher than the threshold limit, the computer can attribute the excessive vibration to knock and take corrective action.

This investigation has discovered that the acceleration threshold is dependent on engine speed, as Figures 5.35 and 5.36 reveal. At 2100 rpm, the threshold value appears to be approximately 410 g*, significantly higher than the 280 g* level at 1500 rpm. Therefore, an effective knock control scheme must be able to accommodate different threshold levels of vibration for various engine speeds, otherwise knock under certain engine conditions could go undetected.

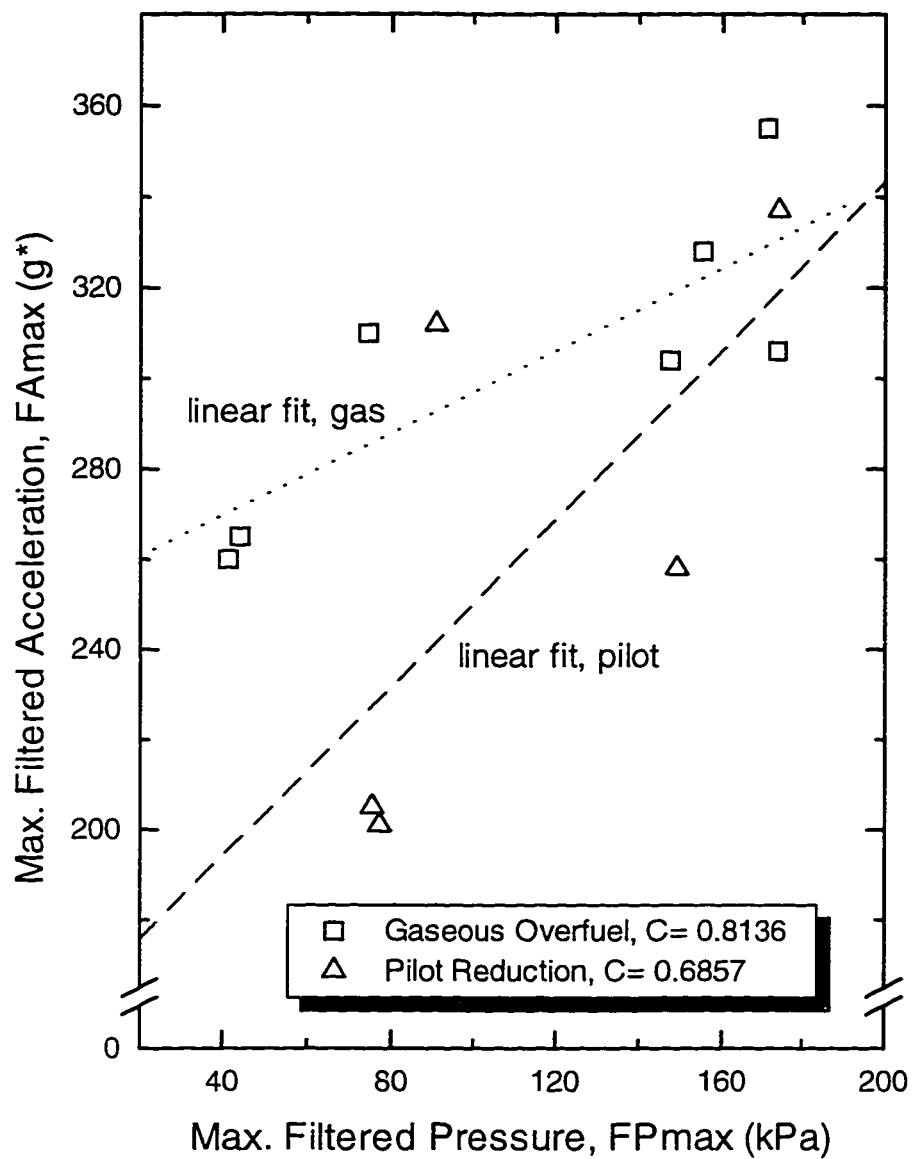


Figure 5.31 Comparison of Best Block Acceleration and Cylinder Pressure Statistics, 1500 rpm

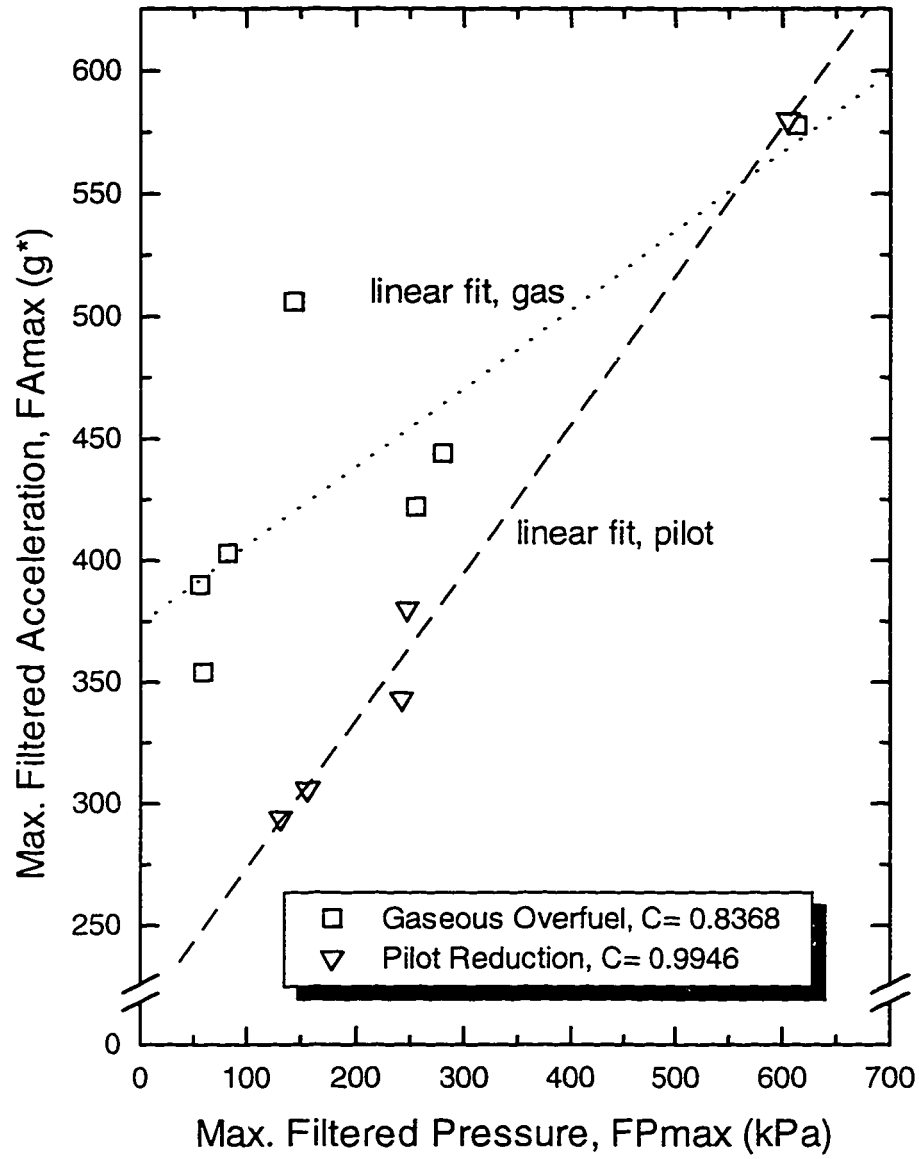


Figure 5.32 Comparison of Best Block Acceleration and Cylinder Pressure Statistics, 2100 rpm

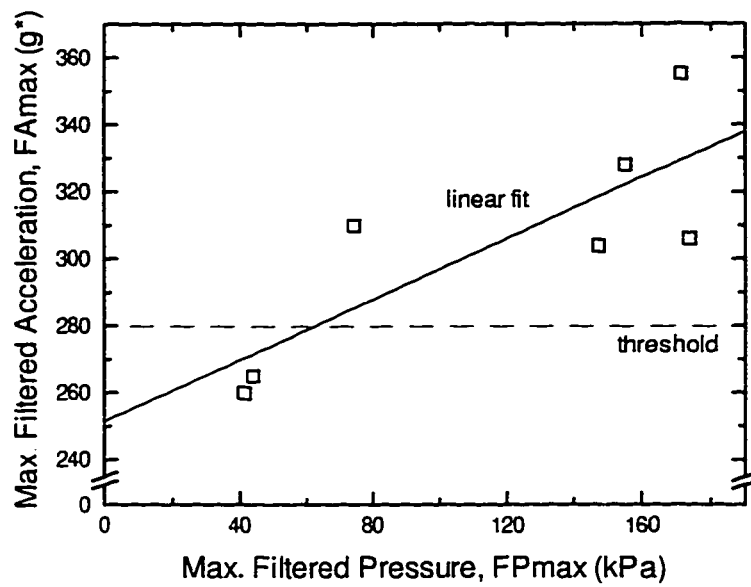


Figure 5.33 Correlation of Best Acceleration Statistic to Best Pressure Statistic, With Suggested Knock Threshold Vibration Level, 1500 rpm

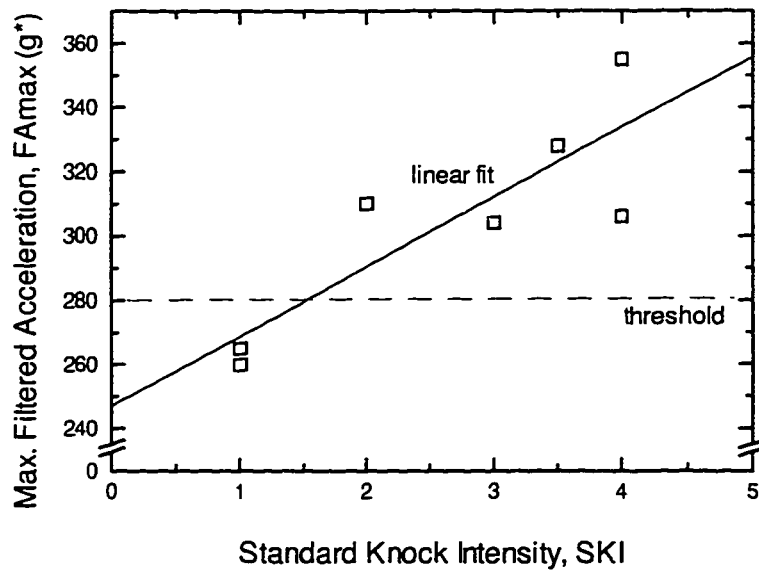


Figure 5.34 Correlation of Best Acceleration Statistic to Observed Knock Intensity, With Suggested Knock Threshold Vibration Level, 1500 rpm

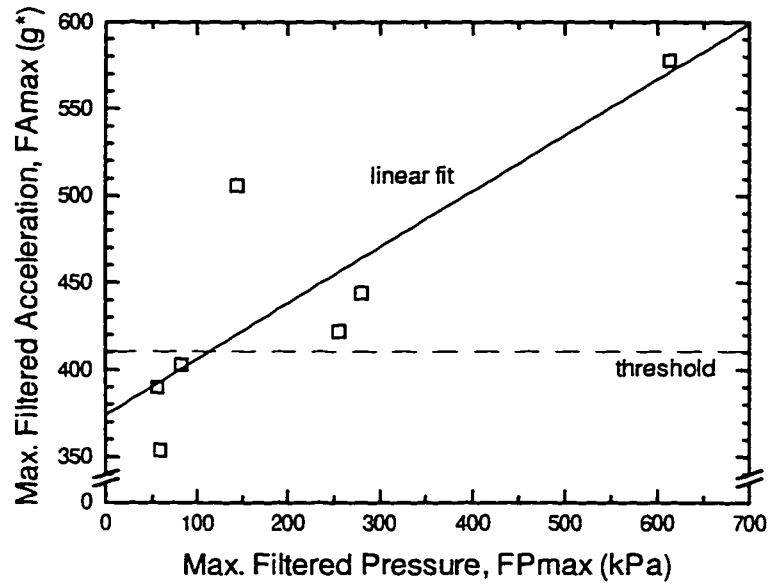


Figure 5.35 Correlation of Best Acceleration Statistic to Best Pressure Statistic, With Suggested Knock Threshold Vibration Level, 2100 rpm

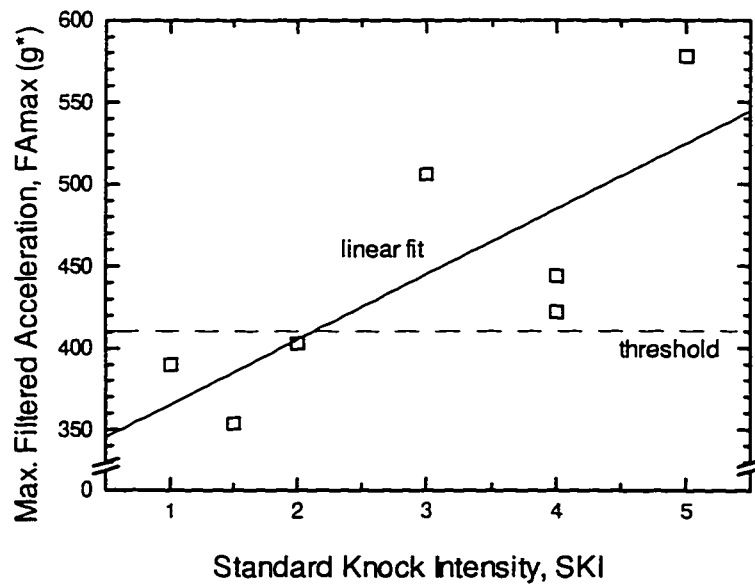


Figure 5.36 Correlation of Best Acceleration Statistic to Observed Knock Intensity, With Suggested Knock Threshold Vibration Level, 2100 rpm

**CONCLUSIONS AND CONSIDERATIONS
FOR FUTURE DEVELOPMENT**

6.1 Summary

“Dual fuel” engines have been proposed to curb the transportation sector’s thirst for diesel fuel while reducing harmful emissions. In a dual fuel engine, most of the diesel used for combustion is displaced by a much cleaner-burning fuel such as compressed natural gas (CNG). However, at high torque levels diesel fuel replacement is limited by “knock”, a destructive process where the gas/air mixture in the far reaches of the combustion cavity violently autoignites. If left unchecked, the excessive heat transfer associated with knock can damage or ruin an engine. Designers of spark-ignition engines commonly use block-mounted accelerometers to detect the onset of knock. Detecting knock through block vibration analysis in dual fuel engines is more problematic, since compression-ignition engines tend to be built much stiffer and heavier than their gasoline-fuelled cousins.

The characteristics of knock in a dual fuel Mercedes OM366LA test engine were investigated at the University of Alberta. The engine was connected to an eddy current dynamometer for torque and speed control. A personal computer was used to directly control the dual fuelling parameters in the engine control module. The sixth cylinder of the OM366LA was customized in two ways; a pressure transducer was installed in its combustion chamber, while its natural gas distribution block was modified to allow a range of gas supply rates. The in-cylinder transducer allowed direct observation of

combustion gas pressure, while a wide-band instrument-grade accelerometer was mounted to the side of the engine to measure block vibration.

Knock was induced in the engine by two different methods. In one series of tests, the sixth cylinder was overfuelled by varying the natural gas delivery pressure. The higher power and concentration of CNG in the chamber's end-gas region led to an increased tendency to knock. In the second set of experiments, knock was induced by increasing the diesel replacement ratio in all cylinders simultaneously. As the pilot fuel injection quantity was reduced, natural gas delivery was increased proportionally, leading to higher knock sensitivity for the same amount of power. The experiments were conducted at 1500 rpm and 2100 rpm to capture the engine's maximum torque point and a common high-speed high-load point, respectively. Combustion pressure and block acceleration were recorded during each experiment by a frequency-modulated tape recorder. Signals were later digitized and analyzed with a personal computer.

The first step in determining knock intensity was the definition of an operator-observed knock index. The human ear is an excellent discriminator of audible engine knock. A Standard Knock Intensity (SKI) scale from 1 to 5 was adopted in the laboratory as the primary quasi-quantitative knock measurement. The OM366LA was made to knock with varying severity under controlled conditions. An appropriate SKI value was selected by the operators for each condition, while pressure and acceleration records were simultaneously recorded for off-line analysis.

Since the pressure transducer directly measured the fluctuating-pressure knock phenomenon, it was expected to be the best quantitative indicator of knock intensity. The pressure signal was digitally bandpass filtered to remove the low-frequency offset of normal combustion and random high-frequency noise. A window of pressure data was computer analyzed for maximum and RMS values as well as spectral content. A

preliminary pressure trace investigation suggested that the fundamental knock frequency was near 7300 Hertz under heavy knock conditions.

When knock occurred, cylinder pressure resonated for several milliseconds. This resonance appeared in the filtered pressure trace as an oscillating function of decreasing amplitude. For the pressure analysis, the start of the data window was always synchronized to the point of highest pressure, which was experimentally observed to approximately coincide with the beginning of the oscillation. The length of the window after this common start point was varied from 10 to 60 crankshaft degrees. Maximum filtered pressure (FPmax), filtered RMS pressure (FPrms) and Fourier-transformed amplitude (FPamp) were calculated for each window and correlated to the SKI index for each condition. The statistic that correlated the best with the SKI at both engine speeds while maintaining a wide dynamic range was FPmax. At 1500rpm, FPmax and SKI showed excellent agreement, with a peak correlation factor near 0.99. The correlation was slightly lower at 2100, but still registered a respectable 0.90. It was also determined that the window length that led to the best pressure statistics was a 40° span after P_{max} . Based on its strong correlation with the SKI scale and its wide sensitivity range, FPmax was adopted as the standard instrument-derived knock intensity measurement.

The accelerometer's output was statistically analyzed and correlated to FPmax. A 40° window of knocking accelerometer data was synchronized to a range of start points near the angle corresponding to P_{max} at each speed. The accelerometer's statistics were shown to be the most sensitive when the window was started at P_{max} , coinciding with the windows used in the pressure analysis. This negated concerns about a possible time lag between the onset of pressure fluctuations and the beginning of accelerometer output.

With the starting time fixed near P_{max} , the accelerometer data window length was varied from 10 to 60 crankshaft degrees. It was shown that a window length of 40 crankshaft degrees was appropriate for maximizing the vibration sensor's accuracy. Three statistics

were calculated for each window, including filtered maximum acceleration (FAMax), filtered RMS acceleration (FARms), and the maximum amplitude of the sample's Fourier transform (FAamp). Both FAMax and FARms appeared to correlate fairly well with knock intensity. In the overfuelling experiment, average values of FAMax and FARms correlated with better than 0.80 effectiveness to the average values of maximum filtered pressure. For the pilot reduction experiment, both statistics worked less effectively at low speed (approximately $C = 0.70$), but correlated very well at high speed, with more than a 0.98 agreement. The maximum filtered acceleration statistic, FAMax, was selected as the best non-intrusive knock analysis technique on the strengths of its favourable correlations and its wide dynamic range of measurement.

6.2 Conclusions

All the tables, figures, and analyses presented in this thesis lead to a conclusion that is deceptively simple and intuitive. When audible knock occurs in a dual fuel engine, pressure or shock waves reverberate across the cylinder bore. Regardless of engine speed or knock intensity, this "ringing" begins at or very near P_{\max} and continues for a duration of about 40 crankshaft degrees. It was experimentally proven that the most effective pressure statistic was, quite simply, the maximum value of filtered pressure within the 40-degree window. It was also postulated that the best accelerometer statistic would be the maximum acceleration value within a corresponding window of filtered block vibration. Experimental evidence supported this hypothesis as well.

While the accelerometer signal is more prone to background noise than the pressure signal, it appears that there is enough information in a carefully chosen and filtered vibration window to reliably detect moderate levels of knock. It is also evident that there is a speed-dependent threshold value of block acceleration that separates normal and trace-knock operation from moderate to heavy levels of knock. This bodes well for the commercial implementation of non-intrusive knock detection as part of a dual fuel conversion kit.

6.3 Future Work

The work outlined in this investigation focused on detecting knock in one cylinder of a dual fuel engine using laboratory equipment. It was determined that a high-quality accelerometer and a sophisticated signal analysis system could accurately detect knock. The next developmental challenge involves performing the same task with inexpensive, production-volume equipment.

In this project, a Brüel and Kjær laboratory-grade vibration sensor was bolted to a central location on the OM366LA block. Further development work could investigate the usefulness of less expensive, more rugged broadband-resonant or spike-resonant accelerometers when attached to several different engine surface locations. It was discovered in this study that a 40-degree long window after the average crankshaft angle of maximum pressure (typically 12° to 16° ATDC) yielded the best results. The optimum length and synchronization of this window may vary with the resonance characteristics of other accelerometers.

It was also observed that the threshold level of vibration separating knocking and normal combustion varied with engine speed. Experimental evidence not provided in this document also suggests that due to the different distances between each combustion chamber and the accelerometer, a different threshold value might be necessary for each cylinder. For example, since cylinder four is closer than cylinder six to a centrally-located vibration sensor in an inline-six cylinder engine, it tends to cause higher peak acceleration levels for equivalent levels of combustion energy. Future testing could develop a three-dimensional “map” of threshold levels that vary with engine speed and cylinder number.

Finally, this project approached the problem of cycle-to-cycle knock variability by averaging statistics over 100 consecutive cycles. When knock intensifies, the average value of statistics such as maximum filtered acceleration (F_{Amax}) and maximum filtered

pressure (FP_{max}) tend to rise. Another approach would be to compare individual cycles to a predetermined threshold for each cylinder and engine speed. When a certain number of “knock” cycles are detected within a specific period of time, the engine control computer is alerted to the likelihood of knock. This way, occasional light-knocking cycles or random noise would not trigger corrective action, while frequent moderate or heavily-knocking cycles would. Like the 100-cycle average technique, this would allow the engine control computer to maximize diesel fuel replacement with a minimum of false-positive indications from infrequent, non-destructive knocking cycles. The difference lies in the level of sophistication required for each logic routine. Since the threshold value varies between cylinders and with engine speed, this logic would be fairly complicated and require extensive development. However, considering the potential effect of optimized fuel replacement on the health and well-being of city dwellers, the effort to fully develop an effective knock sensor seems justified.

REFERENCES

- [1] R. F. Sawyer, "The Formation and Destruction of Pollutants in Combustion Processes: Clearing The Air On The Role Of Combustion Research". *Eighteenth Symposium (International) on Combustion*, New York, USA: The Combustion Institute, 1981, pp. 6-8.
- [2] J. F. Cayot, "The Importance of Carbon Dioxide Emissions Legislation to the Future of the World Automobile Industry". *SAE Technical Paper 930941*, U.S. and European Automotive Emissions Technology (SP-957), Warrendale, USA: Society of Automotive Engineers, 1993, p. 202.
- [3] Automotive Handbook, 3rd Edition. Düsseldorf, Germany: Robert Bosch GmbH, 1993, pp. 232-233, 465, 665.
- [4] J. E. Sinor and B. K. Bailey, "Current and Potential Future Performance of Ethanol Fuels". *SAE Technical Paper 930376*, New Developments in Alternative Fuels and Gasolines for SI and CI Engines (SP-958), Warrendale, USA: Society of Automotive Engineers, 1993, pp. 84-87.
- [5] D. L. Hofeldt, "Alternative Fuel Technologies for Heavy Duty Vehicles: Performance, Emissions, Economics, Safety, and Development Status". *SAE Technical Paper 930731*, Warrendale, USA: Society of Automotive Engineers, 1993, p. 2.
- [6] M. D. Checkel, "The Alternative Fuel Decision and Current CNG Conversion Systems". *16th Annual Energy-Sources Technology Conference and Exhibition*, New York, USA: American Society of Mechanical Engineers, 1993, p. 4.
- [7] C. A. Kukkonen and M. Shelef, "Hydrogen as an Alternative Automotive Fuel: 1993 Update". *SAE Technical Paper 940766*, Warrendale, USA: Society of Automotive Engineers, 1994.
- [8] J. Kubesh, S. R. King, and W. E. Liss, "Effect of Gas Composition on Octane Number of Natural Gas Fuels". *SAE Technical Paper 922359*, Journal of Fuels and Lubricants, Warrendale, USA: Society of Automotive Engineers, 1992, pp. 1862-1864.

- [9] R. L. Boyer, "Status of Dual-Fuel Engine Development". *SAE Journal volume 57*, Warrendale, USA: Society of Automotive Engineers, 1949.
- [10] M. R. Johnson, "Development of a Low Emissions, Lean Premixed Natural Gas Burner". M.Sc. thesis, University of Alberta, 1995, pp. 5-6, 97.
- [11] M. D. Checkel, P. Newman, and A. Nishimura, "An Optimized Diesel Dual Fuel Urban Delivery Truck". *Paper PS63, vol. 4*, 5th Biennial IANGV International Conference and Exhibition NGV '96, IANGV, 1996, pp. 2-4.
- [12] C. F. Taylor, *The Internal-Combustion Engine in Theory and Practice, Volume 2-Revised Edition*. Cambridge, USA: The M.I.T. Press, 1985, pp. 40-41.
- [13] R. Hickling, F.H. Chen, and D. A. Feldmaier, "Pressure Pulsations in Engine Cylinders". *Engine Noise - Excitation, Vibration, and Radiation*, New York, USA: Plenum Press, 1982, pp. 3-26.
- [14] G. A. Karim, S. R. Klat, and N. P. Moore, "Knock in Dual-Fuel Engines". *Proceedings of the Institution of Mechanical Engineers, vol. 181, pt. 1*, London, UK, 1967.
- [15] C. S. Draper, "Pressure Waves Accompanying Detonation in the Internal Combustion Engine". *Journal of the Aeronautical Sciences, vol. 5, no. 6*, New York, USA: Institute of the Aeronautical Sciences, 1938.
- [16] T. Midgely Jr. and T. A. Boyd, "Methods of Measuring Detonation in Engines". *SAE Transactions, vol. 17, pt. 1*, Warrendale, USA: Society of Automotive Engineers, 1922.
- [17] J. B. Heywood, *Internal Combustion Engine Fundamentals*. Toronto, Canada: McGraw-Hill Inc., 1988, pp. 450-478.
- [18] G. König and C. G. W. Sheppard, "End Gas Autoignition and Knock in a Spark Ignition Engine". *SAE Technical Paper 902135*, Journal of Fluids and Lubricants, Warrendale, USA: Society of Automotive Engineers, 1990, pp. 820-836.
- [19] Y. Nakagawa, Y. Takagi, T. Itoh, and T. Iijima, "Laser Shadowgraphic Analysis of Knocking in S.I. Engine". *SAE Technical Paper 845001*, Warrendale, USA: Society of Automotive Engineers, 1984.

- [20] D. Scholl, S. Russ, and W. Stockhausen, "Detection of Spark Knock Oscillations: Dependence on Combustion Temperature. *SAE Technical Paper 970038*, Spark-Ignition Engine Combustion and Emissions (SP-1276), Warrendale, USA: Society of Automotive Engineers, 1997, p. 33.
- [21] P. M. Liiva, J. N. Valentine, J. M. Cobb, and W. P. Acker, "Use of Multiple Pressure Transducers to Find In-Cylinder Knock Location". *SAE Technical Paper 922368*, Warrendale, USA: Society of Automotive Engineers, 1992, p. 3.
- [22] P. O. Witze and R. M. Green, "Determining the Location of End-Gas Autoignition Using Ionization Probes Installed In The Head Gasket". *SAE Technical Paper 932645*, Warrendale, USA: Society of Automotive Engineers, 1993, pp. 1-17.
- [23] U. Spicher, H. Kroger, and J. Ganser, "Detection of Knocking Combustion using Simultaneously High-Speed Schlieren Cinematography and Multi Optical Fiber Technique". *SAE Technical Paper 912312*, Warrendale, USA: Society of Automotive Engineers, 1991.
- [24] P. V. Puzinauskas, "Examination of Methods Used to Characterize Engine Knock". *SAE Technical Paper 920808*, Warrendale, USA: Society of Automotive Engineers, 1992.
- [25] K. M. Chun and J. B. Heywood, "Characterization of Knock in a Spark-Ignition Engine". *SAE Technical Paper 890156*, Warrendale, USA: Society of Automotive Engineers, 1989.
- [26] K. M. Chun and K. W. Kim, "Measurement and Analysis of Knock in a SI Engine Using the Cylinder Pressure and Block Vibration Signals". *SAE Technical Paper 940146*, Warrendale, USA: Society of Automotive Engineers, 1994.
- [27] T. H. Valtadoros, V. W. Wong, and J. B. Heywood, "Engine Knock Characteristics at the Audible Level". *SAE Technical Paper 910567*, Warrendale, USA: Society of Automotive Engineers, 1991.
- [28] M. D. Checkel and J. D. Dale, "Computerized Knock Detection from Engine Pressure Records". *SAE Technical Paper 860028*, Warrendale, USA: Society of Automotive Engineers, 1986.
- [29] M. D. Checkel and J. D. Dale, "Testing a Third Derivative Knock Indicator on a Production Engine". *SAE Technical Paper 861216*, Warrendale, USA: Society of Automotive Engineers, 1986.

- [30] M. D. Checkel and J. D. Dale, "Pressure Trace Knock Measurement in a Current S.I. Production Engine". *SAE Technical Paper 890243*, Warrendale, USA: Society of Automotive Engineers, 1989.
- [31] H. Ando, J. Takemura, and E. Koujina, "A Knock Anticipating Strategy Based on the Real Time Combustion Mode Analysis". *SAE Technical Paper 890882*, Warrendale, USA: Society of Automotive Engineers, 1989.
- [32] E. Rosseel and R. Sierens, "Knock Detection in a Hydrogen Engine". *SAE Technical Paper 970039*, Spark-Ignition Engine Combustion and Emissions (SP-1267), Warrendale, USA: Society of Automotive Engineers, 1997, p. 43.
- [33] W. Herden and M. Küssel, "A New Combustion Pressure Sensor for Advanced Engine Management". *SAE Technical Paper 940379*, Electronic Engine Controls 1994 (SP-1029), Warrendale, USA: Society of Automotive Engineers, 1994, pp. 177-179.
- [34] H. Kusakabe, T. Okauchi, and M. Takigawa, "A Cylinder Pressure Sensor for Internal Combustion Engine". *SAE Technical Paper 920701*, Sensors and Actuators 1992 (SP-903), Warrendale, USA: Society of Automotive Engineers, 1992.
- [35] B. Samimy and G. Rizzoni, "Engine Knock Analysis and Detection Using Time-Frequency Analysis". *SAE Technical Paper 960618*, Design Innovations in Engine Management and Driveline Controls (SP-1153), Warrendale, USA: Society of Automotive Engineers, 1996, p. 15.
- [36] Technical Data Sheet, CC195 Knock Sensor IC Specification ver. 6.9a. Düsseldorf, Germany: Robert Bosch GmbH, 1996.
- [37] S. M. Dues, J. M. Adams, and G. A. Shinkle, "Combustion Knock Sensing: Sensor Selection and Application Issues". *SAE Technical Paper 900488*, Journal of Engines, Warrendale, USA: Society of Automotive Engineers, 1990.
- [38] K. Kaji, S. Matsushige, M. Kanamaru, J. Takahashi, and S. Asano, "Development of Knock Sensor". *SAE Technical Paper 861375*, Warrendale, USA: Society of Automotive Engineers, 1986.
- [39] Workshop Manual. Engine Model OM 366LA. Portland, USA: Mercedes-Benz Truck Co. Inc., 1987, p. 100/1.

- [40] R. L. Barkhimer, N. J. Beck, and W. E. Weseloh, "Development of a Durable, Reliable and Fast Responding Solenoid Valve". *SAE Technical Paper 831326*, Warrendale, USA: Society of Automotive Engineers, 1983.
- [41] 1992 SAE Handbook, Volume 3: Engines, Fuels, Lubricants, Emissions, and Noise. Warrendale, USA: Society of Automotive Engineers, 1992, p. 24.10.
- [42] Technical Data Sheet, Measurements on Internal Combustion Engines: Research, Development, Monitoring. Winterthur, Switzerland: Kistler Instrumente AG, 1989.
- [43] A. L. Randolph, "Methods of Processing Cylinder-Pressure Transducer Signals to Maximize Data Accuracy". *SAE Technical Paper 900170*, Warrendale, USA: Society of Automotive Engineers, 1990.
- [44] M. F. Brunt, C. R. Pond, "Evaluation of Techniques for Absolute Cylinder Pressure Correction". *SAE Technical Paper 970036*, Spark-Ignition Engine Combustion and Emissions (SP-1267), Warrendale, USA: Society of Automotive Engineers, 1997.
- [45] P. P. Nowak, personal communication - knock sensor location, 1994-1997.
- [46] W. D. Stanley, Digital Signal Processing. Reston, USA: Reston Publishing Co., 1975.
- [47] A. Peled and B. Liu, Digital Signal Processing: Theory, Design, and Implementation. Toronto, Canada: John Wiley & Sons, 1976, pp. 135-141.
- [48] G. Benson, E. Fletcher, T. Murphy, and H. Scherrer, "Knock (Detonation) Control by Engine Combustion Chamber Shape". *SAE Technical Paper 830509*, Warrendale, USA: Society of Automotive Engineers, 1983.
- [49] N. P. Cheremisinoff, Practical Statistics for Engineers and Scientists. Lancaster, USA: Technomic Publishing Company Inc., 1987, pp. 7, 113.
- [50] R. Shiavi, Introduction to Applied Statistical Signal Analysis. Boston, USA: Aksen Associates Inc., 1991, p. 77.
- [51] K. Fyfe, *Mec.E.653 Signal Processing of Time and Spectral Series class notes*. University of Alberta, 1997.
- [52] D. Halliday and R. Resnick, Fundamentals of Physics. Toronto, Canada: John Wiley & Sons, Inc., 1970, p. 326.

**APPENDIX
A**

**PRESSURE TRANSDUCER
CALIBRATION**

A Kistler 601B1 miniature pressure transducer was installed in a spare Mercedes OM366LA engine head to measure combustion pressure. With this particular engine, peak pressures up to approximately 12 MPa (1500 psi) were expected for intense knocking cycles. A Budenberg dead-weight tester was used to calibrate the transducer and its Sundstrand model 507 differential amplifier over a range of 69 to 13790 kPa (10 - 2000 psig). With the amplifier adjusted for “charge” mode and “long” time constant, the transducer was hydraulically loaded from low to high pressure in 200 psi increments. The output of the transducer, connecting cable, and amplifier is shown in Table A.1. The data given in this table is for ascending pressure, but virtually no hysteresis was observed when the transducer was unloaded in the same 200 psi steps.

Table A.1 Kistler 601B1 Pressure Transducer Calibration Data

Hydraulic Load (psi)	Hydraulic Load (kPa)	Amplifier Output (V)
10	69	0.046
200	1379	0.205
400	2758	0.364
600	4137	0.524
800	5516	0.686
1000	6895	0.846
1200	8274	1.007
1400	9653	1.167
1600	11032	1.328
1800	12411	1.488
2000	13790	1.649

The relationship between applied pressure and amplifier output is given by Equation A.1, where V is in volts and P is in kPa (see Figure A.1).

$$V = 0.04427 + 0.00011633 \cdot P \quad (\text{A.1})$$

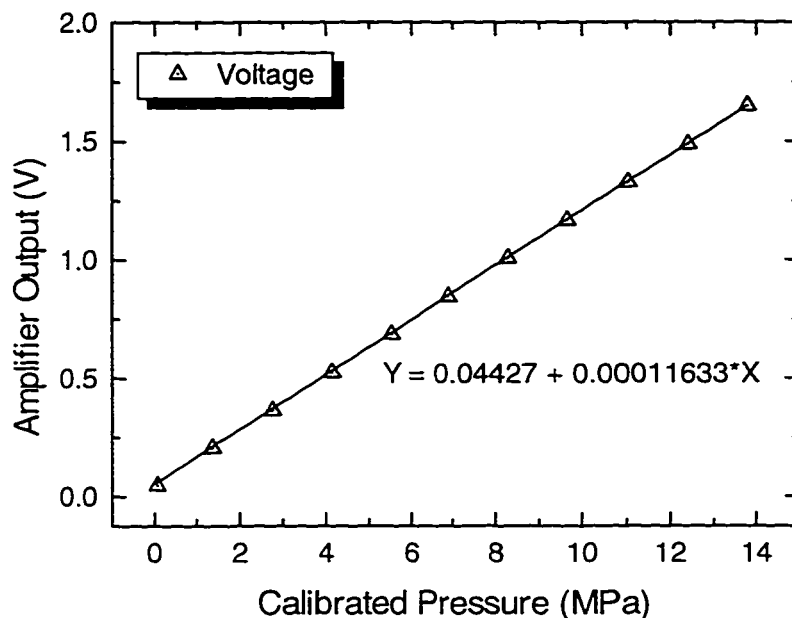


Figure A.1 Pressure Transducer Calibration Curve

Channel two of the Racal Store-4DS tape deck was outfitted with a unipolar input card. The range selector of this card was set to 10 for all knock experiments. At this setting, the channel's full-scale input level is 2.5 volts, and the output is scaled to a unipolar 0 - 5 volt range. A Keithley Metrabyte DAS-16 data acquisition system digitized the tape recorder's output, with a 0 - 5 volt input range corresponding to 0 - 4096 A/D counts. The overall equation governing tape deck input volts to 16-bit A/D counts stored on the PC is given by Equation A.2.

$$V_{in} = \frac{C}{4096} \cdot \frac{T_{range}}{2.5} \quad (A.2)$$

where: V_{in} = voltage into tape deck (V)

C = A/D counts

T_{range} = tape deck range selector (set to 10 for pressure recording)

Equating the voltages leaving the amplifier and entering the tape deck allows the determination of how the A/D counts stored in the binary data files are related to pressure, as in Equations A.3.

$$0.04427 + 0.00011633 \cdot P = \frac{C}{4096} \cdot \frac{T_{range}}{2.5} \quad (A.3a)$$

$$0.00011633 \cdot P = \frac{C}{1024} - 0.04427 \quad (A.3b)$$

$$P = 8.3949 \cdot C - 380.56 \quad (A.3c)$$

This correlation allows the QuickBASIC computer analysis programs to infer pressures from the binary pressure data records. However, there are a number of offsets that must be accounted for. Firstly, the pressure channel of the tape recorder has a small zero offset, as measured during calibration. As well, the pressure transducer's output drifted with combustion temperature. The hotter the transducer became, the lower its voltage output shifted. Finally, an artificial bias was introduced to the pressure signal to prevent it from drifting below 0 volts during periods of heavy knock. All of these offsets were linear signal shifts, i.e. the entire pressure range was translated equally. These errors were all corrected at once by "pegging" the signal to a point of known pressure. In this project, the pressure was pegged to manifold absolute pressure when the piston was at bottom-dead-centre before compression, as in Figure A.2. This technique is

recommended by Randolph [“Methods of Processing Cylinder-Pressure Transducer Signals to Maximize Data Accuracy”. *SAE Technical Paper 900170*, Warrendale, USA: Society of Automotive Engineers, 1990] and Brunt et al [“Evaluation of Techniques for Absolute Cylinder Pressure Correction”. *SAE Technical Paper 970036*, Warrendale, USA: Society of Automotive Engineers, 1997] in the literature. At 180 degrees BTDC, the recorded pressure (in counts) is compared to the MAP (in counts). The difference (in counts) is the total amount of offset due to calibration zero offsets and thermal drift. The calculated offset is applied to the entire pressure array before converting the array to pressure. In this way, the program determines true absolute pressure. Maximum pressure statistics are later extracted from the signal for analysis.

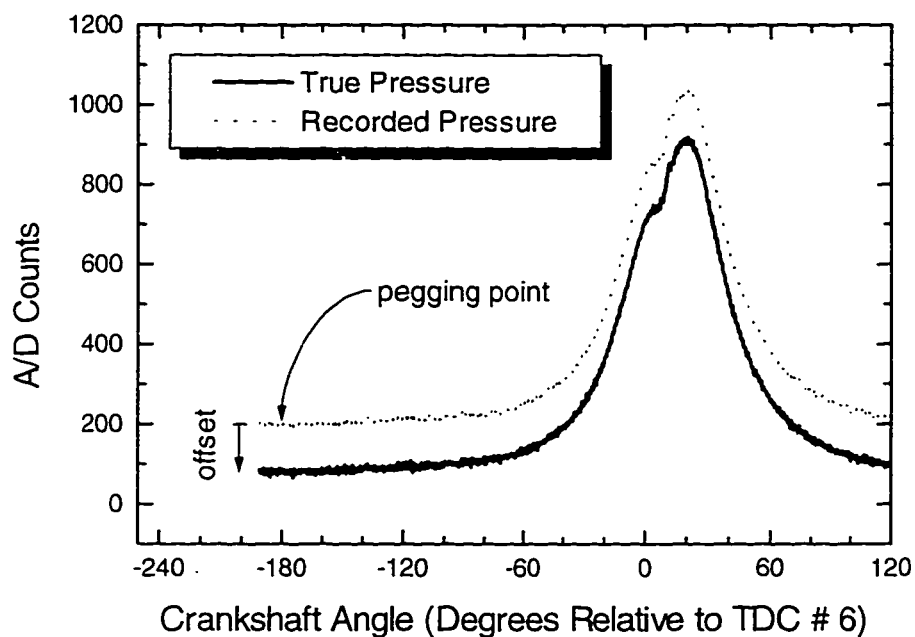


Figure A.2 Binary Pressure Signal “Pegging”

APPENDIX
B

STANDARD KNOCK INTENSITY
DATA

Table B.1 Observed SKI Levels, Gaseous Overfuelling

Engine Speed (rpm)	Gas Supply Pressure (kPa)	Observed SKI Value (scale of 1 - 5)
1500	1000	1
1500	1100	1
1500	1200	2
1500	1300	3
1500	1400	3.5
1500	1500	4
1500	1600	4
2100	1000	1
2100	1100	1.5
2100	1200	2
2100	1300	3
2100	1400	4
2100	1500	4
2100	1600	5

Table B.2 Observed SKI Levels, Pilot Reduction

Engine Speed (rpm)	Diesel Pilot Quantity (mg/inj.)	Observed SKI Value (scale of 1 - 5)
1500	40	1
1500	35	1
1500	30	2
1500	25	3.5
1500	20	4
2100	40	1
2100	35	2
2100	30	3
2100	25	3
2100	20	5

ESTIMATING THE FUNDAMENTAL
KNOCK FREQUENCY

The resonant frequency of a combustion chamber is a function of its diameter and the speed of sound through the products of combustion, as in Equation C.1.

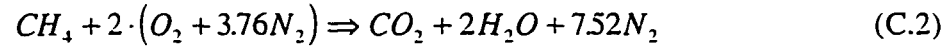
$$f = \xi_m \cdot \frac{c}{D} \quad (\text{C.1})$$

where: f = knock frequency (Hz)
 ξ_m = non-dimensional mode factor
 c = local speed of sound (m/s)
 D = diameter of cylinder (m)

In their 1982 paper "Pressure Pulsations In Engine Cylinders" [*Engine Noise: Excitation, Vibration, and Radiation*, New York, USA: Plenum Press, 1982], Hickling *et al* determined the non-dimensional mode factors for knock above a diesel engine offset-bowl piston through finite element analysis. Depending on the orientation of the piston, this factor should be either $\xi_m = 0.673$ or $\xi_m = 0.715$.

The bore diameter of the OM366LA's cylinders is 0.0975 m. The speed of sound after combustion was estimated with a computer combustion model called STANJAN. All residual gases were assumed to be the products of methane combustion in excess air.

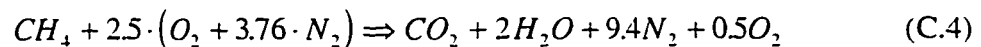
The ideal stoichiometric relationship governing this process (neglecting products of incomplete combustion), is given in Equation C.2.



It was observed during testing that the engine ingested a total of 100 g/s fresh air and 3.5 g/s CNG at 1500 rpm and full torque. This gives an Air/Fuel (AF) ratio of 28.6:1 on a mass basis. Stoichiometrically-correct AF for CH₄ combustion is 17.1:1. As a result, the equivalence ratio at full torque when not knocking is:

$$\Phi = \frac{\text{stoichiometric AF}}{\text{observed AF}} = \frac{17.1}{28.6} = 0.60 \quad (C.3)$$

Overfuelling one of the cylinders with CNG by about 33% led to moderate levels of knock at 1500 rpm. By increasing the gas mass flow rate from 3.5 g/s to 4.67 g/s, the AF ratio rises to 0.80. Equation C.4 shows the combustion reaction for lean ($\Phi = 0.80$) methane combustion (neglecting trace products).



In the laboratory, the observed manifold air temperature was 330 K at an absolute pressure of approximately 1.5 atmospheres. The reactants of Equation C.4 were input to STANJAN at these conditions (State 1) to model the fresh gas/air intake charge. The charge was isentropically compressed by the OM366LA compression ratio (17.4:1) to State 2. Next, it was reacted to gaseous products (State 3) by a constant-volume combustion model, approximating the spark-ignition knock process. STANJAN's output for each state are summarized as follows.

State 1: Inducted Fresh Mixture

$$\begin{aligned}
 T_1 &= 330 \text{ K} & P_1 &= 1.52 \cdot 10^5 \text{ Pa} \\
 v_1 &= 6.480 \cdot 10^{-1} \text{ m}^3/\text{kg} & u_1 &= -2.728 \cdot 10^5 \text{ J/kg} \\
 & \text{speed of sound} & &= 370 \text{ m/s}
 \end{aligned}$$

State 2: Compressed Mixture

$$\begin{aligned}
 T_2 &= 900 \text{ K} & P_2 &= 7.215 \cdot 10^6 \text{ Pa} \\
 v_2 &= 3.724 \cdot 10^{-2} \text{ m}^3/\text{kg} & u_2 &= 2.206 \cdot 10^5 \text{ J/kg} \\
 & \text{speed of sound} & &= 593 \text{ m/s}
 \end{aligned}$$

State 3: Combustion Products

$$\begin{aligned}
 T_3 &= 2778 \text{ K} & P_3 &= 1.236 \cdot 10^7 \text{ Pa} \\
 v_3 &= 3.724 \cdot 10^{-2} \text{ m}^3/\text{kg} & u_3 &= 2.206 \cdot 10^5 \text{ J/kg} \\
 & \text{speed of sound} & &= 1003 \text{ m/s}
 \end{aligned}$$

For a sound velocity of 1000 m/s, a diameter of 0.0975 m, and the mode coefficients listed previously, the predicted fundamental knock frequencies for this engine are given in Equations C.5 and C.6.

For $\xi_m = 0.715$:

$$f = 0.715 \cdot \frac{1000}{0.0975} = 7333 \text{ Hz} \quad (\text{C.5})$$

For $\xi_m = 0.673$:

$$f = 0.673 \cdot \frac{1000}{0.0975} = 6903 \text{ Hz} \quad (\text{C.6})$$

**APPENDIX
D**

**PRESSURE INVESTIGATION
DATA**

Table D.1 Correlation of Maximum Filtered Pressure to SKI, 1500 rpm

SKI	FPmax (kPa) with Various Window Widths					
	10°	20°	30°	40°	50°	60°
1	20.6	25.4	39.1	41.3	41.4	41.5
1	23.2	26.5	41.0	43.9	44.1	44.2
2	19.8	25.9	73.7	74.4	74.4	74.4
3	19.0	26.2	147.3	147.3	147.3	147.3
3.5	22.3	27.4	155.2	155.2	155.2	155.2
4	21.5	27.1	171.1	171.2	171.2	171.2
4	21.2	27.0	173.6	173.6	173.6	173.6
Correlation:	-0.1010	0.7702	0.9899	0.9897	0.9896	0.9896

Table D.2 Correlation of Maximum Filtered Pressure to SKI, 2100 rpm

SKI	FPmax (kPa) with Various Window Widths					
	10°	20°	30°	40°	50°	60°
1	19.6	22.6	53.8	55.8	55.8	55.8
1.5	19.2	22.2	47.5	58.9	59.3	59.5
2	18.7	21.6	53.7	82.5	82.5	82.5
3	17.0	18.6	88.7	144.0	144.0	144.0
4	21.0	23.2	217.7	255.3	255.3	255.3
4	20.7	23.6	266.9	279.9	279.9	279.9
5	18.5	21.1	611.5	613.1	613.1	613.1
Correlation:	0.1332	-0.0120	0.8607	0.8966	0.8965	0.8965

Table D.3 Correlation of RMS Filtered Pressure to SKI, 1500 rpm

SKI	FPrms (kPa) with Various Window Widths					
	10°	20°	30°	40°	50°	60°
1	9.08	9.7	12.9	13.9	13.4	12.9
1	10.22	10.5	13.8	15.4	14.8	14.1
2	8.92	9.5	21.4	23.7	22.3	20.5
3	8.51	9.6	43.5	45.8	42.1	38.7
3.5	9.84	10.5	46.2	49.7	46.0	42.3
4	9.59	10.3	51.0	54.2	50.0	46.0
4	9.22	10.2	51.9	56.4	49.1	47.9
Correlation:	-0.0614	0.2774	0.9884	0.9907	0.9894	0.9904

Table D.4 Correlation of RMS Filtered Pressure to SKI, 2100 rpm

SKI	FPrms (kPa) with Various Window Widths					
	10°	20°	30°	40°	50°	60°
1	9.03	9.4	16.4	15.3	16.5	15.6
1.5	9.27	9.4	14.8	20.4	20.3	19.2
2	8.92	9.0	15.0	27.3	27.1	25.4
3	8.01	8.1	19.6	45.9	44.9	41.7
4	9.81	9.8	44.3	85.5	81.1	75.0
4	9.72	9.8	61.8	88.1	82.9	76.4
5	8.96	9.1	163.2	192.6	181.6	166.7
Correlation:	0.2089	0.1148	0.8042	0.9063	0.9042	0.9048

Table D.5 Correlation of Filtered Pressure FT Amplitude to SKI, 1500 rpm

SKI	FPamp (kPa) with Various Window Widths					
	10°	20°	30°	40°	50°	60°
1	2.62	2.40	3.27	3.78	3.10	2.53
1.5	3.19	2.68	3.74	4.49	3.73	3.13
2	2.43	2.16	6.06	7.42	5.66	4.40
3	2.37	2.18	12.85	15.45	11.40	8.32
4	2.83	2.88	14.39	16.29	12.89	9.71
4	2.78	2.79	15.49	18.18	13.75	10.55
5	2.47	2.72	15.91	18.80	13.88	10.26
Correlation:	-0.2043	0.4254	0.9894	0.9894	0.9890	0.9886

Table D.6 Correlation of Filtered Pressure FT Amplitude to SKI, 2100 rpm

SKI	FPamp (kPa) with Various Window Widths					
	10°	20°	30°	40°	50°	60°
1	2.83	2.72	4.83	4.96	4.80	3.73
1.5	2.83	2.57	4.07	6.47	6.59	6.79
2	2.74	2.54	3.98	8.44	8.94	7.25
3	2.30	1.97	4.66	15.36	14.24	11.96
4	3.03	2.63	10.82	29.26	26.55	19.43
4	3.28	2.76	15.59	30.24	25.86	16.35
5	2.52	2.27	45.04	68.08	58.62	39.69
Correlation:	0.0350	-0.2631	0.7763	0.9013	0.9036	0.8992

Table D.7 Correlation of Pressure Statistics to SKI for 40-degree Window, Pilot Reduction, 1500 rpm

Pilot (mg/inj.)	SKI	Pmax (kPa)	FPmax (kPa)	FPrms (kPa)	FPamp (kPa)
40	1	9532	77.3	23.92	6.92
35	1	10144	75.5	24.92	7.38
30	2	10547	90.7	28.97	9.08
25	3.5	11048	149	45.78	15.02
20	4	11167	174	52.6	19.67
Correlation to SKI:		0.9310	0.9839	0.9864	0.9738

Table D.8 Correlation of Pressure Statistics to SKI for 40-degree Window, Pilot Reduction, 2100 rpm

Pilot (mg/inj.)	SKI	Pmax (kPa)	FPmax (kPa)	FPrms (kPa)	FPamp (kPa)
40	1	9857	132	45.11	15.74
35	2	10416	156	50.8	16.83
30	3	10422	242	79.6	27.33
25	3	10162	247	78.75	27.14
20	5	11072	605	189.3	67.09
Correlation to SKI:		0.9029	0.9428	0.9418	0.9365

**ACCELEROMETER WINDOW START POSITION
DATA**

Table E.1 Correlation of F_{Amax} to F_{Pmax} At Various Start Positions, 1500 rpm

F _{Pmax} (kPa)	F _{Amax} (kPa) Using Various Start Positions (deg. ATDC)					
	0°	4°	8°	12°	16°	20°
41.3	260	260	260	260	258	159
43.9	266	266	266	265	257	169
74.4	311	311	311	310	306	178
147.3	304	304	304	304	294	170
155.2	328	328	328	328	323	202
171.2	355	355	355	355	345	210
173.6	306	306	306	306	303	192
Correlation:	0.8081	0.8081	0.8081	0.8136	0.8105	0.7923

Table E.2 Correlation of F_{Amax} to F_{Pmax} At Various Start Positions, 2100 rpm

F _{Pmax} (kPa)	F _{Amax} (kPa) Using Various Start Positions (deg. ATDC)					
	4°	8°	12°	16°	20°	24°
55.8	390	390	390	390	390	290
58.9	354	354	354	354	354	275
82.5	403	403	403	403	403	345
144	506	506	506	506	506	488
255.3	422	422	422	422	421	381
279.9	444	444	444	444	444	372
613.1	578	578	578	578	574	544
Correlation:	0.8368	0.8368	0.8368	0.8368	0.8311	0.7849

Table E.3 Correlation of FArms to FPmax At Various Start Positions, 1500 rpm

FPmax (kPa)	FArms (kPa) Using Various Start Positions (deg. ATDC)					
	0°	4°	8°	12°	16°	20°
41.3	78.5	80.0	80.6	81.1	74.7	56.6
43.9	82.4	83.6	82.9	84.8	75.4	60.9
74.4	91.0	92.1	92.6	95.1	86.8	61.3
147.3	87.4	88.8	89.9	92.0	82.5	59.6
155.2	95.4	97.6	94.1	101.9	100.7	74.3
171.2	103.3	105.1	107.0	109.4	105.1	81.4
173.6	90.9	93.2	94.9	96.5	91.4	73.2
Correlation:	0.7755	0.7961	0.7993	0.8154	0.8100	0.7889

Table E.4 Correlation of FArms to FPmax At Various Start Positions, 2100 rpm

FPmax (kPa)	FArms (kPa) Using Various Start Positions (deg. ATDC)					
	4°	8°	12°	16°	20°	24°
55.8	122	124	129	136	135	102
58.9	119	121	126	133	134	108
82.5	129	133	138	146	148	119
144	163	166	172	182	185	161
255.3	129	131	137	144	147	125
279.9	139	143	148	157	158	130
613.1	204	210	216	231	232	201
Correlation:	0.8558	0.8597	0.8601	0.8620	0.8595	0.8532

Table E.5 Correlation of FAamp to FPmax At Various Start Positions, 1500 rpm

FPmax (kPa)	FAamp (kPa) Using Various Start Positions (deg. ATDC)					
	0°	4°	8°	12°	16°	20°
41.3	25.1	26.3	27.2	23.7	19.1	15.8
43.9	23.5	26.2	27.9	25.7	21.7	17.1
74.4	27.7	25.5	28.6	29.9	23.5	16.1
147.3	25.2	25.1	25.2	25.8	19.7	15.0
155.2	26.7	28.6	29.4	27.5	23.3	16.9
171.2	24.5	28.0	32.6	29.2	26.3	19.7
173.6	24.8	25.0	28.8	25.8	23.0	18.0
Correlation:	0.0475	0.2229	0.3853	0.3230	0.5130	0.4658

Table E.6 Correlation of FAamp to FPmax At Various Start Positions, 2100 rpm

FPmax (kPa)	FAamp (kPa) Using Various Start Positions (deg. ATDC)					
	4°	8°	12°	16°	20°	24°
55.8	40.9	37.5	37.9	37.7	35.5	24.4
58.9	42.2	34.4	34.8	42.0	40.9	28.3
82.5	36.2	39.1	37.7	39.8	37.5	25.2
144	50.5	52.5	50.7	52.0	48.2	35.1
255.3	36.3	40.0	40.0	41.7	36.9	27.9
279.9	42.1	46.6	41.8	45.8	39.8	29.1
613.1	63.7	64.6	66.8	66.5	63.0	45.4
Correlation:	0.7582	0.8571	0.8684	0.8691	0.8121	0.8519

**APPENDIX
F**

**ACCELEROMETER WINDOW LENGTH
DATA**

Table F.1 Correlation of FAmax to FPmax, Gaseous Overfuelling, 1500 rpm

FPmax (kPa)	FAmax (g*) with Various Window Widths					
	10°	20°	30°	40°	50°	60°
41.3	390	260	260	260	260	246
43.9	263	265	265	265	265	242
74.4	310	310	310	310	310	318
147.3	303	304	304	304	304	287
155.2	325	328	328	328	328	320
171.2	352	355	355	355	355	356
173.6	302	306	306	306	306	307
Correlation:	-0.0210	0.8136	0.8136	0.8136	0.8136	0.7637

Table F.2 Correlation of FAmax to FPmax, Gaseous Overfuelling, 2100 rpm

FPmax (kPa)	FAmax (g*) with Various Window Widths					
	10°	20°	30°	40°	50°	60°
55.8	390	390	390	390	390	386
58.9	354	354	354	354	354	348
82.5	403	403	403	403	403	381
144	496	506	506	506	506	531
255.3	412	420	422	422	422	416
279.9	434	439	444	444	444	432
613.1	566	570	578	578	578	584
Correlation:	0.8278	0.8213	0.8368	0.8368	0.8368	0.7810

Table F.3 Correlation of FArms to FPmax, Gaseous Overfuelling, 1500 rpm

FPmax (kPa)	FArms (g*) with Various Window Widths					
	10°	20°	30°	40°	50°	60°
41.3	174	100	87.5	81.1	81.1	77.0
43.9	133	108	92.2	84.8	84.8	79.9
74.4	156	121	103.6	95.1	95.1	96.3
147.3	146	115	99.7	92.0	92.0	89.0
155.2	134	125	110.1	101.9	101.9	99.6
171.2	163	133	118.5	109.4	109.4	111.6
173.6	141	118	103.6	96.5	96.5	97.2
Correlation:	-0.2488	0.7553	0.7946	0.8154	0.8154	0.7930

Table F.4 Correlation of FArms to FPmax, Gaseous Overfuelling, 2100 rpm

FPmax (kPa)	FArms (g*) with Various Window Widths					
	10°	20°	30°	40°	50°	60°
55.8	206	162	141	136	136	135.6
58.9	188	155	137	133	133	131.4
82.5	214	171	151	146	146	139.6
144	263	223	189	182	182	191.1
255.3	204	170	150	144	144	142.1
279.9	219	175	163	157	157	154.0
613.1	306	248	236	231	231	233.6
Correlation:	0.7846	0.7517	0.8591	0.8620	0.8620	0.8232

Table F.5 Correlation of FAamp to FPmax, Gaseous Overfuelling, 1500 rpm

FPmax (kPa)	FAamp (g*) with Various Window Widths					
	10°	20°	30°	40°	50°	60°
41.3	66.3	35.4	32.5	23.7	21.8	17.0
43.9	63.5	39.7	34.1	25.7	22.8	18.2
74.4	67.0	47.3	35.0	29.9	23.5	21.3
147.3	55.5	39.2	30.2	25.8	22.3	17.7
155.2	65.7	44.7	35.9	27.5	24.4	20.3
171.2	66.9	50.9	37.7	29.2	25.9	23.2
173.6	58.2	43.5	33.1	25.8	22.6	20.1
Correlation:	-0.3849	0.5497	0.1961	0.3230	0.5034	0.5350

Table F.6 Correlation of FAamp to FPmax, Gaseous Overfuelling, 2100 rpm

FPmax (kPa)	FAamp (g*) with Various Window Widths					
	10°	20°	30°	40°	50°	60°
55.8	67.7	55.7	47.2	37.7	33.7	28.2
58.9	83.8	54.2	44.1	42.0	36.3	30.9
82.5	80.0	59.8	47.5	39.8	35.7	30.8
144	97.8	75.3	63.5	52.0	45.2	41.0
255.3	79.2	62.3	49.0	41.7	34.2	29.3
279.9	96.6	64.2	53.9	45.8	38.2	33.3
613.1	121.0	99.4	85.0	66.5	56.9	49.5
Correlation:	0.8499	0.8887	0.8731	0.8691	0.8171	0.7870

Table F.7 Correlation of FAmx to FPmax, Pilot Reduction, 1500 rpm

FPmax (kPa)	FAmx (g*) with Various Window Widths					
	10°	20°	30°	40°	50°	60°
77.3	198	201	201	201	201	213
75.5	199	203	205	205	205	205
90.7	312	312	312	312	312	319
149	248	257	258	258	258	268
174	335	337	337	337	337	338
Correlation:	0.6533	0.6839	0.6857	0.6857	0.6857	0.6843

Table F.8 Correlation of FAmx to FPmax, Pilot Reduction, 2100 rpm

FPmax (kPa)	FAmx (g*) with Various Window Widths					
	10°	20°	30°	40°	50°	60°
132	281	292	294	294	294	302
156	287	304	306	306	306	286
242	335	342	343	343	343	343
247	374	378	380	380	380	388
605	565	569	580	580	580	564
Correlation:	0.9927	0.9945	0.9946	0.9946	0.9946	0.9847

Table F.9 Correlation of FARms to FPmax, Pilot Reduction, 1500 rpm

FPmax (kPa)	FARms (g*) with Various Window Widths					
	10°	20°	30°	40°	50°	60°
77.3	104	86.3	74.6	69.6	69.6	72.8
75.5	99	87.1	78.4	72.7	72.7	72.2
90.7	161	126	107.0	98.2	98.2	95.9
149	115	102	91.3	84.7	84.7	82.1
174	169	132	114.0	106.0	106.0	106.5
Correlation:	0.5429	0.6217	0.6758	0.6948	0.6948	0.6923

Table F.10 Correlation of FARms to FPmax, Pilot Reduction, 2100 rpm

FPmax (kPa)	FARms (g*) with Various Window Widths					
	10°	20°	30°	40°	50°	60°
132	154	130	114	112	111.5	113.4
156	144	132	118	114	113.6	109.1
242	160	138	123	120	119.5	118.8
247	189	144	144	140	140.2	142.2
605	296	254	240	234	233.6	225.7
Correlation:	0.9879	0.9856	0.9864	0.9864	0.9861	0.9820

Table F.11 Correlation of FAamp to FPmax, Pilot Reduction, 1500 rpm

FPmax (kPa)	FAamp (g*) with Various Window Widths					
	10°	20°	30°	40°	50°	60°
77.3	47.0	30.0	24.4	21.0	18.6	16.9
75.5	44.1	29.2	28.7	19.3	19.1	15.6
90.7	83.3	53.3	41.0	30.9	26.5	22.6
149	50.8	37.7	29.3	25.6	22.2	20.2
174	51.2	45.8	36.1	31.3	25.4	22.1
Correlation:	-0.1110	0.3933	0.2912	0.6315	0.5310	0.6272

Table F.12 Correlation of FAamp to FPmax, Pilot Reduction, 2100 rpm

FPmax (kPa)	FAamp (g^*) with Various Window Widths					
	10°	20°	30°	40°	50°	60°
132	63.1	45.7	40.0	31.1	27.7	25.2
156	67.1	59.2	49.7	38.5	31.4	25.9
242	61.9	49.7	40.5	32.8	28.0	23.9
247	66.4	48.5	41.4	37.0	31.9	29.6
605	115	97.1	83.1	65.5	55.1	45.1
Correlation:	0.9570	0.9250	0.9216	0.9514	0.9609	0.9563